Yttria-Stabilized Zirconia / Gadolinium Zirconate Double-Layer Plasma-Sprayed Thermal Barrier Coating Systems (TBCs)

Emine Bakan

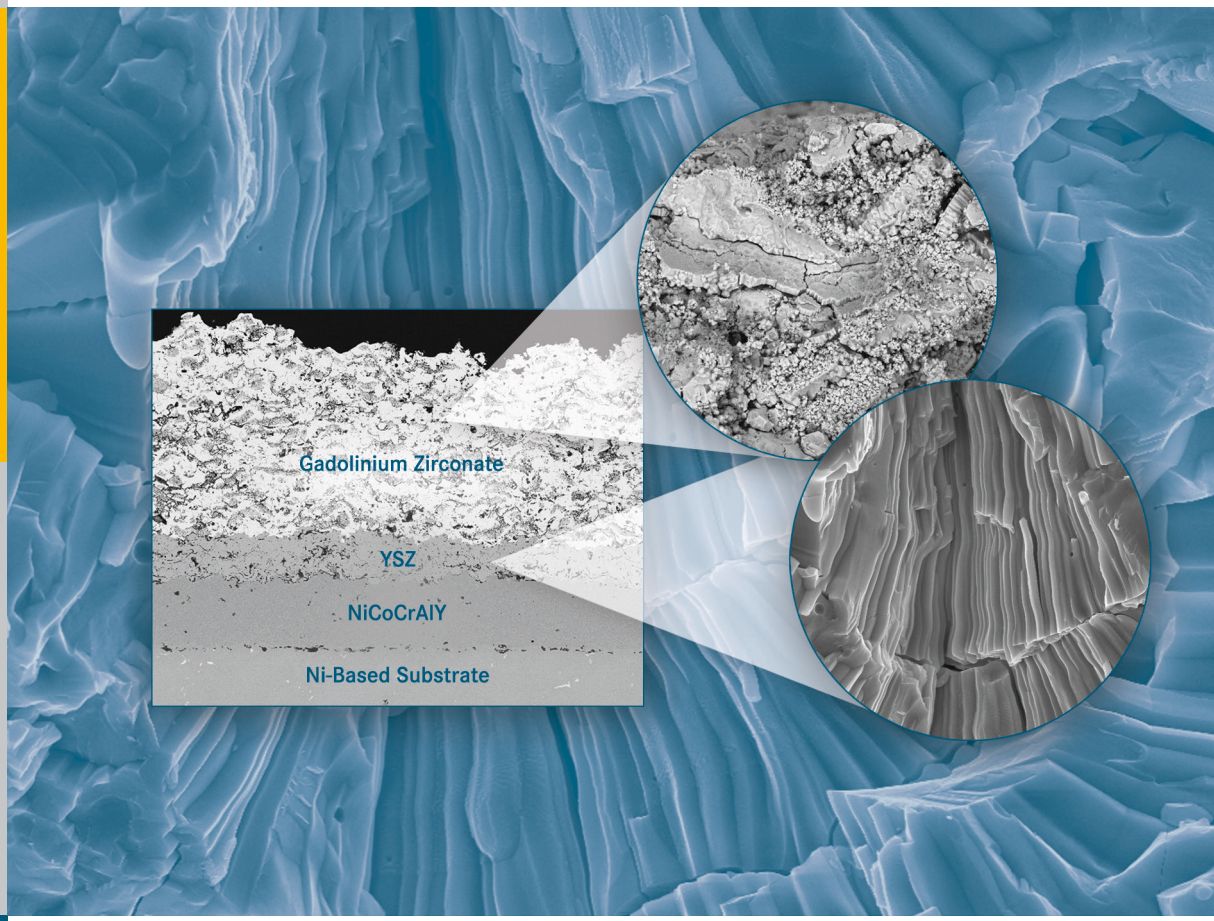

Energie & Umwelt / Energy & Environment
Band / Volume 294
ISBN 978-3-95806-100-2

JÜLICH
FORSCHUNGSZENTRUM

Schriften des Forschungszentrums Jülich
Reihe Energie & Umwelt / Energy & Environment Band / Volume 294

Forschungszentrum Jülich GmbH
Institute of Energy and Climate Research
Materials Synthesis and Processing (IEK-1)

Yttria-Stabilized Zirconia / Gadolinium Zirconate Double-Layer Plasma-Sprayed Thermal Barrier Coating Systems (TBCs)

Emine Bakan

Schriften des Forschungszentrums Jülich
Reihe Energie & Umwelt / Energy & Environment Band / Volume 294

ISSN 1866-1793 ISBN 978-3-95806-100-2

Bibliographic information published by the Deutsche Nationalbibliothek.
The Deutsche Nationalbibliothek lists this publication in the Deutsche Nationalbibliografie; detailed bibliographic data are available in the Internet at http://dnb.d-nb.de.

Publisher and Distributor: Forschungszentrum Jülich GmbH
Zentralbibliothek
52425 Jülich
Tel: +49 2461 61-5368
Fax: +49 2461 61-6103
Email: zb-publikation@fz-juelich.de
www.fz-juelich.de/zb

Cover Design: Grafische Medien, Forschungszentrum Jülich GmbH

Printer: Grafische Medien, Forschungszentrum Jülich GmbH

Schriften des Forschungszentrums Jülich
Reihe Energie & Umwelt / Energy & Environment, Band / Volume 294

D 294 (Diss., Bochum, Univ., 2015)

ISSN 1866-1793
ISBN 978-3-95806-100-2

The complete volume is freely available on the Internet on the Jülicher Open Access Server (JuSER) at www.fz-juelich.de/zb/openaccess.

Abstract

Thermal barrier coating (TBC) research and development is driven by the desirability of further increasing the maximum inlet temperature in a gas turbine engine. A number of new top coat ceramic materials have been proposed during the last decades due to limited temperature capability (1200 °C) of the state-of-the-art yttria-stabilized zirconia (7 wt. % Y_2O_3-ZrO_2, YSZ) at long term operation. Zirconate pyrochlores of the large lanthanides ($(Gd \rightarrow La)_2Zr_2O_7$) have been particularly attractive due to their higher temperature phase stability than that of the YSZ. Nonetheless, the issues related with the implementation of pyrochlores such as low fracture toughness and formation of deleterious interphases with thermally grown oxide (TGO, Al_2O_3) were reported. The implication was the requirement of an interlayer between the pyrochlores and TGO, which introduced double-layer systems to the TBC literature. Furthermore, processability issues of pyrochlores associated with the different evaporation rates of lanthanide oxides and zirconia resulting in unfavorable composition variations in the coatings were addressed in different studies.

After all, although the material properties are available, there is a paucity of data in the literature concerning the properties of the coatings made of pyrochlores. From the processability point of view the most reported pyrochlore is $La_2Zr_2O_7$. Hence, the goal of this research was to investigate plasma-sprayed $Gd_2Zr_2O_7$ (GZO) coatings and YSZ/GZO double-layer TBC systems. Three main topics were examined based on processing, performance and properties: (i) the plasma spray processing of the GZO and its impact on the microstructural and compositional properties of the GZO coatings; (ii) the cycling lifetime of the YSZ/GZO double-layer systems under thermal gradient at a surface temperature of 1400 °C; (iii) the properties of the GZO and YSZ coatings such as thermal conductivity, coefficient of thermal expansion as well as time and temperature-dependent elastic and creep deformations.

Thermal cycling results displayed that the double-layer YSZ/GZO TBC concept is able to provide significant lifetime improvement at 1400 °C surface temperature compared to the standard YSZ. The investigations on the chemical composition of the as-sprayed GZO revealed that no significant gadolinia evaporation, which would compromise the performance of the coating, takes place in the examined spray current range (300 A-525 A). The detailed examination of microstructural properties of the as-sprayed GZO highlighted the importance of the process parameters for achieving the desired porosity features assisting superior lifetime performances. A significant insight was gained into the elastic and creep deformation of the plasma-sprayed YSZ and GZO coatings which play a critical role on the development of advanced TBCs. The overarching conclusion of this work is that the GZO has the potential to increase the temperature capability of gas turbines, if it is applied in double-layer TBC systems and if its microstructure is tailored by adapted processing.

Kurzfassung

Die Motivation für Forschungsarbeiten an Wärmedämmschichten (WDS) ist das Bestreben, die maximale Gaseintrittstemperatur in Gasturbinen weiter zu erhöhen. Eine Vielzahl von neuen keramischen Materialien für WDS wurden in den letzten Jahrzehnten untersucht, da das üblicherweise verwendete Yttriumoxid-teilstabilisierte Zirkoniumoxid (mit 7 Gew.% Y_2O_3 stabilisiertes ZrO_2, YSZ) oberhalb von 1200 °C eine nur begrenzte Temperaturbeständigkeit im Langzeiteinsatz aufweist. Zirkonat-Pyrochlore großer Lanthanide ($(Gd \rightarrow La)_2Zr_2O_7$) sind dabei aufgrund ihrer besseren Phasenstabilität bei hohen Temperaturen verglichen mit YSZ besonders attraktive Werkstoffe. Allerdings wurden in der Literatur auch Probleme bei der Anwendung von Pyrochloren beschrieben, wie eine niedrige Bruchzähigkeit und eine Bildung schädlicher Mischphasen mit der thermisch gewachsenen Oxidschicht (TGO). Daher wurde eine zusätzliche Schicht zwischen den Pyrochloren und der TGO eingeführt, sodass Doppellagenschichtsysteme Eingang in die WDS-Literatur fanden.
Insgesamt bietet die Literatur keine ausreichenden Daten bezüglich der Eigenschaften der Pyrochlore-Beschichtungen, obwohl Daten zu einzelnen Materialeigenschaften verfügbar sind. Daher war das Ziel dieser Arbeit, plasmagespritzte $Gd_2Zr_2O_7$ (GZO) Beschichtungen und YSZ/GZO Doppellagenschichtsysteme für WDS zu untersuchen. Aufbauend auf den Aspekten der Prozessierbarkeit, Leistung und Eigenschaften wurden drei Schwerpunkte in dieser Arbeit gesetzt: (i) die Abscheidung von GZO über einen Plasmaspritzprozess und der Einfluss auf Zusammensetzung und mikrostrukturelle Eigenschaften der GZO-Schichten; (ii) die Lebensdauern von YSZ/GZO-Doppellagenschichtsystemen beim Thermozyklieren bei einer Oberflächentemperatur von 1400 °C, (iii) die Eigenschaften von GZO- und YSZ-Schichten, wie Wärmeleitfähigkeit, Wärmeausdehnung sowie zeit- und temperatur-abhängige elastische Eigenschaften und Kriechverformungen.
Die Thermozyklier-Ergebnisse haben gezeigt, dass die Doppellagenstruktur aus YSZ/GZO im Vergleich zu üblichen YSZ-Schichten eine signifikante Steigerung der Lebensdauer bei einer Oberflächentemperatur von 1400 °C ermöglicht. Untersuchungen der chemischen Zusammensetzung von gespritztem GZO ergaben, dass für die verwendeten Plasmaströme (300 A-525 A) keine signifikante Gadoliniumoxid-Verdampfung auftritt, welche die Leistungsfähigkeit der Schicht beeinträchtigen würde. Ein detaillierter Vergleich der mikrostrukturellen Eigenschaften gespritzter GZO-Schichten zeigte die Bedeutung der Prozessparameter, um spezielle Porositätskenndaten zu erzielen, die für das Erreichen der überlegenen Lebensdauern notwendig sind. Des Weiteren wurden wichtige Erkenntnisse für das Verständnis der elastischen Eigenschaften und Kriechverformungen der plasmagespritzten YSZ- und GZO-Schichten gewonnen. Die wesentliche Schlussfolgerung dieser Arbeit ist, dass die GZO-Schichten das Potential haben, eine höhere Gaseintrittstemperatur zu ermöglichen, falls die Schichten in Doppellagenschichtsystemen eingesetzt werden und ihre Mikrostruktur mit Hilfe des Abscheideprozesses angepasst wird.

Contents

1 | Introduction and Objectives

Thermal barrier coatings (TBCs) are finding increasing application in the most demanding high-temperature environment of the gas turbine engines used for aircraft propulsion and power generation. The use of TBCs along with internal cooling of the underlying superalloy components provides a temperature drop of up to 300 K in the surface temperature of superalloy components. This provides two main benefits; (i) allowing the engine to operate at temperatures above the melting temperature of superalloys, thereby improving the energy efficiency and performance of the engines and (ii) prolonging the life of the components. The first benefit is of primary importance to the gas turbine industry with its continuous drive to increase the efficiency of the engines.

The TBC technology has been based primarily upon yttria-stabilized zirconia (7 wt.% Y_2O_3 stabilized ZrO_2, YSZ), since its commercial introduction in the 1980's (Stecura, 1978). However, temperature limitation of the YSZ has been the main motivation to modify it chemically or to substitute it with new TBC materials ever since. A major concern is related to its phase stability at elevated temperatures. The non-transformable tetragonal phase (t') of the YSZ coatings, which is the underlying reason of the high cyclic durability and adequate erosion resistance in this material, undergoes phase separations into the equilibrium phases at high temperatures (Miller *et al.*, 1981). Furthermore, there are additional concerns that pertain to loss of in-plane compliance, and hence strain tolerance, either by sintering (Thompson and Clyne, 2001), or by infiltration of molten silicate deposits (CMAS) (Krämer *et al.*, 2006).

The zirconate pyrochlores of the large lanthanides ($(Gd \rightarrow La)_2Zr_2O_7$) offer the opportunity to circumvent many of the issues associated with higher temperature operation. They have been reported to be phase stable, existing in single-phase fields on their binary phase diagrams at high temperatures (Wang, 2006), as well as to have lower thermal conductivity (Maloney, 2000; Lehmann *et al.*, 2003), greater sintering (Vaßen *et al.*, 2000) and CMAS resistance (Krämer *et al.*, 2008) with respect to the YSZ. However, introducing the pyrochlores as single layer top coats to the TBCs was not successful due to their low toughness and the formation of deleterious interphases as a result of diffusional interaction with thermally grown oxide (TGO, Al_2O_3) (Leckie *et al.*, 2005). For that reason, the YSZ was proposed as an interlayer between the pyrochlore and TGO to work as a diffusion barrier as well as to provide high toughness for hindering the propagation of cracks

in the vicinity of the TGO. In the past decade, it was shown that the YSZ/pyrochlore double layer concept is well suited for the TBC systems produced by both atmospheric plasma spray (APS) and electron-beam vapor deposition (EB-PVD) techniques (Vaßen *et al.*, 2004; Xu *et al.*, 2008; Moskal *et al.*, 2012; Liu *et al.*, 2014). Nevertheless, processability issues of pyrochlores associated with the different evaporation rates of lanthanide oxides and zirconia resulting in unfavorable composition variations in the coatings were addressed in different studies (Cao *et al.*, 2001; Saruhan *et al.*, 2004; Mauer *et al.*, 2012). After all, although the material properties are available, there is a paucity of data in the literature concerning the properties of the coatings made of pyrochlores and from processability point of view the most reported pyrochlore is $La_2Zr_2O_7$. Hence, the goal of this research is to investigate plasma-sprayed $Gd_2Zr_2O_7$ (GZO) coatings and YSZ/GZO double-layer TBC systems. Three main topics are going to be examined based on processing, performance and properties: (i) the APS processing of the GZO and its impact on the microstructural and compositional properties of the as-sprayed GZO coatings; (ii) the thermal cycling lifetime of the YSZ/GZO double-layer coatings at a surface temperature of 1400 °C; (iii) the thermophysical and thermomechanical properties of the GZO and YSZ coatings such as thermal conductivity, coefficient of thermal expansion as well as elastic and creep deformations.

This thesis is organized as follows. Chapter 2, immediately following this introduction, covers the background and literature review. In Chapter 3, experimental and characterization methods used in the study will be briefly summarized. The results and discussion will be presented in Chapter 4 and Chapter 5. Relations of plasma spraying process, gadolina evaporation issue and microstructure of the GZO coatings as well as thermal cycling lifetime of YSZ/GZO coatings will be discussed in the Chapter 4. Thermal conductivity and coefficient of thermal expansion of the GZO coatings will be compared with the literature data obtained from powder compacts, while time and temperature-dependent elastic and creep deformations of the YSZ and GZO coatings will be demonstrated in Chapter 5. Finally, a summary and concluding remarks will be given in Chapter 6.

2 | Current Knowledge and Future Demands

2.1 Gas Turbines

Thermal barrier coatings (TBCs) are protective ceramic coatings applied to the surface of hot metallic sections in gas-turbine engines. The major fields of the application of gas turbines are aircraft propulsion and electricity generation, which generates a $42 billion industry worldwide (2010) and is projected to reach $65 billion in 2016 (Langston, 2011, 2012). It was reported that the share of aviation related gas turbines in this market was 65 % (2010) (Clarke *et al.*, 2012). Along with the fact that air travelling is predicted to be doubled in the next two decades (FAA 2011), an inevitable growth in the number of aircraft gas turbines can be anticipated. A similar conclusion can be made for stationary gas turbines taking into consideration of the growing global electricity demand (EIA, 2014).

A schematic of an aircraft gas turbine engine showing the essential parts can be seen in Figure 2.1a. In the engine, a compressor mechanically raises the pressure and the temperature of the air (i), fuel is burned in the combustor to further increase the temperature of the pressurized air (ii) and finally the heated, pressurized air expands through turbine section and spins the blades (iii), which are all described by the Brayton cycle (or Joule cycle) (Miller *et al.*, 1981; Bathie, 1996). The thermal efficiency - ability to convert the chemical energy of the fuel into mechanical work - of the cycle is affected by (i) the ratio of temperature leaving the combustor (i.e., the turbine inlet temperature) to that of the air entering the engine and (ii) the overall pressure ratio between atmospheric pressure and peak pressure within the engine. Figure 2.1b shows gas turbine efficiency as a function of pressure ratio and turbine inlet temperature. The increase of the pressure ratio improves the efficiency when accompanied by the increase in inlet temperature. However, increasing the pressure ratio beyond a certain value at any given turbine inlet temperature can actually result in lowering the overall cycle efficiency (Klein and Nellis, 2011). Nonetheless, the same plot clearly shows the consistent boosting effect of higher inlet temperature on the efficiency, which manifests the crucial inlet temperature-efficiency relations of gas-turbine engines.

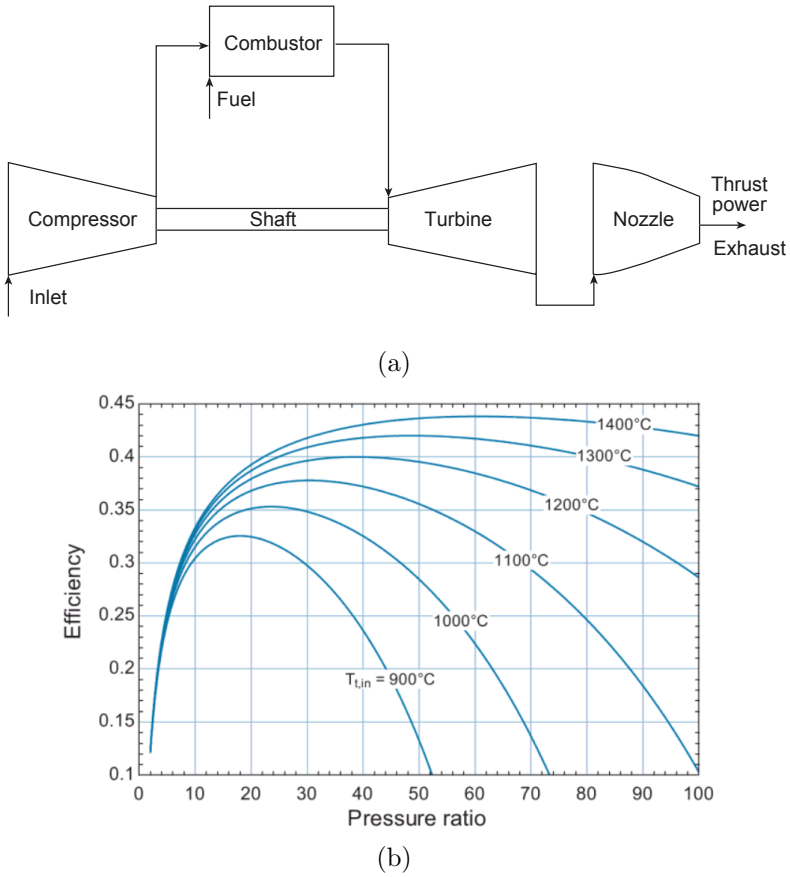

Figure 2.1: (a) Schematic of an aircraft engine (Langston, 2014). (b) The gas turbine efficiency as a function of pressure ratio and turbine inlet temperature Klein and Nellis (2011).

For decades, improving the efficiency by increasing inlet temperatures has been considered for the engine designs. The highest inlet temperature in the engine cycle is limited by the maximum temperature that the adjacent components can withstand. Early attempts to increase gas temperatures introduced cooling systems in the engines, which allow metallic components to survive at higher gas temperatures than their melting points. Subsequently, ceramics were introduced in the form of thermal barrier coatings, which is accepted as the major step in increasing engine temperatures, bonding to metallic surface and protecting it against high temperatures. Additionally, developments on the super alloy materials have been recorded during this time period. Directionally solidified

(DS) and single crystal alloys offered extended creep lifetime and higher temperature capabilities in gas turbine engines (Kingery *et al.*, 1976). Temperature enhancements gained historically by implementing cooling systems and TBCs along with the super alloy developments in the gas-turbine engines can be seen in Figure 2.2. Today, the gas-turbine engines use all these technological developments in combination with the design and manufacturing improvements. Better engine materials including TBCs and associated manufacturing technologies, mechanical design, aerodynamics, cooling technologies are continued to be investigated for further innovations in gas-turbine engine technology.

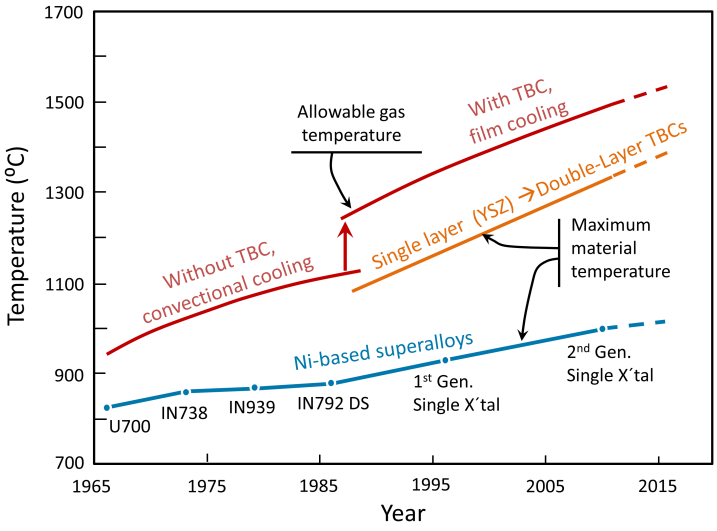

Figure 2.2: Historical perspective of materials and cooling technology development for use in gas turbines. Adapted from (Clarke *et al.*, 2012).

2.2 Thermal Barrier Coating Systems (TBCs)

TBCs were initially introduced to extend the lifetime of stationary gas turbine engine parts such as combustor chamber walls, burner cans and liners in the early 1960s. In the 1970s, National Aeronautics and Space Administration's (NASA) Lewis Research Center developed a two layer TBC system and successfully tested it on turbine blades, which was marked as the beginning of the modern era of TBCs (Stecura, 1977). The system was consisting of an atmospheric plasma sprayed (APS) yttria-stabilized zirconia

(ZrO_2-12 wt. % Y_2O_3) ceramic layer on APS metallic NiCrAlY bond coat. Next year, Stecura presented that lowering the ytrria content of zirconia to 6-8%, which was added to stabilize cubic phase, resulted in superior performances (Stecura, 1978). Whilst first improvement steps of the plasma sprayed TBCs were taken, Pratt&Whitney developed first electron beam physical vapor deposited (EB-PVD) yttria-stabilized zirconia TBCs in the late 1970s (Miller, 1997). These two methods – APS and EB-PVD- have been developed ever since and today known as the established methods for manufacturing of the TBC top coat layers. Similarly, despite intense investigations on the alternative TBC materials, partially-yttria-stabilized zirconia (6-8 wt. % Y_2O_3) is the state-of-the-art top coat material of current TBCs.

The conventional TBCs systems typically consist of an insulating porous ceramic top coat (i), a metallic bond coat (ii), which is more oxidation resistant than the superalloy engine part, and a thermally grown oxide "TGO" layer (iii) that forms between top coat and bond coat due to oxidation of bond coat in service (Figure 2.3). As it is illustrated in Figure 2.3, TBCs are complex systems consisting of ceramic and metallic interactive layers. At high operation temperatures materials of these layers experience e.g. phase transformation, diffusion, oxidation, corrosion, thermal expansion, creep, fatigue, sintering phenomena which all interact with each other. This makes predictability and reliability of the performance of TBCs quite complicated. The current research on the TBC technology focuses on solving these interaction related issues of the TBC layers in order to guarantee that each component maintains its properties and the system can perform reliably during the desired lifetime. In the following sections, functions of each TBC layer illustrated in the Figure 2.3 will be discussed along with the material properties and production routes.

2.2.1 Superalloys of Turbine Engine Parts

The development of the superalloys over the past decades has considerably contributed to a better high temperature capability of the components. From the first wrought alloys such as U700 in the 1960s to the most modern single-crystal alloys of nowadays, the gas inlet temperature in turbo-machines could be increased about 200 K as depicted before in Figure 2.2.

The superalloy components such as blades and vanes are typically fabricated by investment casting which is essential for the utilization of complex cooling arrangements and also for grain structure control. These components can be casted in the form of polycrystals or single crystals. The grain boundaries in the polycrystalline structures function as

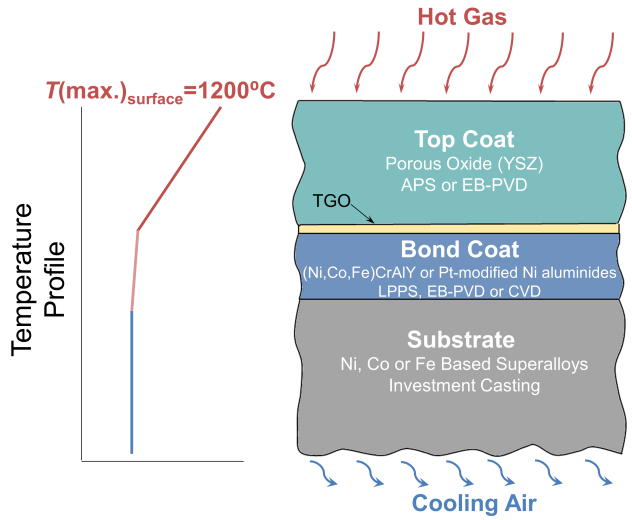

Figure 2.3: Schematic structure of a thermal barrier coating system with an expected temperature gradient through the system. Typical materials and production routes of top coat, bond coat and substrate are indicated. (APS: Atmospheric Plasma Spray, EB-PVD: Electron Beam Vapor Deposition, LPPS: Low Pressure Plasma Spray, CVD: Chemical Vapor Deposition)

weakness sites at elevated temperatures resulting in inferior creep and strength properties. Therefore, single crystal alloys are typically preferred at hot section engine parts such as turbine blades and the polycrystalline alloys are used in colder sections (Pollock and Tin, 2006).

Nickel and cobalt based superalloys, which both can be hardened by precipitation hardening mechanism, are predominantly employed in gas turbines (Sims *et al.*, 1987). Addition of iron into the nickel based superalloys led to introduction of nickel-iron based sub group alloys and Inconel 718 to the turbine engine industry in 1950s, which is known as the most popular and widely used alloy for turbines in the world. Notwithstanding, the cobalt based alloys do have other advantages such as higher melting points, better environmental resistances and also better weldability, which can make them favourable for static components where the high strength is not required (Campbell, 2008).

In the precipitation hardening mechanism, addition of aluminium, titanium, tantalum and niobium into a supersaturated γ-nickel matrix results in precipitation of intermetallic γ' [$(Ni_3(Al, Ti, Ta, Nb)]$ compounds. γ' forms small cubic crystals that inhibit slip and creep effectively at elevated temperatures which is accepted as the key strengthening method of nickel based superalloys (Sims *et al.*, 1987) (Figure 2.4). Solid solution

strengthening of the γ-nickel matrix is obtained by adding refractory elements such as Mo, W, Nb and Re into alloy (Pollock and Tin, 2006). This combination of precipitation and solid solution hardening of nickel based superalloys provides their superior high temperature capabilities.

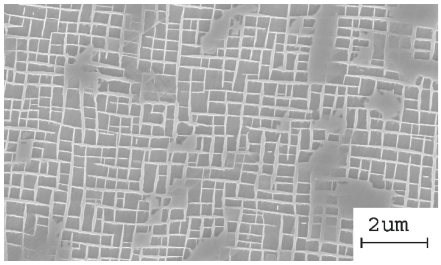

Figure 2.4: Typical γ-γ´ microstructure for a single crystal nickel based superalloy (Pollock and Tin, 2006).

Although it is eliminated for single crystal alloys, carbides and borides are used as grain boundary strengtheners in polycrystalline superalloy systems with the minor additions of Hf, Zr, W, Mo, V, Cr. Besides the strengthening, enhancement of the specific properties such as oxidation resistance (Al, Cr, Y, La, Ce), hot corrosion resistance (La, Th) creep resistance (B, Ta) of the nickel based superalloys is also provided by addition of the given elements (Davis and Committee, 2000). On the other hand, studies showed that the unavoidable impurities in the ppm levels such as S, As, Se, Te, which accompany the beneficial alloying elements, can affect the mechanical properties and oxidation resistance of the alloys adversely (Bouse and Mihalisin, 1989).

It was reported that many nickel based alloys contain a combination of five to ten of these alloying elements up to 40 wt.% (Pollock and Tin 2006). However these elements, which are essential for high temperature strength of alloy, undergo diffusion through the bond coat (occasionally through the top coat) during operation at high temperatures and can play a critical role in the spallation of TBCs (Kaden *et al.*, 1999).

2.2.2 Bond Coat and Thermally Grown Oxide (TGO)

The bond coat lying between the substrate and the ceramic top coat in the TBC plays a critical role in the system. It has the primary functions of protecting the substrate from oxidation and providing adherence of the top coat. The growth of the TGO at the bond coat - top coat interface during engine operation is the most important phenomenon

responsible for the spallation failure of TBCs. For that reason, the failures associated with the bond coat and TGO characteristics will be also discussed in this section.

Currently used bond coat alloys are: (i) MCrAlY (M=Ni, Co) which can be applied by either low-pressure or vacuum plasma spray (LPPS or VPS are two different designations for the same process) (Miller, 1987), or electron-beam physical vapour deposition (EB-PVD) (Schulz *et al.*, 2003), (ii) aluminides of Ni and Pt are deposited by electroplating in conjunction with diffusion aluminizing (Schulz *et al.*, 2003). In the LPPS, a high-temperature plasma spraying is performed in a low-pressure argon atmosphere, which enables to spray metallic materials that are sensitive to oxidation. At the TBC operation temperatures, bond coat oxidation occurs as a result of oxygen inward diffusion to the bond coat through the porous top coat. This results in the formation of a thermally grown oxide (TGO) layer between bond coat and top coat (Figure 2.3).

Since the formation of the TGO is inevitable, the bond-coat compositions are selected as Al rich to form an alumina (α -Al_2O_3) TGO. So that in addition to oxygen inward diffusion to the bond coat, aluminum outward diffusion controls the alumina growth leading to the formation of the new oxide at the TGO-top coat interface or at the grain boundaries within the alumina scale. Alumina is the preferred TGO because it is (i) the slowest growing oxide at high temperatures (Clarke *et al.*, 2012), (ii) an excellent oxygen diffusion barrier due to its very low oxygen diffusivity (Sims *et al.*, 1987), (iii) phase compatible with typical top coat material-yttria-stabilized zirconia (YSZ) (Meier and Pettit, 1992) and (iv) it forms an adherent layer with excellent mechanical integrity (Padture *et al.*, 2002). These are important because TGO thickness can induce the TBC failure when it exceeds a critical thickness, when the release of stored elastic strain energy in the coating system exceeds the fracture resistance. TGO thickening and lateral alumina growth strain associated stresses as well as thermal expansion mismatch stresses are counted as the main stress contributors in the TGO layer (Clarke *et al.*, 2012).

The TGO composition, morphology, growth rate, adherence, stress levels and hence the failure of TBC are strongly affected by composition and roughness profile of the bond coat. The roughness is an important factor in particular for plasma sprayed TBCs. Because they are sprayed on the rough bond coat surfaces to ensure mechanical clamping, whereas smooth bond coat surface profiles are preferred in TBCs manufactured by EB-PVD. Thereby, an optimized composition and roughness of the bond coat are considered as two factors to improve TBC lifetime, and their relations with properties and the TBC failure will be discussed here.

In terms of high temperature oxidation and corrosion resistance, MCrAlY bond coats are claimed as the superior to the Pt-modified aluminides (Nicholls, 2000). Specifically, high

Al and Cr contents in MCrAlY are found to be beneficial for the oxidation and corrosion resistance but at the same time harmful for the coating fatigue resistance (Birks *et al.*, 2006). Al depletion, on the other hand, in the bond coat after long exposure times due to Al outward diffusion leads to formation of non-protective Ni and Co containing oxides, e.g. spinel (Figure 2.5), which can provide sites for initiation and propagation of failure relevant cracks (Shillington and Clarke, 1999; Rabiei and Evans, 2000). Function of Y in MCrAlY is more sophisticated; while it was observed that small additions of Y (0.1-1 wt. %) improve the alumina scale adherence, it was found that the high Y content result in the formation of mixed Y-Al oxides such as $Y_3Al_5O_{12}$ (YAG: yttrium aluminum garnet) and $YAlO_3$ (YAP: yttrium aluminum perovskite) in the alumina layer (Gudmundsson and Jacobson, 1989). Some research results supported that these mixed Y-Al oxides enhances the alumina scale adhesion (Song, 2012), whereas some other indicated that they are detrimental for the adhesion due to their different CTE (coefficient of thermal expansion) from alumina (Nijdam and Sloof, 2007). In addition to affecting the adhesion of alumina scale, it was shown that the Y in higher concentrations also increases the growth rate of alumina scale (Dunin-Borkowski *et al.*, 1996). The reason of the increase in the growth rate was explained by short-circuit paths for the inward oxygen transport provided by incorporated Y-oxides in alumina scale (Pint, 2003). Figure 2.5 shows an example of such incorporated yttrium aluminate precipitates (pegs) in the oxide scale. After all, there is still no general agreement in the literature concerning the mechanisms elucidating the effects of Y-oxides on the oxide scale. But obviously it is an important factor to control Y concentration of the bond coat alloys for the performance of the protective oxide in TBC system.

Bond coat roughness was also found to affect the morphology of protective oxide layer leading to inhomogeneous depletion of Al and Y in concave and convex regions (Gil *et al.*, 2006). Gil et al. studied on flat and rough bond coat surfaces and found that oxide scale morphologies grown on these different surface profiles are different. The alumina scale is thinner and contains less Y-Al pegs in the convex surfaces than the concave surfaces of the rough bond coat (Figure 2.5), which might explain the earlier spallation frequently observed at convex surfaces.

There are a numbers of other elements such as Re, Ta and so-called reactive elements (e.g. Hf, Ce, Zr) that are added in small amounts to MCrAlY bond coats for different purposes. For instance, the segregation of S at the interface of bond coat and TGO is known as detrimental and to mitigate this effect reactive elements (Zr, Y) are added to bond coat composition (Smialek *et al.*, 1994). Some of the properties of MCrAlY bond coats changed by addition of these specific elements are given in Table 2.1.

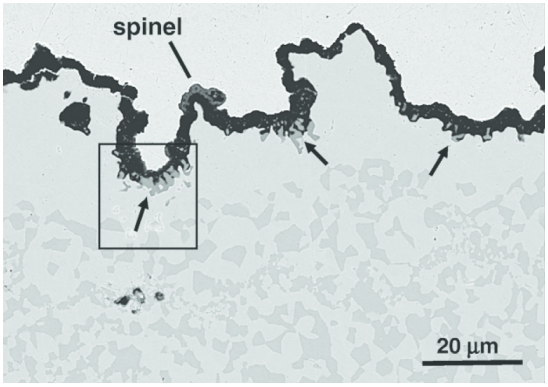

Figure 2.5: SEM cross-section of rough NiCoCrAlY bond coat after 25h isothermal oxidation at 1100 °C. Arrows indicate Y-Al oxide pegs and spinel formation at the convex TGO surfaces adjacent to the bond coat and TBC, respectively. Al depletion is also visible from contrast difference in the bond coat (Gil *et al.*, 2006).

Table 2.1: Influence of different material additions in MCrAlY bond coats

Elements	Influenced properties of MCrAlY bond coat	References
Re	thermo-mechanical fatigue resistance	(Czech *et al.*, 1994)
Ta	yield strength and creep resistance	(Taylor and Bettridge, 1996)
Ce, Hf	oxidation resistance, mechanical properties, suppressing the metastable alumina growth	(Ogawa *et al.*, 2006) (Goward, 1998) (Haynes *et al.*, 2002)(Hayashi and Gleeson, 2009)
Co	increase of the CTE of the bond coat	(Toscano *et al.*, 2007)

2.2.3 Ceramic Top Coat

The main function of the ceramic top coat in TBC systems is providing thermal insulation for the metallic engine part and bond coat. However, there are a numbers of other requirements that the top coat needs to fulfill. As mentioned before, 6-8 wt. % YSZ remains the material of choice for TBC top coat since it was introduced in 1970s (Stecura, 1978). As YSZ is a great combination of desired properties, although it has the major temperature capability limitation at long term operation, it was not possible to substitute it with other materials in the last few decades. In this regard, the requirements of the top coat and the limitations of the YSZ along with the top coat associated failure mechanisms will be summarized below.

A high melting point, low thermal conductivity and a *high thermal expansion coefficient*, are the main required properties for a thermal insulating ceramic material on top of metallic components. YSZ has a high melting point (∼2700 °C) and one of the lowest thermal conductivities of all ceramics at elevated temperatures; conductivity of dense YSZ was reported as 2.6 W/mK (5.3 wt. % YSZ, 600 °C) (Hasselman *et al.*, 1987) and as 0.7-1.4 W/mK for the coatings (7.25 wt. % YSZ) with different microstructures and porosity (Pawlowski *et al.*, 1985).

YSZ also has a high thermal-expansion coefficient ($11 \times 10^{-6}\,K^{-1}$), which is almost comparable to that of the underlying superalloy substrate ($14 \times 10^{-6}\,K^{-1}$) (Cao *et al.*, 2004) and helps to mitigate stresses arising from the thermal-expansion mismatch. But a mismatch still remains and for that reason the porosity and cracks (inter-lamellar cracks, segmentation cracks etc.) are deliberately introduced to the top coat via processing in order to maximize the strain tolerance of it.

APS and EB-PVD, two standard processing techniques for the top coat deposition, both enhance the thermal insulation efficiency and thermal expansion compliance of the ceramic materials in different ways and extents. In APS process, an electric arc generated between anode and cathode ionizes the flowing process gases (argon, hydrogen, nitrogen or helium) into the plasma state (Figure 2.6). The ceramic powder particles are injected into this plasma jet where they are heated and accelerated towards the substrate, so that the molten or partly molten particles impact the surface of substrate at high speed. This leads to deformation of the particles and spread like "pancakes" or so-called "splats" (1 to 5 μm thick, 200 to 400 μm diameter) (Padture *et al.*, 2002; Pawlowski, 2008). Heat from the hot particles is transferred to the cooler substrate material and the splats rapidly solidify and shrink. Figure 2.7a shows a plasma sprayed YSZ microstructure consisting of mechanically interlocked splats. As a result of quenching of the splats and their imperfect contacts, inter-splat, intra-splat cracks and larger spherical pores are introduced to the microstructure. Depending on the temperatures of the sprayed particles, unmelted particles can also be obtained in the microstructure contributing to the fine porosity. Thus, the cumulative porosity (15-30 vol. %) of the as-sprayed microstructure lower the thermal conductivity (in particular the inter-splat cracks aligned parallel to the substrate surface and normal to the heat flux) and the elastic modulus of the ceramic top coat for better thermal insulation and strain tolerance, respectively.

However, plasma sprayed coatings often show spallation failure due to stored strain energy in porous coatings during thermal cycling processes. The thermal expansion mismatch of metallic substrate and ceramic coating induces tensile stresses in the coating at high temperatures. Relaxation of tensile stresses at high temperatures results in development

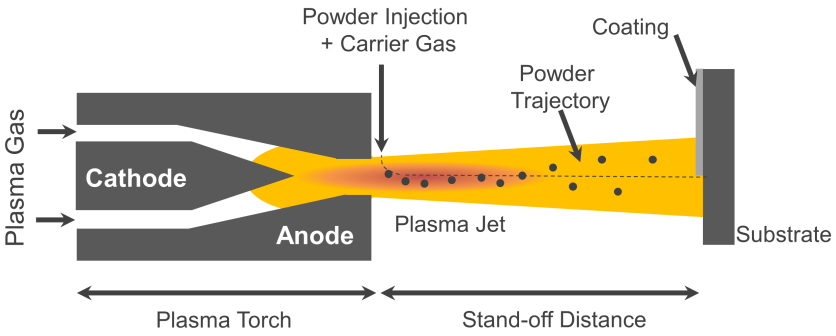

Figure 2.6: Schematic of plasma spraying process with powder injection. Reproduced from Fauchais *et al.* (2014).

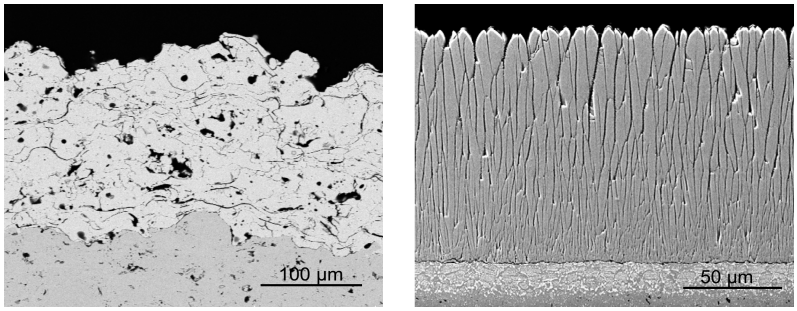

(a) (b)

Figure 2.7: Cross-section microstructures of YSZ deposited with (a) APS, (b) EB-PVD (Lee, 2005).

of compressive stresses in the coating after fast cooling to room temperature leading to crack propagation and hence shorter lifetime (Matejicek *et al.*, 1999). Therefore, one possible way to improve thermal shock resistance and cycling performance of plasma-sprayed coatings is reducing the tensile stress level before cooling which requires microstructural modifications. Highly porous coatings from plastic-ceramic mixed powder, different gradient and layered structures were studied for that purpose (Gualco *et al.*, 1997; Gao, 2008; Lee *et al.*, 1996). Segmentation cracks which are the vertical cracks running perpendicular to the coating surface were introduced to the top coats by manipulating spray conditions. These cracks have successfully improved the strain tolerance of the top coat by opening during tensile loading, similar to EB-PVD coatings which will be discussed below, and yielded successful thermal shock performances with respect to standard porous coatings (Taylor *et al.*, 1990; Karger *et al.*, 2011). The disadvantage of these modification was an

increased thermal conductivity resulting from decrease in the cumulative porosity due to well-bonded splats obtained with high substrate temperatures and the cracks parallel to the heat flux.

In the EB-PVD process, a high energy electron beam is used to heat and vaporize the coating material. The pre-heated substrate is inserted into the vapor cloud and the vapor condenses onto the surface of the substrate, forming a coating in a columnar structure with inter-column pores running through the coating thickness (Figure 2.7b). The columnar structure of EB-PVD exhibits a great strain tolerance but also higher thermal conductivities with respect to the conventional porous plasma sprayed coatings. Therefore, in general EB-PVD coatings are preferred because of their greater strain tolerance for the applications where frequent cycling will occur, even though they are inferior to APS coatings regarding thermal insulation. A recently proposed thermal spray technology that should be mentioned here is called plasma spray-physical vapor deposition (PS-PVD). It uses a high energy plasma gun operated in an inert atmosphere at reduced work pressures (50-200 Pa) which enables to vaporize fine feedstock material and to produce layers in shape of columns out of the vapor phase similar to EB-PVD (Figure 2.8a). Apart from high strain tolerance microstructure, PS-PVD offers lower investment costs and 10-100 times higher deposition rates than the EB-PVD along with the ability of coating complex geometries and shadowed areas (Niessen *et al.*, 2010). Recently it was also reported that thermal cycling lifetimes more than two times higher than conventionally sprayed TBCs were obtained with optimized PS-PVD process conditions (Rezanka *et al.*, 2014).

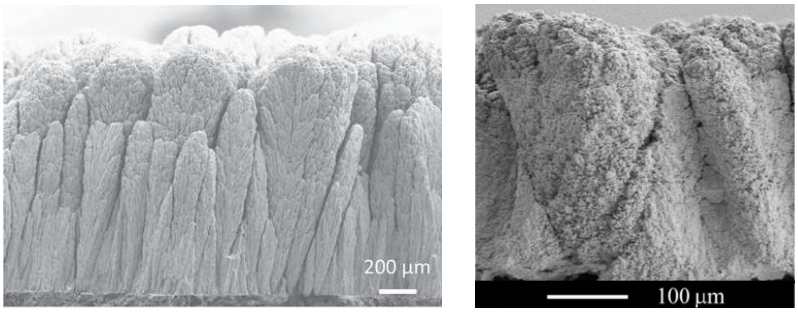

(a) (b)

Figure 2.8: Fracture surface of a columnar YSZ microstructure produced by PS-PVD (Mauer *et al.*, 2013) (a) and SPS (VanEvery *et al.*, 2011) (b) .

As another innovative plasma spray technique so-called “Suspension Plasma Spray (SPS)” was introduced, which employs a liquid chemical precursor instead of powder feedstock

likewise APS. High segmentation crack density and high cumulative porosity mainly consisting of sub-micrometer range pores were obtained with this technique (Figure 2.9).

Figure 2.9: Cross section of an as-sprayed SPS YSZ free standing coating with segmentation cracks (Guignard *et al.*, 2012).

As a result of these, research results showed that (i) thermal conductivity of SPS coatings are in a similar range with that of APS porous coatings and lower than the APS segmented coatings, (ii) thermal shock resistance and strain tolerance of the SPS coatings are larger than the APS coatings, (iii) thermal cyclic performance of SPS coatings are superior to APS coatings (Pawlowski, 2009; Guignard *et al.*, 2012; Curry *et al.*, 2014). Latest research also showed that the SPS is a suitable process for the deposition of columnar-structured coatings (Figure 2.8b) (VanEvery *et al.*, 2011).
The newer thermal spray technologies seem already to surpass the capabilities of the APS presenting highly strain tolerant and porous coatings. On the other hand, maintenance of strain tolerance and porosity requires the *sintering resistance* and *phase stability* of the top coat material at high application temperatures. Unfortunately, YSZ shows insufficient phase stability and accelerated sintering at temperatures above 1200 °C, which are known as two degradation mechanisms of plasma sprayed YSZ TBCs (Vaßen *et al.*, 2000). At room temperature, a non-equilibrium, high-yttria containing tetragonal phase (t', also called non-transformable tetragonal) is observed in as-sprayed YSZ coatings (Figure 2.10a). The t' phase is formed due to rapid cooling during deposition process, which prevents the necessary compositional adjustments for the formation of equilibrium phases (low-yttria containing transformable tetragonal and high-yttria containing cubic), therefore very small amounts of the equilibrium phases are observed in the as-sprayed microstructures. However, the t' phase undergoes phase separations into the equilibrium phases at high temperatures (Figure 2.10b) (Miller *et al.*, 1981) resulting in degradation of the coating. Because, the transformation of the low-yttria containing tetragonal phase into the monoclinic phase upon cooling is accompanied by a volume change (Scott, 1975; Chevalier *et al.*, 2009), which is detrimental for the integrity of the coating and the high-yttria containing cubic phase displays low toughness (Marrow *et al.*, 1994; Mercer

et al., 2007). Furthermore, the enhanced sintering leads to decrease in the porosity which results in an increase in Young's modulus and decrease in the thermal resistance of the coating (Zhu and Miller, 2000).

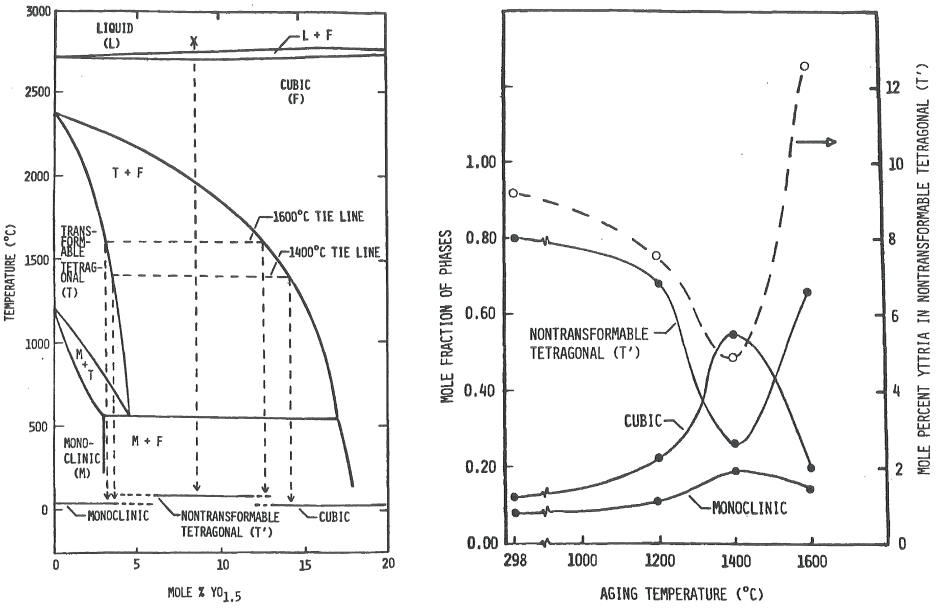

(a) (b)

Figure 2.10: (a) Low-yttria region of ZrO_2-Y_2O_3 phase diagram, (b) mole fraction of the phases in the as-sprayed and 100h-aged YSZ specimens (Miller *et al.*, 1981).

Similar to thermomechanical compatibility of the components in the TBC system, *thermochemical compatibility* is also a critical factor for the durability. Interactions between the TGO and ceramic top coat can result in replacing the alumina with less protective oxides and hence can be deleterious for the system. In the literature, ZrO_2 and alumina are reported as thermochemically compatible at the expected upper temperature limit for the TGO/TBC interface (∼1200 °C), which means their solubility is very limited in each other and they don´t have interphases. However higher additions of yttria to the system introduce a concentration boundary for the compatibility (Lakiza and Lopato, 1997). Because yttria (addition above 20 %) and alumina form an aluminate compound (garnet) at 1250 °C (Lakiza and Lopato, 1997; Fabrichnaya and Aldinger, 2004).
After intrinsic issues lead to degradation of the TBC system, there are also extrinsic degradation mechanisms such as *erosion, FOD (foreign object damage), hot corrosion and CMAS (initials of calcium-magnesium alumina-silicate) attack.* Erosion and FOD

are leading to the progressive loss of thickness and total coating removal, respectively (Nicholls *et al.*, 1999). Small particles ingested into turbines and internally generated larger particles (such as engine wear residues, thermally spalled TBC from the combustor) contribute to erosion damage, while any foreign objects such as rocks, ice from the wings in case of FOD impact the components of the engine and can have disastrous consequences. Nicholls *et al.* (1999) studied the erosion behavior of plasma sprayed and EB-PVD coatings and reported that erosion of the plasma sprayed coatings result in a fracture through loosely bonded splat boundaries leading to removal of large coating parts, while erosion occurs in the surface region of EB-PVD coatings leading to smaller localized damage. Hot corrosion of TBC occurs due to molten deposits resulting from impurities in the fuel; the impurities such as sodium, sulfur, vanadium, lead and phosphorus are oxidized during combustion to form strong acidic or alkaline oxides that attack both the ceramic and metallic components of the TBC system. It was found that the Y_2O_3 in YSZ thermal barrier coatings react strongly with the V_2O_3 resulting in formation of YVO_4, which depletes yttria from the zirconia matrix and causes the spallation of TBC (Jones, 1997). Furthermore, molten oxides permeate to the bond coat through the YSZ top coat and lead to accelerated oxidation of the bond coat. Different approaches were introduced to improve the corrosion resistance of YSZ such as altering the yttria content or the stabilizer of the zirconia matrix. Scandia, yttria-stabilized zirconia was found as more corrosion resistant to vanadate hot corrosion, but also some stabilization issues of it was reported by (Jones *et al.*, 1996). A similar erosion mechanism at high operation temperatures is caused by the environmentally ingested airborne sand/ash particles melt on the hot TBC surfaces resulting in the deposition of the CMAS glass deposits (Stott *et al.*, 1994; Mercer *et al.*, 2005; Krämer *et al.*, 2006). The CMAS rapidly penetrate the porosity of the coating and lead to premature failure of the coating as a consequence of mechanical and chemical interactions. Former leads to loss of strain tolerance of the YSZ coating, while the latter result in the destabilization of the YSZ. Due to presence of the CMAS in the structure with much lower CTE than the YSZ top coat and metallic components, large compressive stresses develop upon cooling increasing the energy release rate of the system. The CMAS were also reported as lowering the yttria content of the YSZ, which results in the formation of transformable monoclinic zirconia as discussed above, and consequently compromising the integrity of the system (Krämer *et al.*, 2006). From mechanical point of view, the CMAS induced degradation relies on progressing of the molten deposits through the pores of the top coat surface. Therefore the surface porosity of the top coat becomes critical and makes EB-PVD top coat microstructures particularly vulnerable to the CMAS attack. From chemical point of view, Aygun *et al.*

(2007) showed that up to 20 mol.% Al_2O_3 and 5 mol.% TiO_2 additions into YSZ enable to mitigate CMAS attack by incorporation of both Al and Ti solutes with CMAS glass. Later, it was also shown that increasing the yttria content of zirconia increase the CMAS resistance (Li *et al.*, 2014), although other issues related to phase stability are manifested in that case.

2.2.4 Alternative Ceramic Top Coat Materials

As previously mentioned, some of the properties of the ceramic top coats such as thermal conductivity and strain tolerance can be modified to a certain extent through the processing techniques, although such properties may not persist at high temperatures. On the other hand, changing some other intrinsic material properties such as melting point, phase stability can be only possible with the modification of the crystal structure or by using alternative materials. During the last decade, a number of ceramic materials have been suggested as new top coat materials mainly due to the limited temperature capability of state of the art YSZ above 1200 °C, which necessitates its substitution in advanced gas turbines. Zirconia doped with different rare-earth cations (defect cluster TBC's), perovskites, aluminates and pyrochlores are the main material groups introduced as new candidates and a number of reviews exist in the literature covering this topic (Arnault *et al.*, 1999; Stiger *et al.*, 1999; Vaßen *et al.*, 2010; Levi, 2004; Cao *et al.*, 2004; Schulz *et al.*, 2004). Table 2.2 shows a summary of some of these selected material groups and their properties, while the pyrochlores will be discussed more in detail in the following section.

In defect cluster TBC's, the zirconia is doped with oxides of the different rare-earth cations, which have distinctively different ionic sizes, to produce thermodynamically stable but highly defective lattice structures. The obtained lattice distortion was intended to scatter lattice and radiative photon waves to reduce the thermal conductivity of the coating. In this way, for instance, the thermal conductivity of the zirconia doped with 5.5 mol% Y_2O_3-2.25 mol% Gd_2O_3-2.25 mol% Yb_2O_3 is reduced to 1.6-1.9 W/mK from 2.3 to 2.6 W/mK of ZrO_2-4.5 mol% Y_2O_3 and good thermal cycling performances were obtained (Zhu and Miller, 2004).

The aluminates with magnetoplumbite structure, on the other hand also yielded lower thermal conductivities than standard YSZ as well as low Young´s moduli and high fracture toughness. These good combination of properties, which explain the good thermal cycling performance at high temperatures, are mainly attributed to platelets morphology of calcined granulate (Friedrich *et al.*, 2001). However, recrystallization issues of partly

Table 2.2: Ceramic materials suggested as a substitute of YSZ top coat and their selected properties.

Material group	Composition / Example	Improved properties, advantages	Drawbacks	Ref.
Defect cluster zirconia	ZrO_2-Y_2O_3-Gd_2O_3-Yb_2O_3	◗ Reduced thermal conductivity ◗ Lower thermal conductivity increase rates within the time ◗ Increased thermal cycling performance with moderate dopant concentrations	◗ Reduced thermal cycling performance with high dopant levels due to cubic zirconia stabilization	Zhu *et al.* 2004, Zhu and Miller 2004, Vaßen *et al.* 2010
Aluminates	(La, Nd)$MAl_{11}O_{19}$ (M =Mg, Mn to Zn, Cr or Sm)/ $LaMgAl_{11}O_{19}$	◗ Long term thermochemical stability up to 1400°C ◗ Significantly lower sintering rate ◗ Low thermal conductivity ◗ Segmentation crack networks in APS coatings	◗ Recrystallization of partly amorphous as-sprayed coating during annealing is accompanied by a large decrease in the volume of the coating	Schäfer and Gadow 1999, Friedrich *et al.* 2001, Gadow and Lischka 2002, Gadow and Schäfer 2006
Perovskites	Zirconates $AZrO_3$ (A=Sr, Ba, Ca)/$SrZrO_3$ Complex forms ABO_3 (A= Ba, La, B=(paired Mg, Ta, Al, La)/ $Ba(Mg_{1/3}Ta_{2/3})O_3$	◗ Good thermal cycling performance of Gd-Yb doped $SrZrO_3$/YSZ double layer system above 1250°C	◗ Undesirable phase transformation of $SrZrO_3$ at about 700°C ◗ Inferior toughness vs. YSZ ◗ Preferential volatilization of constituents of the complex perovskites during processing	Ma *et al.* 2008b, Ma *et al.* 2008a, Jarligo *et al.* 2010

amorphous plasma sprayed coatings and Mg evaporation during EB-PVD complicate the processing of the material (Vaßen *et al.*, 2010).
The perovskites were considered as candidate materials mainly due to their high melting temperatures ($SrZrO_3$; 2800 °C, $Ba(Mg_{1/3}Ta_{2/3})O_3$; 3100 °C) (Tarvin and Davies, 2004; Ma *et al.*, 2008b). However, it was found that $SrZrO_3$ undergoes some phase transformations and the one from orthorhombic to pseudo-tetragonal which occurs at 740 °C involves a volume change of 0.14 %, while formation of $Ba(Mg_{1/3}Ta_{2/3})O_3$ is accompanied by secondary phases (Ma *et al.*, 2008b). Ma *et al.* reported that doping the $SrZrO_3$ with Yb_2O_3 and Gd_2O_3 not only suppresses the phase transformation but also lowers the thermal conductivity of $SrZrO_3$ (∼20 %) and yields longer cyclic lifetimes than the standard YSZ particularly in a double layer system.

2.3 Pyrochlores

The pyrochlores are named after the mineral pyrochlore, $(NaCa)(NbTa)O_6F/(OH)$, with which they share a similar structure. Pyrochlore cubic crystal with the formula of $A_2B_2O_7$, where A and B are 3+ or 2+ and 4+ or 5+ cations, respectively, can accommodate a wide compositional range due to flexibility of the structure (Subramanian *et al.*, 1983). Elemental versatility of pyrochlores provides a number of interesting properties and hence diverse application areas to pyrochlores such as cathode and electrolyte materials for fuel cells (Burggraaf *et al.*, 1981; Porat *et al.*, 1997), catalysts (Goodenough and Castellano, 1982; Korf *et al.*, 1987), encapsulation of the nuclear wastes (Dosch *et al.*, 1984) and finally the thermal barrier coatings (Maloney, 2001).
Zirconates pyrochlore of the large* lanthanides (rare earth elements) ($(Gd{\rightarrow}La)Zr_2O_7$) have been particularly attractive for the thermal barrier coatings mainly due to their lower thermal conductivities and phase stability at higher temperatures than the standard YSZ. There are other aspects that make this material group favorable and they will all be discussed below.

2.3.1 Crystal Structure and Low Thermal Conductivity Relations

The pyrochlore crystal structure ($A_2B_2O_7$ or $A_2B_2O_6O'$) with the space group of $Fd\bar{3}m$ is commonly described by following four crystallographically unique atom positions with

*Large in terms of ion radius. Lanthanide ion radius decreases with increasing mass number and is known as lanthanide contraction (Barrett and Malati, 1997).

Wyckoff notations; 16d (A sites), 16c (B sites), 48f (O sites) and 8b (O' sites) (Subramanian *et al.*, 1983). The pyrochlore structure can essentially be considered as an ordered superstructure of anion-deficient fluorite structure, which makes it more convenient to visualize. Figure 2.11 pictures the close relationships between the fluorite and pyrochlore crystal structures schematically.

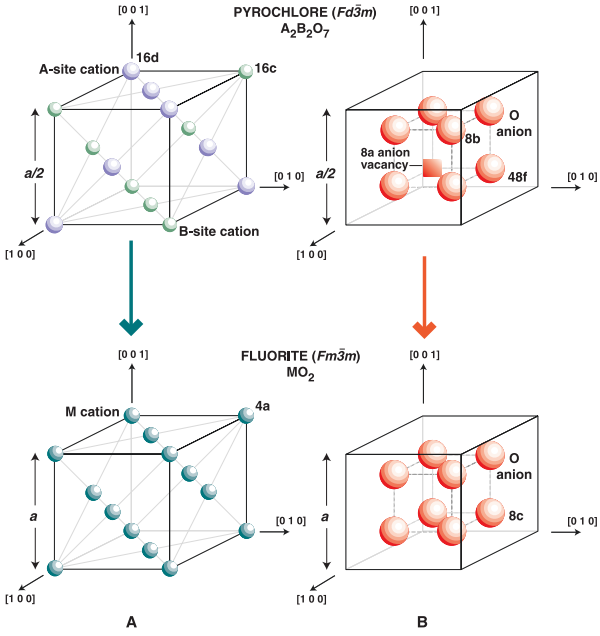

Figure 2.11: Comparison of the cation (A) and anion (B) arrangements in the unit cells of pyrochlore and fluorite compounds (Sickafus *et al.*, 2000).

In the ideal fluorite structure (MO_2, $Fm\bar{3}m$), the oxygen ions are located in the equivalent tetrahedral sites of an M face-centered cubic array. Similarly in pyrochlores, two types of A and B cations form the face-centered cubic array exhibiting an alternating ABAB order at 16c and 16d sites in <110> directions, which result in doubling of the lattice parameter (a) with respect to the fluorite structure. However due to this cation ordering in the pyrochlores, tetrahedral anion sites are no longer crystallographically identical; three distinct tetrahedral sites exist in the structure: the 48f, the 8a and the 8b. Six oxygen atoms occupy the 48f sites with two A and two B neighbors, while the seventh oxygen occupies the 8b site surrounded by four A cations. The 8a site remains vacant in the pyrochlore structure, thereby 87.5% of the tetrahedral sites are filled in the pyrochlore structure while in the ideal fluorite all of them are occupied. The only

variable crystallographic position of the $A_2B_2O_7$ structure is the x position of 48f oxygen ($0.3125 \leq x < 0.375$), where 0.375 indicates the ideal fluorite position, and it is one of the structural parameters used to describe pyrochlore solid solutions along with the lattice constant. The stability of the pyrochlore structure is governed by the ratio of the ionic radii of A and B cations ($1.46 \leq rA/rB \leq 1.80$). Due to this fact, for instance, zirconates of smaller Dy, Er or Yb cations ($(Dy,Er,Yb)_2Zr_2O_7$) adapts to a defect fluorite structure, while gadolinium zirconate ($Gd_2Zr_2O_7$) crystallize in the pyrochlore structure with 1.46 radii ratio at the pyrochlore/defect-fluorite structural boundary. (Subramanian *et al.*, 1983).

In the pyrochlore structure, mixing of the A and B cations at the 16c and 16d sites forms anti-site defects, while the 48f oxygen ion fills the unoccupied 8a site to form interstitial defects (Minervini *et al.*, 2000);

$$A_A^x + B_B^x \rightarrow A_B^{'} + B_A^{\bullet} \tag{2.1}$$

$$O_{O(48f)}^x \rightarrow V_{O(48f)}^{\bullet\bullet} + O_{i(8a)}^{''} \tag{2.2}$$

where $A_B^{'}$ and $B_A^{\bullet}$ denotes the substitution of A^{3+} and $B^{+4}$with each other in Eq.(2.1). In Eq.(2.2), $V_{O(48f)}^{\bullet\bullet}$ shows the vacancy at a 48f site and $O_{i(8a)}^{''}$ is a Frenkel defect at an 8a site. The cation anti-site and following Frenkel defects are considered as the lowest-energy intrinsic disorder mechanisms in pyrochlores (Wilde and Catlow, 1998). Minimization of these defects by more ordered arrangement of cations and the distribution of the oxygen ions implies the ordering of the pyrochlore structure.

The thermal conductivity of dielectric solid oxides (k) in the absence of any defects is controlled by phonon-phonon scattering and decreases with $1/T$;

$$k = k_i \propto 1/T \tag{2.3}$$

where k_i is the intrinsic conductivity and T is the absolute temperature. However, a weak temperature dependence was observed in the thermal conductivities of the oxides with the presence of high concentration of point defects, which influences the mean free paths of phonons by scattering them;

$$k = k_i - \delta k_p \tag{2.4}$$

where δk_p denotes the decrease in the thermal conductivity due to point defect scattering (Klemens, 1996). Another factor leading to a substantial decrease in the thermal con-

ductivity in the high temperature range by altering the mean free paths of the phonons was shown as grain boundaries in the nanocrystalline ceramics (Soyez *et al.*, 2000). But as the grain boundaries of the material of interest are in the micrometer range, this influence can be disregarded here (Wu *et al.*, 2002a; Lehmann *et al.*, 2003). Therefore, A and B cation substitution and corresponding oxygen vacancies are the considered point defects leading to decrease (δk_p) in the thermal conductivity. The scattering strength of the point defects is given as proportional to the square of the atomic mass difference of A and B cations and oxygen vacancies were reported as more effective in comparison to cation substitution in this regard due to missing anion mass (Wu *et al.*, 2002a).

Based on these, lower thermal conductivity of the pyrochlores compared to the standard YSZ and other doped zirconates were expected as a result of (i) a relatively higher level of cation substitution with respect to the doped zirconia and (ii) a high concentration of the oxygen vacancies present in the crystal structure as well as (iii) a larger atomic mass difference with zirconia of the lanthanides than the Y.

In the temperature ranges of 700-1400 °C, thermal conductivities of dense pyrochlores of La, Nd, Sm, Eu, Gd were reported between 1.1-2.0 W/mK, although there are discrepancies between the studies for the same materials due to differences in the initial porosities and measurement techniques (Suresh *et al.*, 1997, 1998; Vaßen *et al.*, 2000; Maloney, 2001; Wu *et al.*, 2002a; Lehmann *et al.*, 2003).

Wu *et al.* (2002a) studied the influence of order-disorder transition of $Gd_2Zr_2O_7$ pyrochlore-fluorite phases on the thermal conductivity, since disordered-fluorite phase is stable at elevated temperatures which will be discussed later, and found very similar results. Moreover, they investigated the thermal conductivity as a function of temperature and stoichiometry changes in the ZrO_2-$GdO_{1.5}$ system (Wu *et al.*, 2002b). Their results revealed that the thermal conductivity of the solid solution is slightly affected by the composition particularly at elevated temperatures.

Further reductions in the thermal conductivity of the pyrochlores were achieved by doping them with other cations. Lehmann *et al.* (2003) showed that doping $La_2Zr_2O_7$ with 30 % Nd (atomic mass, m_a=144.23), Eu (m_a=151.94) or Gd (m_a=157.25) leads to a systematic reduction in the thermal conductivity with the increase of m_a of the doping element. Accordingly, a maximum reduction from 1.55 to 0.9 W/mK in the thermal conductivity was obtained with 30 % Gd dopant at 800 °C. Bansal and Zhu (2007) also studied the thermal conductivity of the same material and revealed that doping $La_2Zr_2O_7$ with both Gd (15 %) and Yb (15 %) leads to additional reductions with respect to the solely Gd (30 %) doped $La_2Zr_2O_7$. Recently Guo *et al.* (2014) reported the thermal conductivities of Yb_2O_3 (Yb, m_a=173.05) doped $Gd_2Zr_2O_7$ ceramics as in a range of 0.88-1.00 W/mK

at 1400 °C, about 20 % lower than that of $Gd_2Zr_2O_7$ ($\sim$ 1.18 W/mK). It should be noted that the use of high atomic mass elements will increase the weight of these materials but it is dominated by the benefits obtained from the reduction in thermal conductivity.
Although many experimental studies especially on zirconate pyrochlores are already available, measurements are typically limited to 800 °C. If they are not, then a pronounced contribution of radiative heat transfer at higher temperatures complicates the interpretation and understanding of point defects and phonon scattering at these high temperatures. Thereby, molecular dynamic (MD) simulations have been evolved for a better understanding of thermal transport in new TBC materials by adapting and further developing earlier phonon models to this application. Schelling *et al.*, who also studied the effect of yttria concentration on the thermal conductivity of yttria-stabilized zirconia by MD simulations (Schelling and Phillpot, 2001), investigated the effect of the size of A, B cations on the thermal conductivity of pyrochlores at high temperatures (1200 °C) and found a greater dependence on the B than A ionic radius (Schelling *et al.*, 2004).

2.3.2 High Temperature Phase Stability

Another essential benefit of pyrochlores is their high temperature phase stability. Unlike the YSZ, the pyrochlores remain as single phases over the entire service temperature range of TBCs. Figure 2.12 shows the calculated phase diagrams of ZrO_2-$REO_{1.5}$ binary systems in which pyrochlores of interest for TBCs appear with systematically decreasing radii of lanthanide cations (La→Nd→Sm→Gd).
$La_2Zr_2O_7$ is one of the most studied zirconate pyrcohlores as a TBC material. It can be seen from ZrO_2-$LaO_{1.5}$ phase diagram that the P phase forms directly from the liquid (L) in contrast to the zirconate pyrochlores with smaller RE cations. Expansion of the F field is observed with decreasing radii of RE cations which results in the formation of P with an order-disorder transformation from F phase and increasing of the melting temperatures of pyrochlores in the same direction (Table 2.3).

Table 2.3: Melting temperatures of the pyrochlores given by Wang, 2006.

Composition	Melting temperature (K)
$La_2Zr_2O_7$	2556
$Nd_2Zr_2O_7$	2593
$Sm_2Zr_2O_7$	2770
$Gd_2Zr_2O_7$	2843

Comparing the highest stability temperatures of P phases, a decreasing temperature trend is observed with decreasing radii of lanthanide cations. Although, the highest stability

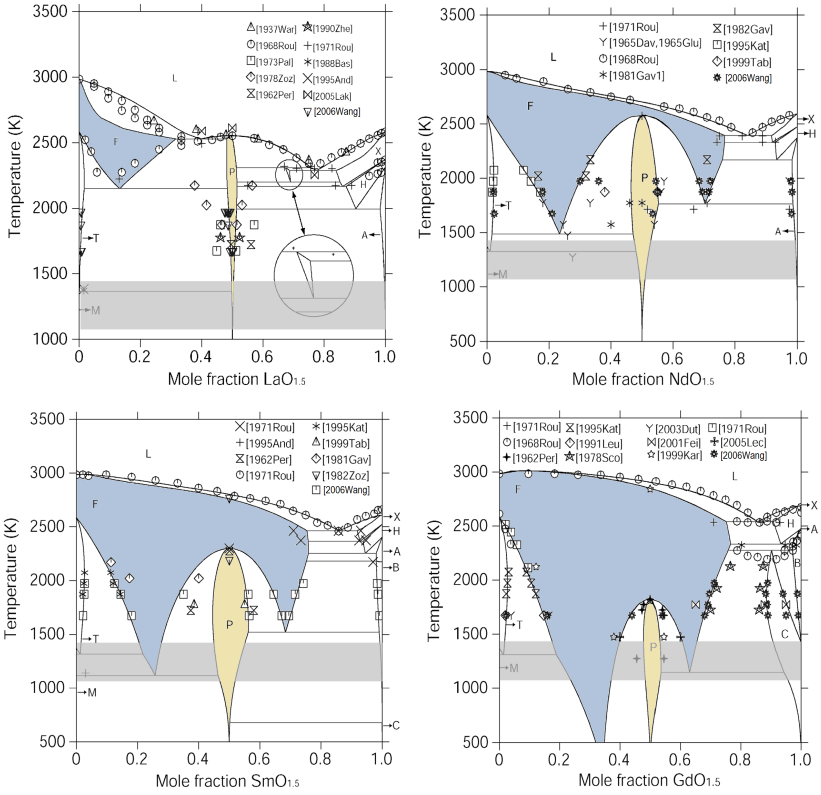

Figure 2.12: Calculated phase diagrams of ZrO_2-$REO_{1.5}$ (RE:La→Nd→Sm→Gd) systems compared with experimental results. Reproduced from (Wang, 2006). The grey shaded regions indicate the approximate maximum exposure temperature of TBCs, the pyrochlore (P) and fluorite (F) phase regions were colored with yellow and blue, respectively.

temperature calculated by Wang, 2006 of $La_2Zr_2O_7$ (2556K) is lower than the pyrochlore of next smaller RE cation (Nd, 2584K). However, Wang, 2006 reported that there are studies predicting the temperature of both transformations of L→P in ZrO_2-$LaO_{1.5}$ and F→P in ZrO_2-$NdO_{1.5}$ systems quite differently, which can give a reason for about 30K difference here. After all, $Gd_2Zr_2O_7$ pyrochlore has the lowest stability temperature (1823K, Wang 2006) with respect to its counterparts, but it is still quite above the max exposure temperature of the TBCs.

It should be noted here that, "different" versions of the experimental phase diagrams of the "same" ZrO_2-$REO_{1.5}$ binary systems are available in the literature. This makes difficult the decision of phase transition temperatures or existence of stable phases in

certain temperature ranges, which might be critical for TBCs eventually. Furthermore, it becomes more critical to extend the compositions of the phase diagrams with different elements for new material synthesis. Calculated phase diagrams using thermodynamic modeling (Yokokawa *et al.*, 2001; Wang, 2006) as well as phase maps obtained by combining atomistic simulations and experimental data (Clave, 2006) provide great insights into these regards. As an example for that, simulated stability regions of pyrochlore, fluorite and δ-phases at low and high temperatures are shown in Figure 2.13. δ-phase

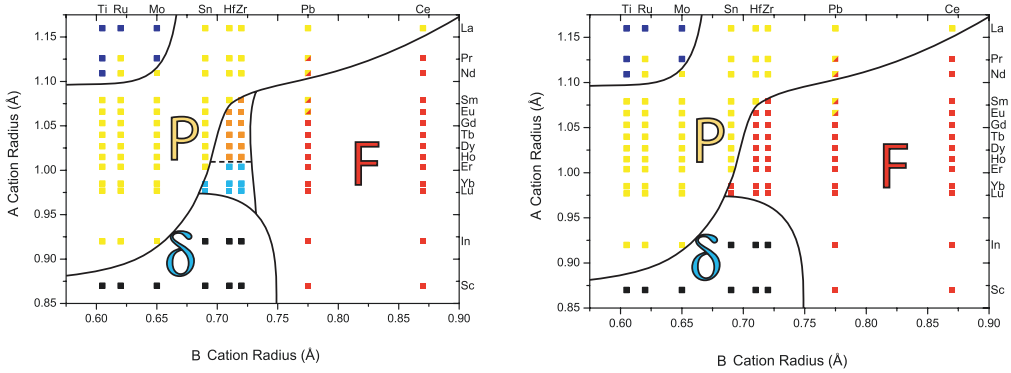

Figure 2.13: Phase maps showing the stability of pyrochlore (P), fluorite (F) and delta (δ) phases at low (room temperature) (a) and high (2000 K) (b) temperatures. Color key for map (a) : dark blue (possibly monoclinic pyrochlore), yellow (pyrochlore forming from melt), orange (pyrochlore formed by order-disorder transformation), black (δ-phase postulated to form from the melt), light blue (δ-phase formed by order-disorder transformation), red (disordered fluorite). Color key for map (b): dark blue (possibly monoclinic pyrochlore), yellow (pyrochlore), black (δ-phase), red (disordered fluorite) (Clave, 2006).

($A_4B_3O_{12}$), which is formed for instance when the oxides of smaller In or Sc ions and zirconia are combined, is another fluorite-related phase and much less is known about these phase unlike the more extensively studied pyrochlore phase. The simulated maps give information for an extensive range of compositions such as which element combinations are stable in pyrochlore phase or which pyrochlore compositions directly formed from liquid or undergo order-disorder transformations.

2.3.3 CTEs

Pyrochlores were well accepted as good candidates of the TBC top coat materials also due to their relatively high CTEs. The CTEs of the dense pyrochlores ($A_2Zr_2O_7$) of

La, Nd, Sm, Eu and Gd were reported between 9.1-11.5×10^{-6} K^{-1} at 1000 °C (Lehmann *et al.*, 2003; Wan *et al.*, 2009; Guo *et al.*, 2014), although there are differences between the measurement results for the same materials likely due to different measurement setups. For instance, CTE of $Gd_2Zr_2O_7$ is measured to be 10.6×10^{-6} K^{-1} by Lehmann *et al.* 2003; Guo *et al.* 2014, while Wan *et al.* 2009 stated it as 11.5×10^{-6} K^{-1}. Nevertheless it is somewhat clear that CTEs of the pyrochlores are close to that of the standard YSZ (11×10^{-6} K^{-1}).

Lehmann *et al.* (2003) studied on two groups of pyrochlores; (i) pyrochlores of La, Nd, Eu, Gd with systematically decreasing ion radius and (ii) $La_2Zr_2O_7$ pyrochlore which 30 % of La substituted with Nd, Eu and Gd ($La_{1.4}$(Nd, Eu, Gd)$_{0.6}Zr_2O_7$). For the first group, their results revealed that $La_2Zr_2O_7$ with the largest La cation in the group has the lowest CTE over the whole studied temperature range (RT-1400 °C). However other than this, no simple dependence of CTE on the cation size was found for the rest of the elements in the same temperature range. In the second group, CTE of partially substituted compounds was reported as slightly different than the $La_2Zr_2O_7$ showing that substitution of 30% La with other trivalent cations does not produce a sufficient distortion in the lattice to lead to a significant change in CTEs.

Another A-site doping investigation was made on $Gd_2Zr_2O_7$ pyrochlore by Guo *et al.* (2014). Yb was selected as dopant element, which has the smallest ionic radii among rare-earth elements and hence reduces the value of rA/rB ratio resulting in the stabilization of defect fluorite structure instead of the pyrochlore. They found the CTEs of Yb_2O_3 doped $Gd_2Zr_2O_7$ defect fluorite composition at 1200 °C in a range of 11.8×10^{-6} K^{-1} to 13×10^{-6} K^{-1}, which are comparable to or even larger than that of YSZ. CTE of doped $Gd_2Zr_2O_7$ was also investigated by Wan *et al.* (2009). They chose smaller Ti^{4+} to partially substitute B-site Zr^{4+}, which leads to increase in the ordering of the pyrochlore structure due to higher rA/rB ratio, and reported the CTE of the $Gd_2(Zr_{0.8}Ti_{0.2})_2O_7$ as 11.8×10^{-6} K^{-1} at 1000 °C.

After all, questions related with the mechanisms which determine the CTE of the rare-earth zirconates arise such as: which distortions in the lattice are most important for the CTE or how does doping in A and B sites affect the CTE. A molecular dynamic study which calculates the CTE of rare-earth zirconates suggested some answers to these questions (Qun-bo *et al.*, 2009). They compared the A-O, Zr-O and O-O bond pairs with molecular dynamic simulations and found that Zr-O bond is the strongest bond in the pyrochlore structure followed by A-O bond. Therefore, it was suggested for obtaining higher CTEs to dope B (Zr^{+4}) site in order to weaken the Zr-O bonding. They showed for the two $Sm_2Zr_2O_7$ pyrochlore structures each doped only at A or B sites that, B-site

doped $Sm_2Zr_2O_7$ have a higher CTE than A-site doped, while undoped $Sm_2Zr_2O_7$ has smallest CTE among them. Furthermore they claimed that due to longer and hence weaker Zr-O bond of the fluorite structure than the pyrochlore, fluorite structure yields higher CTEs.

2.3.4 Sintering Resistance

The ordered pyrochlore structure was introduced as having higher intrinsic sintering resistance than the cubic-fluorite structure of the standard YSZ. In the YSZ, mobile oxygen ion vacancies are produced by substitution of Zr^{+4} ions with lower valent Y^{3+} ions, which is the reason of the YSZ to be a good oxygen-ion conductor and the choice of the electrolyte in solid-oxide fuel cells (SOFC) (Goodenough, 2000). However, as these mobile oxygen vacancies can facilitate the diffusion of the species throughout the matrix, they can also compromise the sintering resistance of the material. On the other hand ordered pyrochlore structures are reported as poor ionic conductors due to their ordered oxygen vacancies, although a large increase in the ionic conductivity is observed on the disordering of the crystal structure (Diaz-Guillen *et al.*, 2008). It is not clear, yet, the diffusion rate of cations and its effect on the sintering resistance on these materials. But ordered pyrochlores were suggested as sinter resistant thermal barrier coatings with patents (Subramanian, 2005; Subramanian and Allen, 2005). Nevertheless, it should be noted here that the pyrochlore to fluorite order-transition temperatures (e.g.lie between 1500-1550 °C for $Gd_2Zr_2O_7$ (Shlyakhtina *et al.*, 2004) might be a limiting factor for the sintering resistance of these materials.

The sintering activity of cold and hot-pressed $La_2Zr_2O_7$was investigated and the results revealed that the $La_2Zr_2O_7$ powder was not fully sintered (∼97 % relative density) at 1400 °C after 3 h under 100 MPa (Vaßen *et al.*, 2000). In another study, relative densities of amorphous, submicron $Gd_2Zr_2O_7$ and $Nd_2Zr_2O_7$ was found as 97 % and 93 %, respectively, after sintering 50 h at 1400 °C (Kong *et al.*, 2013). The sintering resistance differences between the materials were explained by their rA/rB ratios ($Gd_2Zr_2O_7$, 1.46; $Nd_2Zr_2O_7$, 1.54), which determine the thermal activation energy needed for cation and anion ordering in the structures. Due to larger cation radius ratio of $Nd_2Zr_2O_7$, smaller activation energy is required to minimize defects in the structure and thus greater degree of ordering leads to better sintering resistance.

2.3.5 CMAS Resistance, Hot Corrosion and Erosion Behaviors

Recently, superior CMAS resistance of pyrochlores (more specifically $Gd_2Zr_2O_7$) with respect to the standard YSZ was presented, which was a notable finding for the implementation of pyrochlores as top coat materials in TBCs (Freling *et al.*, 2008; Litton *et al.*, 2010). First it was reported for a EB-PVD $Gd_2Zr_2O_7$ TBC that $Gd_2Zr_2O_7$ reacts with the CMAS melt resulting in the crystallization of a highly stable apatite phase incorporating Ca, Gd, and Si at temperatures well above the melting point of the original deposit. This crystalline phase seals off the top of the coating and prevents further CMAS penetration as the reaction and crystallization kinetics are competitive with that for the penetration (Krämer *et al.*, 2008). Later, similar to the EB-PVD $Gd_2Zr_2O_7$ coating, formation of a sealing layer made of $Ca_2Gd_8(SiO_4)_6O_2$ apatite phase was documented for an APS $Gd_2Zr_2O_7$ coating, as well (Figure 2.14) (Drexler *et al.*, 2012a). The CMAS pen-

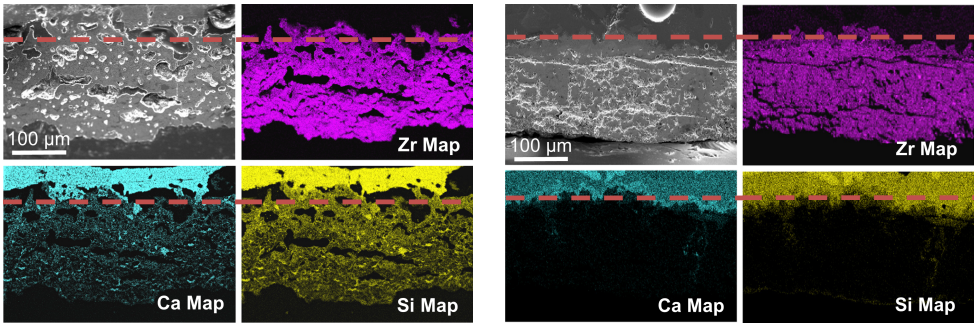

Figure 2.14: Cross-sectional SEM micrograph of APS 7YSZ (a) and $Gd_2Zr_2O_7$ (b) TBCs and corresponding Zr, Ca, and Si elemental maps after interaction with CMAS glass (1200 °C, 24 h). The horizontal dashed line denotes top surface of the original TBC. Reproduced from (Drexler *et al.*, 2012a).

etration depth in the APS $Gd_2Zr_2O_7$ coating was noted as ∼20 µm after 24 h interaction at 1200 °C, while it was ∼200 µm for the APS YSZ coating under same test conditions. Moreover, resistance of APS $Gd_2Zr_2O_7$ against different type of molten silicate deposits (e.g.volcanic ash, coal fly ash) was reported in the same study.

After it was somewhat clear that the $Gd_2Zr_2O_7$ provides a resistance to the penetration of CMAS regardless of its microstructure (APS or EB-PVD) and type of molten silicate deposit, performance of different RE-zirconate compositions were investigated for the same purpose. Drexler *et al.* (2012b) prepared ceramic porous pellets (∼15 % porous) of $RE_2Zr_2O_7$, (RE=Y, Gd, Yb) and YSZ and infiltrated them with the CMAS (1200 °C,

24 h). A summary of their findings in terms of CMAS penetration depth and apatite phases formed as a result of CMAS interaction is given in Table 2.4.

Table 2.4: CMAS mitigation performance of different $RE_2Zr_2O_7$ oxides and their apatite reaction products with CMAS interaction reported by (Drexler *et al.*, 2012b). Note the different apatite phase stoichiometries of Y and Yb than Gd.

Composition	**CMAS penetration depth (µm)**	**Observed crystalline apatite phases in the reaction zone after CMAS interaction**
$Y_2Zr_2O_7$	20 ± 3	Y-apatite, $Ca_4Y_6(SiO_4)_6O$
$Gd_2Zr_2O_7$	60 ± 4	Gd-apatite, $Ca_2Gd_8(SiO_4)_6O_2$
$Yb_2Zr_2O_7$	40 ± 3	Yb-apatite, $Ca_4Yb_6(SiO_4)_6O$
7YSZ	263 ± 3	No apatite phase

From the two pellets containing Y^{3+}, a 13.2-fold decrease in the CMAS penetration depth with increasing Y^{3+} concentration from 7YSZ to $Y_2Zr_2O_7$ was recorded and formation of an apatite phase was observed for the latter. Due to higher Y^{3+}concentration of $Y_2Zr_2O_7$,CMAS melts enable to accumulate the Y^{3+} amount required to crystallize into apatite phase which is not the case for YSZ. Different CMAS mitigation performances of the $RE_2Zr_2O_7$ compositions were argued by different RE^{3+} sizes and the formation of stoichiometrically different apatite phases. Their hypothesis was that, as more RE^{+3} cation incorporation is required to form the Gd-type apatite than the Y(or Yb)-type apatite, the CMAS melt needs to penetrate deeper to accumulate sufficient amount of RE^{+3} in case of $Gd_2Zr_2O_7$. On the other hand, although they form similar type-of apatite phases, because the crystallization tendency of RE-apatites decreases with the decreasing size of RE^{3+}, the Y-apatite crystallize readily relative to the Yb-apatite resulting in the shorter penetration depth. More recently, Poerschke and Levi (2015) also systematically investigated the relations between pellet oxide compositions (hafnates or zirconates (M=Hf, Zr) containing $YbO_{1.5}$, $GdO_{1.5}$, or $LaO_{1.5}$ (RE=Yb, Gb, La)), and constitution of varied reaction products, such as apatites, fluorite (Ca and/or RE stabilized cubic MO_2) and the other secondary products e.g. garnet or cuspidine silicates at different test temperatures (1300 and 1500 °C). Their results, however, revealed that from the two most relevant reaction products to mitigate CMAS penetration, the apatite and fluorite, the composition of former is relatively insensitive to the composition of the coating material conversely what Drexler *et al.* (2012b) offered. However, there is a strong correlation between the RE cation in the coating material and the compposition of fluorite phase. Therefore, they proposed the composition of the fluorite as another criterion indicating the effectiveness of the silicate crystallization reactions. Finally, cor-

relating the composition of the fluorite and apatite phases in terms of RE, M and Ca, their result suggested that the effectiveness of crystallization reactions increases with RE cation size (Yb<Gd<La).

Schulz and Braue (2013) also studied the CMAS infiltration response of different pyrochlore compositions but in the form of EB-PVD TBCs. They compared $Gd_2Zr_2O_7$ and $La_2Zr_2O_7$ and found that the latter reacts faster with the CMAS melt than the former, which also confirms the suggestion of Poerschke and Levi (2015) (Gd<La). An 80 µm global infiltration depth was reported in $Gd_2Zr_2O_7$ TBC after 2 h CMAS exposure at 1260 °C. On the other hand, due to more inhomogeneous columnar microstructure of $La_2Zr_2O_7$, which changes the reaction interfaces as well as reaction kinetics as a result of dissimilar amount of supplied CMAS into these reaction zones, different reaction products and penetration depths were observed (e.g. on top of the columns 10 µm, at the the rims 50 µm).

Hot corrosion and erosion behaviors of pyrochlores have not been investigated as intensive as their CMAS resistance, yet. Hot corrosion behaviors of $La_2Zr_2O_7$ and YSZ coatings were compared exposing them to vanadium- and sulfur-containing compounds at temperatures up to 1000 °C for different periods of time (Marple *et al.*, 2004). As noted above, the YSZ coatings are quite vulnerable to vanadium attacks, but they are relatively stable in the presence of sulfur-containing compounds. However, it was revealed with this study that, in contrast to the YSZ, the reaction of $La_2Zr_2O_7$ with V_2O_5 does not result in a degradation of the coating, while the reactions with sulfur-containing compounds lead to the rapid degradation under the same test conditions. The reaction products of $Gd_2Zr_2O_7$ and V_2O_5, which are ZrV_2O_7 and $GdVO_4$ at 700 °C and $GdVO_4$ and m-ZrO_2 at 750-850 °C, are also shown in the literature (Liu *et al.*, 2010; Habibi *et al.*, 2012). Habibi *et al.* (2012) reported a superior hot corrosion resistance of $Gd_2Zr_2O_7$ TBC under Na_2SO_4 + V_2O_5 attack at a temperature of 1050 °C than that of YSZ coatings. Although the different response of materials can be solely related to difference of the chemical compositions, attack mechanisms are not fully understood. Ramachandran *et al.* (2013) investigated the erosion durability of ASP YSZ and $La_2Zr_2O_7$ TBCs with different porosities (min 4-max 24%) with varied velocity, angle of impact and flux of the air suspended erodent corundum particles (50 µm). They reported a general better erosion resistance with lower porosities. Furthermore, they claimed that the $La_2Zr_2O_7$ TBC yielded a superior erosion resistance due to better mechanical properties such as a higher microhardness (H=11.61 GPa), a lower elastic modulus (E=175 GPa) and a higher hardness ratio (H_p/H_t=2.00, p: particle, t:target) than the YSZ coating

(H=11.27 GPa, E=220 GPa; H_p/H_t=2.07), although they noted the fracture toughness of the $La_2Zr_2O_7$ and YSZ coatings as 4 MPa.$m^{1/2}$ and 1.8 MPa.$m^{1/2}$, respectively.

2.3.6 Implementation Related Issues and Considered Solutions

After mentioning a number of properties of pyrochlores which makes them favorable as TBC top coat materials, the issues related with their implementations and suggested solutions for these issues in the literature will be discussed here.

Thermochemical Compatibility with TGO

One of the essential requirements for the ceramic top coat material is its thermochemical compatibility with underlying TGO ($AlO_{1.5}$) layer. As indicated before, the mutual solubility of YSZ and Al_2O_3 is very limited and they do not have interphases, however higher concentration of yttria added zirconia system tends to form an interphase by diffusional interaction with Al_2O_3 (Fabrichnaya and Aldinger, 2004). Figure 2.15 compares the critical (X^*) concentrations of Y_2O_3 (X^*∼23 %), Gd_2O_3 (X^*∼34 %) and La_2O_3 (X^*∼5 %) added zirconate systems that above these dopant concentrations formation of different interphases with Al_2O_3; garnet, perovskite and β alumina, respectively is induced at 1200 °C (Levi, 2004). Based on the cation sizes, general trends show that Y and smaller lanthanides tend to form the garnets, whereas larger (e.g. La, Nd) lanthanides with very small concentrations and intermediate lanthanides with higher concentrations (e.g. Gd) induce formation of the β alumina and the perovskite interphases, respectively. Considering that the stabilization of the pyrochlore phases requires higher Gd_2O_3 or La_2O_3 concentrations than the given compatibility limits (X^*concentrations), it can be concluded that the pyrochlores in general are prone to degrade with interphase formation by diffusional interaction with Al_2O_3.

Leckie *et al.* (2005) studied the interphase formation between the pre-oxidized sapphire substrates and EB-PVD $Gd_2Zr_2O_7$ coatings. They reported that this zirconia TBC with ∼33 mol % Gd_2O_3 tends to react with alumina to form a porous $GdAlO_3$ perovskite interphase as shown in Figure 2.16. Although, the evolution mechanism of the interfacial pores is not fully understood, the following reaction between $Gd_2Zr_2O_7$ and alumina;

$$Gd_2Zr_2O_7 + Al_2O_3 \rightarrow 2GdAlO_3 + 2ZrO_2 \tag{2.5}$$

is reported as accompanied by negative volume change of ∼9 %, which can contribute to explanation. Eventually, this implies that the evolved porous $GdAlO_3$ interphase not

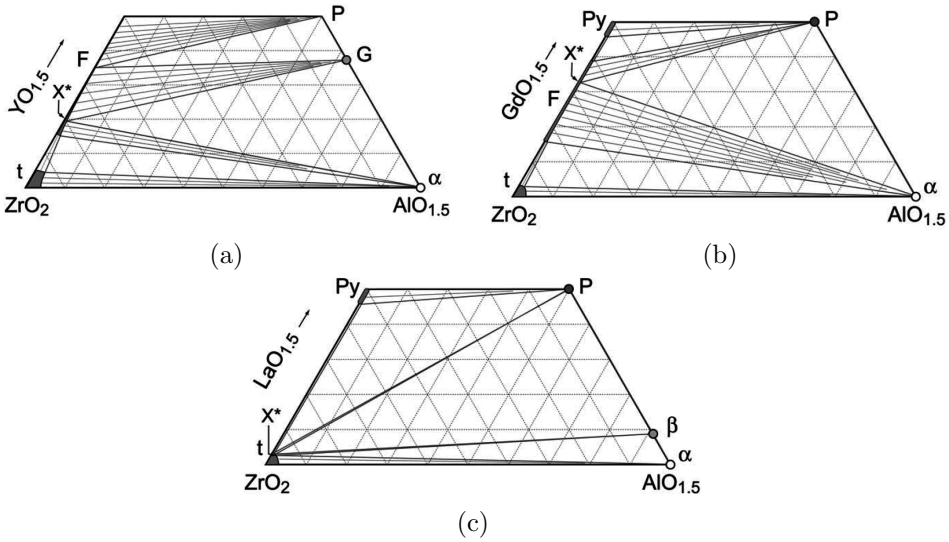

Figure 2.15: Phase diagrams illustrating the interactions of different ZrO_2-$REO_{1.5}$ materials with TGO ($AlO_{1.5}$) layers. When X^* concentration is exceeded the formation of garnet (G), perovskite (P) and β alumina interphases are expected for (a), (b) and (c), respectively at ∼1200 °C (Levi, 2004). t, F and Py denotes tetragonal zirconate, cubic zirconate (fluorite) and pyrochlore.

only weakens the protective function of the alumina TGO but also compromises integrity of the TBC system.

Toughness

Fracture toughness of TBCs has gained significant interest due to its reported influence on the failure mechanisms associated with the TGO growth and CTE mismatch under cycling conditions or material loss due to erosion and FOD that limit the TBC durability (Rabiei and Evans, 2000; Evans *et al.*, 2001; Chen *et al.*, 2003). As a matter of fact, the fracture toughness is a crucial intrinsic factor leading to the 7-8 wt.% yttria-stabilized zirconia with its non-transformable tetragonal (t') phase remains the material of choice for decades. Although the lower thermal conductivity RE zirconates with a number of other favorable properties were discovered, their typically cubic (fluorite, pyrochlore or δ-phase) structure exhibit lower toughness than tetragonal zirconia (Vaßen *et al.*, 2000; Evans *et al.*, 2008; Bast and Schumann, 2009).

Greater toughness of tetragonal zirconia particularly at elevated temperatures has been attributed to a ferroelastic domain switching mechanism (Michel *et al.*, 1984; Virkar and

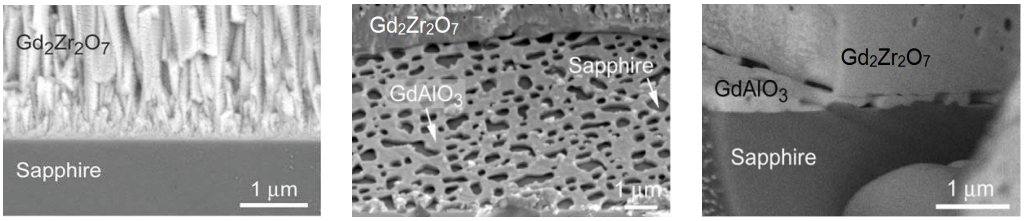

(a) (b) (c)

Figure 2.16: SEM images of sapphire/$Gd_2Zr_2O_7$ interfaces; (a) cross-section of as-deposited interface, (b) porous reaction layer on the sapphire after partial spallation of the coating, (c) FIB (Focused-Ion Beam) cut image showing the reaction zone (Leckie *et al.*, 2005).

Matsumoto, 1986). It was shown that the cubic zirconia structure lacks the benefit of this toughening mechanism. Michel *et al.* (1984) studied the fracture toughness of the tetragonal and cubic single crystals of zirconia doped with Y_2O_3, Yb_2O_3 and Gd_2O_3 and reported the toughness of the tetragonal crystals three times higher than the cubic crystals. In another work, the toughness of the tetragonal zirconia (3-YSZ) was measured to be 300 J/m^2 (using the energy release rate), while the cubic zirconia (20-YSZ) yielded a toughness of 6 J/m^2 (Evans *et al.*, 2008). Leckie (2006) reported the fracture toughness of YSZ and $Gd_2Zr_2O_7$ as ∼45 and ∼10 J/m^2 and showed that TiO_2 addition into ZrO_2-$GdO_{1.5}$ system can enhance the toughness of the pyrochlore by manipulating the tetragonality of the structure. More recently Dwivedi *et al.* (2014) measured the fracture toughness on YSZ and $Gd_2Zr_2O_7$ free-standing APS coatings in as-sprayed and thermally aged conditions. Their results revealed that comparing the YSZ and $Gd_2Zr_2O_7$ coatings sprayed with the same plasma energies (e.g. 24 kW), the former yielded about two-times larger fractures toughness values than the latter. On the other hand, they reported a general toughness enhancement for the aged coatings due to reduction of the overall porosity and microcracks as well as improved interlamellar bonding, but a more pronounced toughness increase for the YSZ coatings which might be attributed to lower sintering rate of the $Gd_2Zr_2O_7$ coatings.

Double-Layer TBCs

Pyrochlore materials give the prospect for elevating the TBCs to higher operation temperatures along with a number of advantageous properties that can improve the TBC durability. However, introducing the pyrochlore as single layer top coats to the TBCs was not successful and early TBC studies of different pyrochlores ($La_2Zr_2O_7$, $Gd_2Zr_2O_7$,

$Sm_2Zr_2O_7$) suggested the use of YSZ as a protective interlayer or for better adherence (Maloney, 2000, 2001; Subramanian, 2002; Vaßen *et al.*, 2004). Another concern was the lower CTE of the pyrochlores which might induce higher thermal stresses in the TBC system and contribute to an early failure. Today it is clearer that the single-layer pyrochlore TBCs do not perform well mainly due to mentioned issues of (i) the formation of deleterious interphases as a result of diffusional interaction with TGO and (ii) low toughness. For that reason, YSZ is suggested as an interlayer between pyrochlore and TGO to work as a diffusion barrier as well as to provide high toughness for hindering the propagation of cracks in the vicinity of the TGO (Figure 2.17).

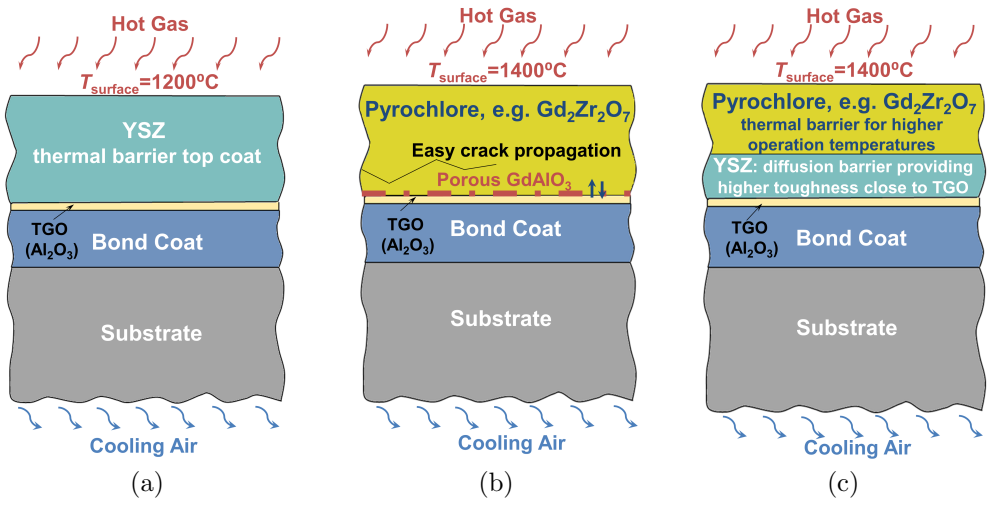

Figure 2.17: Introducing pyrochlore top coats to the TBC system for higher operation temperatures; schematic illustration of a standard TBC with YSZ top coat (a) single-layer TBC with pyrochlore top coat (b) and a double-layer TBC with pyrochlore and YSZ layers (c).

In the past decade, it was shown that the concept is well suited for TBC systems produced by both APS and EB-PVD techniques Vaßen *et al.* (2004); Saruhan *et al.* (2004); Cao *et al.* (2006); Xu *et al.* (2008); Zhao *et al.* (2011); Moskal *et al.* (2012); Liu *et al.* (2014). Vaßen *et al.* (2004) showed that both plasma-sprayed $La_2Zr_2O_7$ and $Gd_2Zr_2O_7$ coatings displayed superior lifetime performance in double-layer TBCs with a combination of YSZ underlayer and provide at least a 100 K higher temperature capability. Later Xu *et al.* (2009) investigated the thermal cycling performance of $La_2Zr_2O_7$/YSZ double-layer TBCs deposited by EB-PVD and found that they perform better than YSZ and single-layer lanthanum zirconate coatings. Contrary to positive findings in the literature

concerning the performance of the double-layers, Munawar *et al.* (2014) recently stated that double-layer GZO TBCs with a YSZ interlayer deposited by EB-PVD do not improve the lifetime under furnace cycling test conditions. On the other hand, they reported that the single-layer GZO coatings, despite the observed Al diffusion from the TGO into the TBC, survived longer than conventional YSZ. The difference in the performance of double layers specified here and in the literature can be attributed to the different test conditions such as temperature (e.g. isothermal conditions or temperature gradient) which directly affect the induced stresses in the TBC system, or bond coat compositions which alter the chemistry of the bond coat-top coat interface.

Processability

For more than a decade it has been known that difference in the vapor pressures of rare-earth oxides (RE_2O_3) and zirconia (ZrO_2) complicates processing of $RE_2Zr_2O_7$ both with APS and EB-PVD processes. Because the rare-earth oxides with higher vapor pressure than zirconia are prone to evaporate at high process temperatures resulting in non-stoichiometric coatings. There is a paucity of information on the thermodynamic properties of these solid solutions, but Jacobson (1989) reported a compilation on vapor pressures of some RE_2O_3-ZrO_2 systems and Figure 2.18 shows a graph plotted based on the data of this report. The vapor pressures of some of the rare-earth oxides and zirconia are plotted as a function of inverse temperature in the graph. The accuracy of the replotted data is not sufficient to make quantitative discussion on the vapor pressures, however general trends show that the differences between the vapor pressures of zirconia and rare-earth oxides increase with the decreasing atomic mass of the rare-earth elements (Gd (157.25)→Sm (150.36)→La (138.90)) or melting temperatures (T_m) of the related pyrochlores ($Gd_2Zr_2O_7$:2843 K, $Sm_2Zr_2O_7$: 2770 K, $La_2Zr_2O_7$:2556 K). Obviously, the intermolecular bonds get stronger when the atomic mass increases so that it is more difficult to break those bonds to escape as gaseous phase. In the same report, confirming vapor pressures of the Gd_2O_3, Sm_2O_3 and La_2O_3 relative to Lu_2O_3 at 2500 K are given as 15, 40 and 130, respectively. Accordingly, it can be anticipated that with respect to the $Sm_2Zr_2O_7$ and $Gd_2Zr_2O_7$, the processing of $La_2Zr_2O_7$ will be more problematic due to relatively higher vapor pressure differences of La_2O_3 and ZrO_2 at a given temperature. Indeed, according to earlier reports on the processing of $La_2Zr_2O_7$, it was observed that different evaporation rates of La_2O_3 and ZrO_2 resulted in unfavourable composition variations both in plasma-sprayed and EB-PVD deposited coatings (Cao *et al.*, 2001; Saruhan *et al.*, 2004). Locally low and fluctuating La_2O_3 concentrations were found in the $La_2Zr_2O_7$ coatings deposited by APS and EB-PVD, respectively. Relatively minor

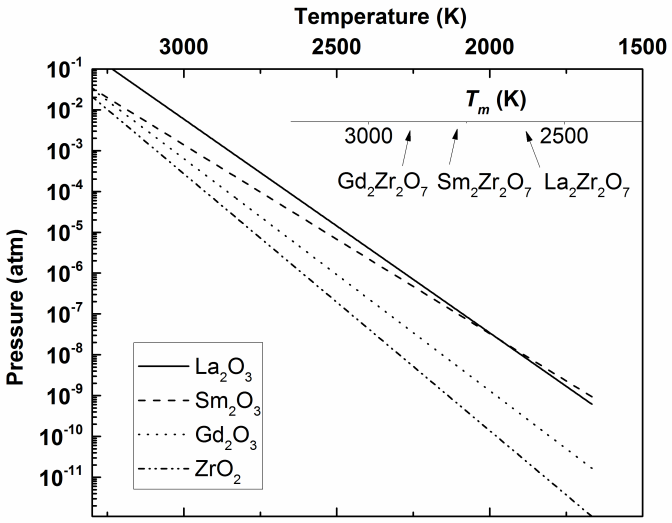

Figure 2.18: Reported vapor pressure-temperature relations for zirconia and rare-earth oxide species of interest for TBCs. Replotted from Jacobson (1989).

compositional Sm_2O_3 and Gd_2O_3 changes were reported in EB-PVD $Sm_2Zr_2O_7$ and $Gd_2Zr_2O_7$ coatings in later studies (Zhao *et al.*, 2009; Munawar *et al.*, 2014).

Cao *et al.* (2001) addressed the fact that the thermal cycling performance of $La_2Zr_2O_7$ coatings is affected by the fast La_2O_3 loss during the plasma spraying process. This can be prevented to some extent by increasing the amount of La_2O_3 in the feedstock. However, it is not possible to control the process entirely by doing so, due to the fact that the evaporation rate of the sprayed powder is also influenced by the particle size: vaporization will occur sooner for a small particle than a larger one and will only take place at the particle surface. On the other hand, La_2O_3 content strongly influences the melting and boiling temperature of lanthanum zirconate according to La_2O_3-ZrO_2 binary phase diagram. Hence, a more sophisticated material related solution is needed in this regard. Similarly, Mauer *et al.* (2012) made an investigation of $La_2Zr_2O_7$ and $Gd_2Zr_2O_7$ processing with the APS. The results clearly indicated that the lanthana is excessively evaporated at the particle surfaces during flight above a specific power level (Figure 2.19). As a consequence of this, significant amounts of metastable cubic zirconia phase is developed which will transform and then undergo specific volume changes during thermal cycling. It was stated that the $La_2Zr_2O_7$ coating with lanthanum depleted as-sprayed microstructure failed after only 14 cycles at 1400 °C/1040 °C surface/bond coat temperatures in burner rig test. Thus, the implication was requirement of a careful APS

process optimization for pyrochlore materials. Additionally, the study showed that the gadolinia loss in the $Gd_2Zr_2O_7$ coatings was less pronounced than the lanthana loss in $La_2Zr_2O_7$ coatings sprayed with identical spray conditions, presumably due to the lower vapor pressure of gadolinia. In the EB-PVD manufacturing route of $La_2Zr_2O_7$ coating, it was suggested that the addition of an oxide with low vapor pressure such as Y_2O_3 to the $La_2Zr_2O_7$ would assist in stabilizing the pressure conditions of deposition chamber and improve the chemical homogeneity of the coating (Saruhan *et al.*, 2004).

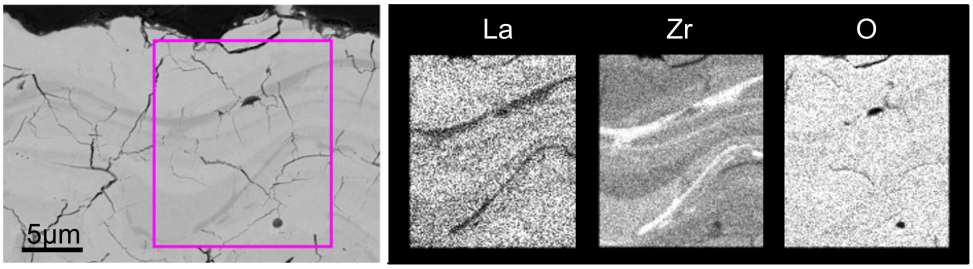

Figure 2.19: Back-scattered SEM image and EDS elemental mapping of La, Zr and O in the as-sprayed $La_2Zr_2O_7$ coating. Reproduced from (Mauer *et al.*, 2012).

2.3.7 Summary of Merits and Issues

The main advantages and drawbacks of the pyrochlore crystal structure over the cubic fluorite structure were presented above. Additionally, some of the properties of the pyrochlores were discussed in relation to cation size and atomic mass of dopant rare-earth (RE) elements. Based on the available literature work, the results and trends indicate:

i. a lower thermal conductivity of pyrochlore zirconates than YSZ as a result of higher concentration of the oxygen vacancies present in the crystal structure and further reductions with larger atomic mass difference of the RE elements with zirconia.

ii. a higher temperature phase stability of pyrochlore zirconates compared to the YSZ, although the melting temperature of YSZ is higher, and increase in pyrochlore phase stability with increasing RE cation size. Although, the pyrochlore phase is stable up to 1823 K even in Gd_2O_3-ZrO_2 binary system which has one of the smallest RE cation size. Furthermore, it is reported that the pyrochlore-fluorite transformation does not compromise the integrity of the system.

iii. CTEs of pyrochlore zirconates close to that of the YSZ, even higher CTEs in specific cases by reducing rA/rB ratio, but no obvious dependence of the CTE on the RE features.

iv. a higher sintering resistance of ordered pyrochlores attributed to ordered oxygen vacancies compared to the YSZ.

v. a superior CMAS resistance of pyrochlore zirconate with respect to the YSZ as a result of formation of crystalline apatite phase which seals off the top of the coating and prevents further CMAS penetration. In one recent study it is stated that the effectiveness of crystallization reactions increases with increasing RE cation size.

vi. a better resistance of zirconate pyrochlores to V_2O_5 corrosion attack but worse against sulfur containing media with comparison to the YSZ and a worse resistance of pyrochlores against erosion is expected due to lower toughness.

vii. formation of deleterious interphases as a result of diffusional interaction of pyrochlores with TGO, while the standard 7YSZ is thermocompatible with the TGO.

viii. a lower toughness of pyrochlores than the YSZ attributed to their cubic structure with no toughening mechanism likewise the ferroelastic domain switching in tetragonal zirconia.

ix. a double layer TBC top coat structure consisted of a pyrochlore layer on top of a YSZ layer seems to be a good solution for low toughness and chemical TGO interaction problems of the pyrochlores.

x. the difference of evaporation rates of RE oxides, particularly oxides of large RE cations, and zirconia at high temperatures result in unfavorable composition variations both in plasma-sprayed and EB-PVD deposited coatings.

3 | Experimental Methods and Materials

3.1 Feedstock

The gadolinium zirconate ($Gd_2Zr_2O_7$, hereafter referred to as GZO) top coats were produced from two different powder batches in this study. The hollow-spherical morphology of the spray dried GZO powder, which is favorable for a good flowability during plasma spraying, is shown in Figure 3.1. The GZO powder names and manufacturer information are given in Table 3.1 along with the information of other feedstock used to spray YSZ top coats and NiCoCrAlY bond coats.

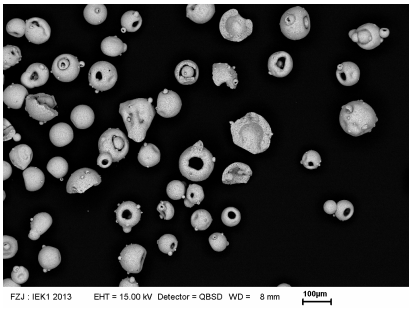

Figure 3.1: SEM image showing the morphology of spray dried GZO 357 H feedstock.

Particle size of the each feedstock was measured with laser diffraction (LA-950-V2, Horiba Ltd., Japan). In this analysis, when particles of different sizes pass a laser beam, they cause the laser light to be scattered at angles and intensities that are inversely and directly proportional to the particle size, respectively. The resulting diffraction patterns are then translated into a given particle size using an algorithm designed based on either Fraunhofer or Mie scattering theory and the former was used in this study (de Boer *et al.*, 1987). The obtained particle size data of the feedstock in terms of d_{10}, d_{50} and d_{90}, which indicate the maximum particle diameters below 10, 50 and 90 % of the cumulative sample volume distribution, is also shown in Table 3.1.

Table 3.1: Information of ceramic and metallic feedstock used in this study.

				Particle Size (µm)		
Material	**Name**	**Manufacturer**	**Internal Code**	d_{10}	d_{50}	d_{90}
GZO	Amperit 835.090	H.C. Starck	GZO 357 H	60	83	117
GZO	Amperit 835.956	H.C. Starck	GZO 365 H	64	86	116
YSZ	204NS	Oerlikon Metco	YSZ 335 M	28	54	85
NiCoCrAlY	Amdry 386	Oerlikon Metco	BCM 319 M	15	24	36

Chemical composition of the GZO feedstock is another important feature, as gadolinia evaporation will be investigated during plasma spray process. Elemental composition of the GZO feedstock was thus determined by ICP-OES (Inductively Coupled Plasma-Optical Emission Spectroscopy, TJA-Iris-Intrepid, Thermo Scientific GmbH, Germany). In the ICP-OES method, the sample in liquid form is converted to an aerosol by a device called nebulizer and then fed to the plasma charge, where the atomization and ionization of the sample takes place. The excited atoms and ions create a unique emission spectrum specific to element and the intensity of each emission spectrum depends on the concentration of the element in the sample (Olesik, 1991). For elemental analysis of the feedstock, 10 mg specimen was dissolved in 2 g of $(NH_4)_2SO_4$ and 4 ml H_2SO_4 and completed to 100 ml. The Gd and Zr element compositions are given in Table 3.2 indicating the average and standard deviation of the three measurements.

Table 3.2: Gd and Zr concentration of the GZO feedstock.

Feedstock	**Gd wt.%**	**Zr wt.%**
Theoretical Value	51.6	29.9
GZO 357 H	52.3 ± 1.2	29.7 ± 0.7
GZO 365 H	52.1 ± 1.1	28.6 ± 0.9

3.2 Thermal Spraying

3.2.1 Deposition of Top Coats, Bond Coats and Single Splats

The YSZ and GZO ceramic top coats, which were prepared either in the form of free-standing coatings or double-layer TBCs, or single splats used in this study were sprayed by the APS method. The free-standing coatings and the single splats were used to

characterize microstructural and compositional properties, while the double layer systems were thermally cycled for the lifetime assessment.
Spraying experiments were performed in a Multicoat facility (Oerlikon Metco, Wohlen, Switzerland) with a triple-cathode, cascaded TriplexPro-210^{TM} spray gun mounted on a six-axis robot. The optimized APS parameters for the coatings and single splats such as powder feed rate or robot velocity and some others are given in Table 3.3. APS spray current and stand-off distance optimizations to meet desired porosity and stoichiometric composition in GZO coatings are one of the main objectives of this study and they will be discussed in the results sections of related chapters.

Table 3.3: Specific APS parameters used for the spraying.

	Plasma gas composition (slpm)*	**Carrier gas (slpm)**	**Powder feed rate (%)**	**Robot velocity (mm/s)**
YSZ top coat	50 Ar+4 He	1.6 Ar	20	500
GZO top coat	46 Ar+4 He	2 Ar	10	500
GZO single splats	46 Ar+4 He	2 Ar	2	2500

*standard liter per minute

The NiCoCrAlY (Oerlikon Metco, Amdry 386) bond coats were sprayed by VPS in a Oerlikon Metco facility using an F4 gun. The plasma jet was generated using a mixture of argon and hydrogen at a flow rate of 50 slpm and 9 slpm, respectively in a chamber pressure of 50 mbar Ar. Bond coats were sprayed with a spray current of 640 A and a stand-off distance of 275 mm. Prior to top coat deposition bond-coated specimens were annealed under vacuum at 1120 °C/2 h and 840 °C/24 h.
Single splats were deposited on mirror polished stainless steel substrates, while free-standing coatings were obtained by following three different ways; (i) the coating was sprayed on a graphite substrate and subsequently detached by grinding the graphite, (ii) the coating was sprayed on a steel substrate and afterward the steel substrate was dissolved in HCI acid or (iii) the coating was sprayed on a salt (NaCI) coated stainless steel substrate and then detached by dissolving the NaCI in water.

3.2.2 Particle Diagnostics

In-flight particle temperatures of the sprayed GZO feedstock were measured at varied spray currents and stand-off distances by a DPV-2000 (Tecnar Automation Ltd., St. Bruno, QC, Canada) particle diagnostic system. In the system, the temperature is acquired by two-color pyrometry, which involves filtering of the thermal radiance emitted

by a particle at two wavelength bands (λ_1 =787 ± 25 nm and λ_2 =995 ± 25 nm) (Fincke *et al.*, 2001).

According to Planck´s law of radiation, the intensity of radiation emitted by unit surface area of a black-body can be expressed as a function of wavelength (λ) and an absolute temperature (T)

$$E(\lambda) = \frac{2hc^2}{\lambda^5} \cdot \frac{1}{e^{\frac{hc}{\lambda k_B T}} - 1} \tag{3.1}$$

where h and k_B are the Planck and Boltzmann constants, respectively and c is the speed of light.

Accordingly, the thermal radiance ratio emitted by a particle at two different wavelengths can be written as

$$\frac{E(\lambda_1)}{E(\lambda_2)} = \left(\frac{\lambda_2}{\lambda_1}\right)^5 \cdot \frac{\varepsilon(\lambda_1).e^{\frac{hc}{\lambda_2 k_B T}} - 1}{\varepsilon(\lambda_2).e^{\frac{hc}{\lambda_1 k_B T}} - 1} \tag{3.2}$$

where ε is the emissivity and defined as the ratio of energy being emitted by a real body to that emitted by a black body. Emissivity values are material-specific and vary between zero and one, and generally depend on the wavelength and temperature. However, as the emissivities are unknown particularly for the molten ceramic oxide materials, it is assumed that the emissivity is not wavelength dependent and thus $\varepsilon(\lambda_1)/\varepsilon(\lambda_2) = 1$ is used. It was shown that this assumption introduces systematic errors to temperature measurements and therefore a calibration is required particularly at temperatures above 3000 K (Mauer *et al.*, 2008).

3.3 Characterization

3.3.1 Mercury Intrusion Porosimetry (MIP)

The mercury intrusion porosimetry is commonly used to measure pore size and pore size distribution as it can be applied to evaluate pore sizes from 1 mm to nanometers in diameter. The method uses the non-wetting property of mercury combined with its high surface tension (Mikijelj *et al.*, 1991; Ishizaki *et al.*, 1998). Because the mercury does not spontaneously penetrate pores by capillary action, it must be forced into the pores by the application of external pressure. Assuming the pores are cylindrical, the required pressure (P) to force mercury to penetrate into pores is inversely proportional to the

radius of the pores (r), while the pressure is balanced by the surface tension (γ) of the mercury leading to

$$P = \frac{-2\gamma cos\theta}{r} \tag{3.3}$$

known as Washburn equation (Washburn, 1921). The θ denotes the contact angle between the mercury and the material (>90°). Accordingly, the pore radius is calculated by measuring the pressure, as the θ and γ are constants for the material and mercury. Simultaneously, the volume of the pores in the corresponding pore size class is determined by measuring the volume of mercury that penetrates into the sample with each pressure change. In this regard, presence of the pores that are closed and cannot be accessed by the mercury in the material leads to an underestimation of the total volume of the porosity. Finally, a porosity distribution curve is obtained by plotting the cumulative volume of the pores as a function of the pore radius ($\phi(r)$). Pore size distribution of the coating samples was obtained using one low (0.01 to 400 kPa) and one high pressure (up to 400 MPa) porosimeter in this study (Pascal 140 and Pascal 440, Thermo Scientific GmbH, Germany). To obtain the logarithmic pore size distribution function ($\Delta\phi/\Delta(log_{10}(r))$) for a different presentation displaying the microstructural porosity features, the data was smoothed with a Savitzky-Golay filter of the third order with a window width of $\Delta log_{10}(r/\mu m)$=0.6.

3.3.2 X-ray Diffraction (XRD)

The X-ray diffraction is an instrumental technique that is usually used to study crystalline materials whose three-dimensional structure is defined by regular, repeating planes of atoms that form a crystal lattice. X-rays are electromagnetic radiation with wavelengths between about 0.02 Å and 100 Å and as these wavelengths are similar to the size of atoms, X-ray and atom interferences provide useful information to determine crystal structure (Warren, 1969).

The interference, when a beam of monochromatic X-rays (λ) entering a crystal with atomic plane spacing *d,* and one of these planes of atoms oriented at an angle of θ to the incoming beam of X-rays is described by

$$n\lambda = 2dsin\theta, n = 1, 2, 3.. \tag{3.4}$$

which is known as Bragg´s law for X-ray diffraction (Bragg and Bragg, 1913). n is an integer for constructive interference.

In the X-ray diffraction technique, thus, the characteristic d-spacing of the crystal is calculated with a known X-ray wavelength and a measured diffraction angle. A diffraction pattern is obtained by measuring the intensity of diffracted waves as a function of the diffraction angle. The XRD data allows (i) the identification of the crystalline phases, (ii) the quantitative analysis of mixed phases, (iii) the evaluation of structural variations under different conditions by calculation of the lattice parameter and (iv) the analysis of crystallite size and strain using the height, width and positions of the peaks in the diffraction pattern.

While the accuracy of the analysis is strictly dependent on these peak characteristics and it was particularly low for the powder diffraction as a result of random orientation of the crystallites and overlapping peaks, a method was introduced to refine the measured peak profile. The method is called Rietveld refinement and it uses a least squares approach to refine a theoretical line profile until it matches the measured XRD profile (Rietveld, 1967). The Rietveld method which uses a numbers of profile parameters to define half-widths or positions of the peaks and structural parameters related to unit cell has been successfully used. Today it is routinely used via softwares that work with it, not only for the refinement of the powder diffraction patterns but also for quantitative phase analysis, lattice parameter calculations etc. Later on different algorithms were developed (Pawley, 1981; Le Bail *et al.*, 1988), which do not take into account the peak intensities but peak positions allowing the refinement of cell parameters very precisely (Toraya, 1989).

In this study, phase analysis of the coatings and the feedstock was carried out by the XRD (Bruker AXS GmbH, Karlsruhe, Germany) using Cu Kα radiation. The operating voltage and current were 40 kV and 40 mA, respectively, with a step size of 0.02° 2ϑ and a step time of 2 s or 0.5 s. The shorter step time were used for the measurements to investigate structural variations due to gadolinia evaporation by means of lattice parameter. The lattice parameters were determined using Pawley´s method for the refinement with TOPAS software (Bruker Corporation, Germany).

3.3.3 Time of Flight-Secondary Ion Mass Spectroscopy (TOF-SIMS)

The secondary ion mass spectroscopy was chosen as a method for the composition analysis of the single splats through the thickness of them. Because gradients might be visible via this method, if the gadolinia evaporation occurs during plasma spraying from the particle surfaces.

SIMS is used in surface science to analyze the composition of solid surfaces and thin films by sputtering the surface of the specimen with a focused primary ion beam and subsequently collecting the emitted secondary ions. The resulting secondary ions are accelerated into a mass spectrometer, where they are mass analyzed by measuring their time-of-flight from the sample surface to the detector (Williams, 1985). The time of flight (t) of the ions over a fixed distance of flight (L) is given by

$$t = L(\frac{m}{2zV_{ac}})^{1/2} \tag{3.5}$$

where m/z is mass-to-charge ratio of the ions and V_{ac} is the accelerating voltage (Benninghoven, 1994).

There are three different modes of analysis in TOF-SIMS; (i) mass spectra are acquired to determine the elemental and molecular species on a surface, (ii) images are acquired to visualize the distribution of individual species on the surface, and (iii) depth profiles are used to determine the distribution of different chemical species as a function of depth from the surface. Accordingly, the depth of the analyzed surface can be changed from 1-2 outermost atomic layer of the sample to the micrometer scales. The depth profile of the GZO single splats were analyzed through their thickness ($\sim$ 2µm) in this study by sputtering the specimen with Cs^+ ions with an energy of 2 keV (TOF-SIMS IV, ION-TOF GmbH, Germany).

3.3.4 Thermomechanical Analysis (TMA)

Materials undergo changes of their thermomechanical properties during heating or cooling. For instance sintering, softening or phase changes can occur in addition to thermal expansion. Thermomechanical analysis is the method to determine these properties as a function of time and temperature. Depending on the selected measuring mode either the expansivity (dilatometry) or elastic behavior (e.g. three-point bending test) of the materials can be investigated.

The thermal expansion, elastic and viscoelastic properties of the free-standing coatings were investigated in this study by means of dilatometry and three-point bending test in a TMA facility (Setsys TMA-18, Setaram Inc., Caluire, France) and details of measurements will be given below.

Dilatometry

The CTE of the free-standing coatings were determined from expansion during heating from ambient to 1400 °C with a 1 K/min heating rate. A schematic of the vertical measurement apparatus located in a box furnace, where the sample is placed under a push-rod in a supporting tube is shown in Figure 3.2a. The height change of the specimen (h) is recorded by a linear displacement transducer in the cold-top region of the push-rod and the push-rod and supporting tube are made from alumina. Interlocking two-pieces sample geometry which enables coating to stand is also shown in Figure 3.2b, where the thickness, height and width of the coating pieces are ∼400 µm, 13 mm and 8 mm, respectively.

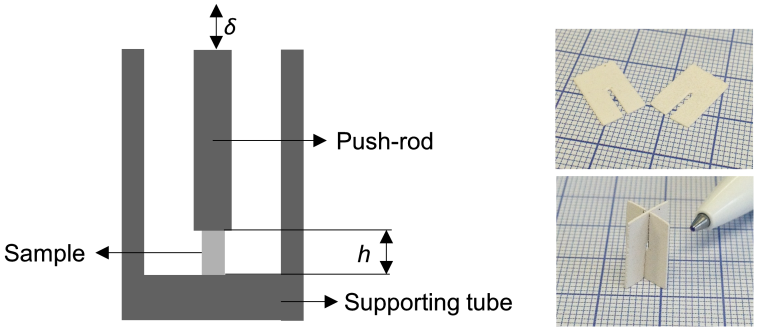

Figure 3.2: Schematic of the vertical measurement apparatus (a) and standing sample geometry used for the dilatometric measurements (b).

As the recorded displacement (δ) by the tranducer is a superposition of the thermal expansion of the sample and the measuring apparatus (push-rod and supporting tube) during measurement time (t):

$$\delta(t) = \delta_s(t) + \delta_r(t) - \delta_t(t) \tag{3.6}$$

where; δ_s: thermal expansion of the sample, δ_r: thermal expansion of the push-rod and δ_t:thermal expansion of the supporting tube, a correction was required on the recorded displacement to extract solely the displacement belonging to the sample. The displacement error related to the expansion of push-rod and the supporting tube was corrected with a blank measurement (without specimen);

$$\delta_{blank}(t) = \delta_r(t) - \delta_t(t) \tag{3.7}$$

Finally, the CTE of the coatings (α_s) were calculated according to;

$$\alpha_s = \frac{1}{h_0} \cdot \frac{d\delta_s(t)}{dT} = \frac{1}{h_0} \cdot \frac{d(\delta(t) - \delta_{blank}(t))}{dT} \tag{3.8}$$

where h_0 and T denote the initial height of the specimen and the temperature. The details of the corrections and calculations are described in Mücke (2007).

Three-Point Bending Test

Time and temperature dependent elastic response and stress relaxation of the free-standing coatings were investigated using a three-point bending apparatus in the TMA facility. A schematic of the three-point bending arrangement located in the box furnace where the test sample is supported at the ends and the load is applied at the center is shown in Figure 3.3.
Rectangular samples cut from the free-standing layers with a length of 15 mm and a width of 4 mm were used for the test. The thicknesses of the specimens were measured with a double-sided optical profilometer using a chromatic white light sensor (CHR 3000) (CyberScan CT 300, CyberTechnologies, Ingolstadt, Germany). For each sample, 30,000 data points were acquired. The obtained averaged thickness values of the GZO layers ranged from 250 to 400 µm as a result of the different spray parameters and the individual deposition efficiencies. The applied loads (max. 0.1-0.3 N) were adapted to the different thicknesses to ensure comparable stress levels in the specimens.

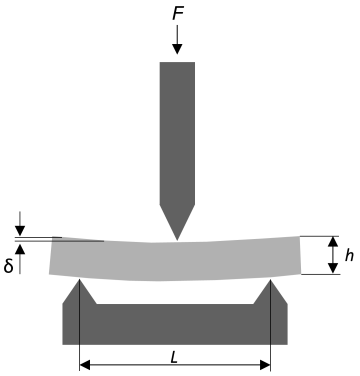

Figure 3.3: Schematic of the three-point bending apparatus used in the TMA facility.

A typical material strain response (δ) recorded during one loading-unloading cycle of the load (F) as a function of time is shown in Figure 3.4. An instantaneous elastic response during loading and unloading is monitored (from t_1 to t_2 and from t_3 to t_4). After

reaching to the max load (t_2), a short transition period from the elastic to the viscous behavior is observed followed by a secondary (viscous) creep during constant load period (Δt_{load}). The creep is partially recovered as can be seen after unloading of the load (t_4), nevertheless there is a residual displacement at t_5 as a result of the viscoplastic deformation of the sample.

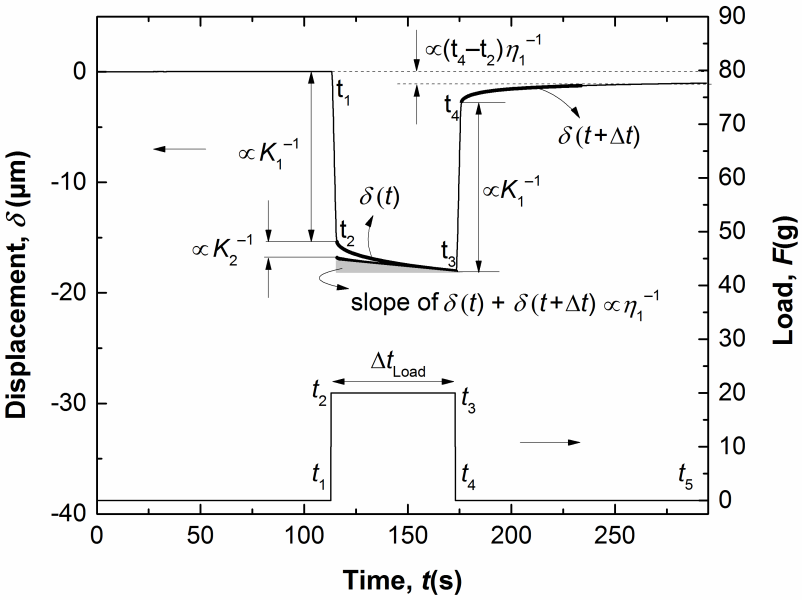

Figure 3.4: Viscoelastic/viscoplastic response of in-plane strain of a coating measured in three-point bending setup. The time points are defined as; t_1: the onset of loading, t_2: completed loading and reaching of max load, t_3: the onset of unloading, t_4: completed unloading and t_5: end of the cycle.

This strain response was approximately described by the Burgers model (Ahrens *et al.*, 2004) and given as a superposition of three contributions;

$$\varepsilon(t) = \frac{\sigma}{K_1} + \frac{\sigma}{\eta_1} \cdot t + \frac{\sigma}{K_2} \cdot \left(1 - exp\left[-\frac{K_2}{\eta_2} \cdot t\right]\right), \sigma(t) = const. \tag{3.9}$$

where ε: strain, σ: stress, K_1 and K_2: spring elements, η_1 and η_2: dashpot elements. Accordingly the first term of the equation represents the elastic strain, the second term describes the viscoplastic strain (creep) and the third term accounts for the viscoelastic behavior of the material which is equivalent to recovery effect after unloading.

For calculations of elastic modulus and viscosity, the displacements at t_2, t_3 and t_4 were defined by finding the local minimum and maximum using second derivative of the strain as shown in Figure 3.5.

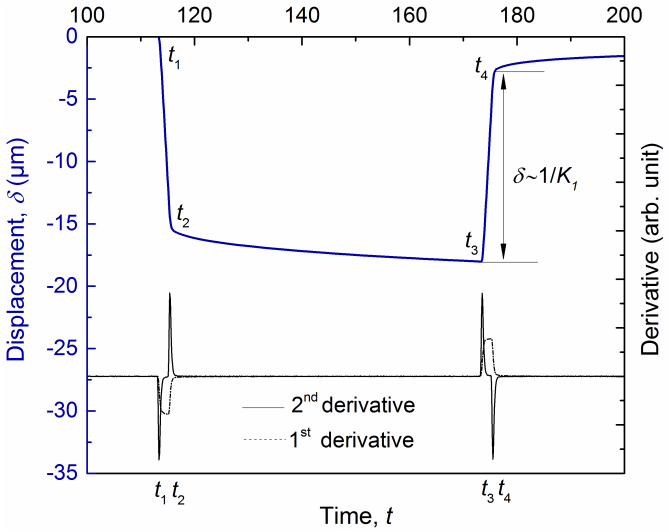

Figure 3.5: Determination of the accurate displacements at t_2, t_3 and t_4 from local minimums and maximums using second derivative of the measured strain data.

Based on that the elastic modulus and the viscosity of the coatings were calculated as follows:

- the displacement after load release ($\delta(t_4 - t_3)$) was used to calculate Young´s modulus in order to rule out the effect of potential creep (splat sliding) on the results during the loading period. As different loads were applied during measurement, force-displacement ratio was taken as the slope of the force-displacement function assuming it is linear. The elastic modulus (K_1=E) was calculated from

$$K_1 = E = \frac{F}{\lambda} \cdot \frac{1}{\delta(t_4 - t_3)}, \lambda = \frac{4bh^3}{L^3} \tag{3.10}$$

where λ is a geometrical factor and b, h and L denote the width and height of the sample and the distance between the supports pin.

- the viscosity (η_1) was calculated from either the residual displacement at the end of the cycle or from the slope of the creep during constant load period (Δt_{load}) (Figure 3.4).

(i) The former was calculated according to;

$$\eta_1 = \frac{F}{\lambda} \cdot \frac{t_4 - t_2}{\delta(t_5) - \delta(t_1)} \tag{3.11}$$

(ii) For the latter, a linear creep behavior was acquired by summing up the displacement under constant load ($\delta(t)$) and the displacement recorded during recovery after t_4 ($\delta(t + \Delta t)$) and the linear regression for $\delta(t) + \delta(t + \Delta t)$ was calculated from $t_2 + (t_3 - t_2) \cdot \frac{1}{3}$ to t_3.

3.3.5 Laser Flash Method

The laser flash method is commonly used to measure thermal diffusivity of the solid materials for the thermal conductivity evaluation in a temperature range up to ∼2500 K (Tong, 1994). It involves applying a flash of laser radiation to the surface of the specimen and then measuring the rate of temperature rise at the back surface of the specimen using an infrared detector (Figure 3.6a). The heat provided by the laser flash at the front surface is conducted through the specimen and reaches to the back surface. Thereby, the specimen surfaces must have high emissivity to maximize the amount of thermal energy transmitted from the front surface and to maximize the signal observed by the infrared detector.

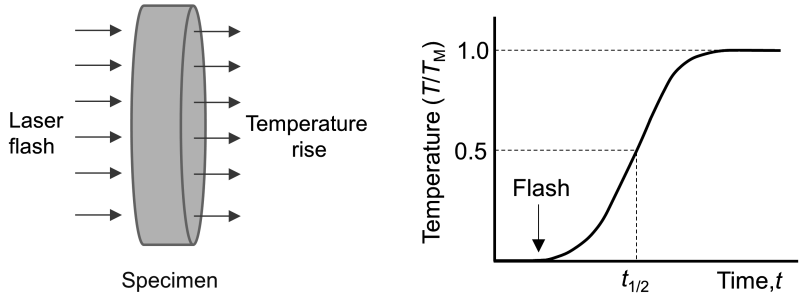

Figure 3.6: Testing geometry with the laser flash originating from the left (a), temperature rise at the back side of the specimen as a function of time (b). T_M indicates the maximum temperature. Reproduced from (Parker *et al.*, 1961).

Using the method, the thermal diffusivity of the specimen (α_d is used here to not to be confused with the CTE, which is also denoted by α) is determined. Considering the laser pulse is instantaneously and uniformly absorbed at the front surface of a solid with uniform thickness h, α_d (m^2/s) is given by Parker *et al.* (1961);

$$\alpha_{\mathrm{d}} = \left(\frac{1.38h^2}{\pi^2 t_{1/2}}\right) \tag{3.12}$$

where $t_{1/2}$ is the time required for the back surface to reach half of the maximum temperature rise (Figure 3.6b).
If the specific heat (C_{p}, at constant pressure, J/(gK)) and the density (ρ, g/m^3) of the material are also known, the thermal conductivity (k, W/mK) can be calculated using;

$$k = \alpha_d \cdot C_{\mathrm{p}} \cdot \rho \tag{3.13}$$

$C_{\mathrm{p}} \cdot \rho$ is given as volumetric specific heat which gives the amount of heat required to increase the temperature by 1 K for a unit volume of the material.
In this study, the thermal diffusivity and specific heat capacity of the coatings were recorded by a laser flash (THETA, Netzsch, Germany) and simultaneous thermal analysis apparatus (Model STA 449C, Netzsch, Germany), respectively. Measurements were conducted in Hot Materials Lab (N-M), Forschungszentrum Jülich, Germany. Free-standing coatings were cut in disk shape in a diameter of 10 mm and 5 mm with 2 mm thickness for the analyses and the surface of the specimens were polished to obtained coplanar front and rear surfaces. Finally the front and back surface of the specimens were coated with a thin graphite layer and the measurements were conducted between room temperature and 1400 °C with 200 K steps. The density of the specimens was measured according to Archimedes´ principle.

3.3.6 Thermal Cycling Test

The thermal cycling test under a thermal gradient through the sample is used to evaluate the lifetime of the TBCs. TBC coated Inconel 738 disk-shaped substrates, which had a diameter of 30 mm and a thickness of 3 mm, were used for the test. The outer edge of the substrates was machined in a radii of curvature of 1.5 mm to reduce the stress level and avoid failure at sharp edges. At gas burner test facilities which are operating with a natural gas/oxygen mixture, the burner flame giving a homogeneous temperature distribution was positioned on the coated surface of the sample during heating. At the same time, the back side of the substrate was cooled by compressed air to achieve the desired temperature gradient through the thermal barrier coating.
During the test, surface temperature was measured with an infrared pyrometer operating at a wavelength of 9.6-11.5 µm and a spot size of 8 mm. The emissivity of the GZO coatings was assumed to be constant and set to its maximum value of 1. This describes well

the emissivity of YSZ, which has been determined to > 0.98 at this wavelength range and at elevated temperatures (Eldridge *et al.*, 2009). Additionally, the substrate temperature was measured by a thermocouple located in the center of the substrate. The surface temperature was fixed at 1400±50 °C, while the substrate temperature was adjusted to 1050±30 °C. Using the thermal conductivities of the coatings and the substrate, bond coat temperatures were calculated to be about 30 K higher than the measured substrate temperatures. After thermal cycling, the mean substrate and surface temperatures during the heating phase were calculated by disregarding the temperature during the fast heating phase at the beginning of each cycle.
In the test facility, after a 5 min high-temperature period, the burner was automatically removed and the surface was additionally cooled for 2 min using compressed air to achieve rapid cooling conditions. Cycling was stopped when a clearly visible spallation ($\geq$ 20% of the sample surface area) occurred. More details of the test setup and procedure are described in Traeger *et al.* (2003).

3.3.7 Microscopy

Metallographic cross-sections or fracture surfaces of the coatings were investigated with a scanning electron microscope (SEM) (Carl Zeiss NTS GmbH, Oberkochen, Germany) for microstructural and failure mode analysis. The secondary electron (SE) and and back-scattered electron (BSE) imaging modes were used to acquire topographical and compositional contrast, respectively.
Cross sections of the GZO single splats were prepared and analyzed by a FIB (Focused Ion Beam) assisted SEM in the Department of Materials and Environmental Engineering, Università degli Studi di Modena e Reggio Emilia, Italy. The FIB assisted cross sections were prepared with a FEI Strata^{TM} DB235 dual beam machine, combining a Field Emission Scanning Electron Microscope (FE-SEM) column and a high-resolution FIB column equipped with a Ga Liquid Metal Ion Source (LMIS). A platinum thin film was first deposited to protect the area of interest from surface damage during the ion beam machining. A larger ion beam current (7 nA) was then used to mill a pocket in the protected area. The sidewall of the pocket, i.e., the area of interest, was subsequently polished using a lower beam current (300 pA). The samples thus prepared were observed in situ, under an angle of 52°, using both the ion probe (for maximum microstructural contrast) and the electron probe (for maximum morphological contrast). Secondary electron images were acquired in both cases.

4 | Results and Discussion Part 1: Microstructure, Composition and Lifetime Relations

4.1 General Understanding of GZO Processing and its Relation to Lifetime

In this section, optimization of the atmospheric plasma spray current for the manufacturing of GZO coatings (using GZO 357 H powder) by means of monitored in-flight particle temperatures will be presented. The impacts of the selected spray parameters on the porosity, microstructure and chemical composition of the GZO coatings will be characterized. As the investigation of the gadolinia evaporation during APS processing is one of the objectives of this study, compositional characterizations of the GZO single splats will be discussed in addition to the as-sprayed GZO coatings. For this purpose, cross-section imaging and depth- profile analysis of the GZO splats via FIB-SEM and TOF-SIMS techniques, respectively, will be introduced. Finally, thermal cycling lifetime of YSZ/GZO double layers sprayed with selected parameters will be evaluated and compared to the standard YSZ.

4.1.1 Particle Temperature Measurements as an Approach for Spray Current Optimization

In-flight particle surface temperature distributions of GZO were measured in a spray current range of 300 A-425 A with 25 A steps at a fixed stand-off distance of 90 mm (Figure 4.1). The particle temperature distributions were fitted with mono or bimodal Gaussian distributions and characteristic peaks were indicated showing solid, solidifying and liquid particle fractions with respect to the melting temperature (T_m) of the GZO. According to this definition; the fractions below the temperature of the melting point ($T < T_m$) are exhibited as solid (unmelted) or re-solidified particles, the fractions at the melting temperature ($T \approx T_m$) are indicated as solidifying particles and finally the fractions above the melting temperature ($T > T_m$) are displayed as liquid particles on the graphs.

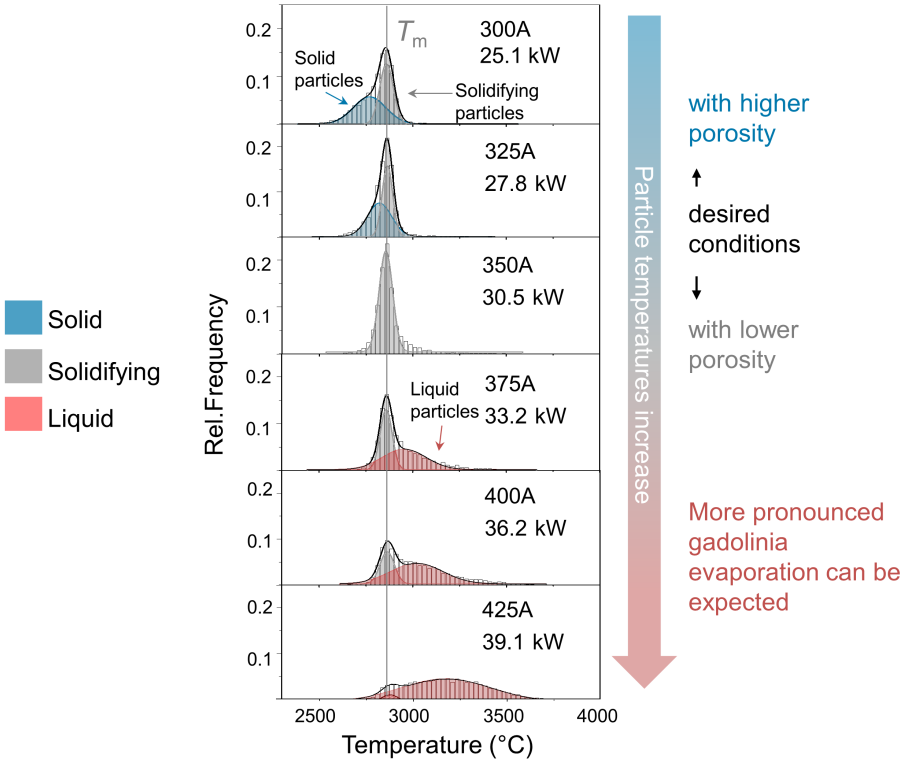

Figure 4.1: Particle temperature distributions measured by two-color pyrometry at spray current levels between 300 A and 425 A. T_m indicates melting temperature of GZO.

With this approach, highly porous coatings can be expected to be sprayed up to 350 A due to presence of unmelted or re-solidified solid particles. Furthermore, from compositional point of view, higher gadolinia evaporation rates can be anticipated above 400 A considering the increase in the particle temperatures leading liquid particles to dominate the distributions. Based on this assumptions, two low (300 A and 325 A) and two high (450 A and 525 A) spray currents were decided to be tested and combined with different stand-off distances (Table 4.1).

Table 4.1: Spray currents and stand-off distances selected to be tested for spraying of GZO.

Spray current (A)	Stand-off distance (mm)	Spray protocol
300	75	M-12-360-TP
325	95	M-12-349-TP
325	75	M-12-350-TP
325	65	M-12-446-TP
450	95	M-13-223-TP
525	95	M-13-224-TP

4.1.2 Porosity and Microstructure of GZO Coatings

The pore size distributions of the free-standing GZO coatings sprayed with varied spray parameters (Table 4.1) as determined by mercury porosimetry are shown in Figure 4.2. The total porosity range changes from 8 to 32 % by volume for the manufactured coatings. The results reveal a typical bimodal distribution of small (<1 µm) and large (>1 µm) pore radii. The small pores are typically attributed to unmelted particles, intersplat and intrasplat cracks, while macrocracks and globular pores are accounted for larger pore sizes within the coatings.

The obtained pore size distributions indicate that the process parameters in terms of spray current and stand-off distance have a significant influence on the porosity levels of the coatings. Particularly, the lower spray currents greatly increase the porosity level, which was expected based on the particle temperature measurements. On the other hand, the influence of stand-off distance is not clear taking into account the results obtained at 65, 75 and 95 mm distances with 325 A spray current. The larger stand-off distances and hence longer time of the flight of the particles, which might lead to reduced particle temperatures, are expected to contribute to the higher porosity contents. However, it was observed that the 65 and 95 mm stand-off distances yield the same ∼26 % cumulative porosity, whereas 75 mm distance introduces ∼18 % porosity at 325 A.

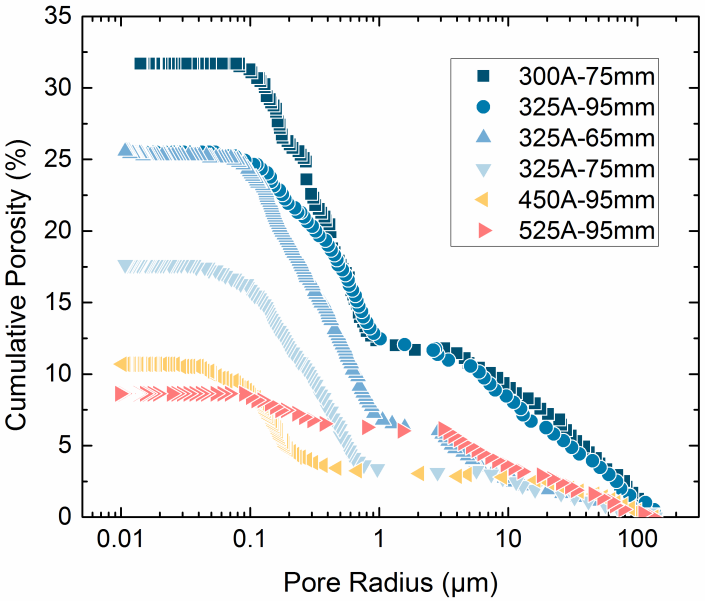

Figure 4.2: Pore size distributions of the GZO coatings sprayed with different spray currents and stand-off distances.

The reason of the obtained high porosity at 65 mm can be attributed to too short time of flight of the particles. The short interaction time of the plasma and the particles may result in insufficient heat transfer to the particles, hence incomplete melting of them. These partially molten particles can be partly responsible for the high porosity of the coating.

Figure 4.3 shows the microstructures of the as-sprayed GZO coatings. At 300 A, which is the lowest spray current that was used here, very fine particles (darker gray shadings) dominate the microstructure of the coating. Their prevailing effect progressively was reduced with the increase in the spray current up to 525 A.

A closer look to the fine particles on a fracture coating surface is shown in Figure 4.4a, while another image which belongs to a particle surface of GZO 357 H feedstock is presented in Figure 4.4b. Similarity of size and shape of the structures clearly indicates that the fine particles observed in the as-sprayed microstructures are unmelted feedstock particles. The very fine voids among these particles contribute to the small pore size distribution of the coatings leading to a high cumulative porosity at low spray currents. Their amounts decrease with the increase in the particle temperatures at higher spray currents and results in low porosity contents.

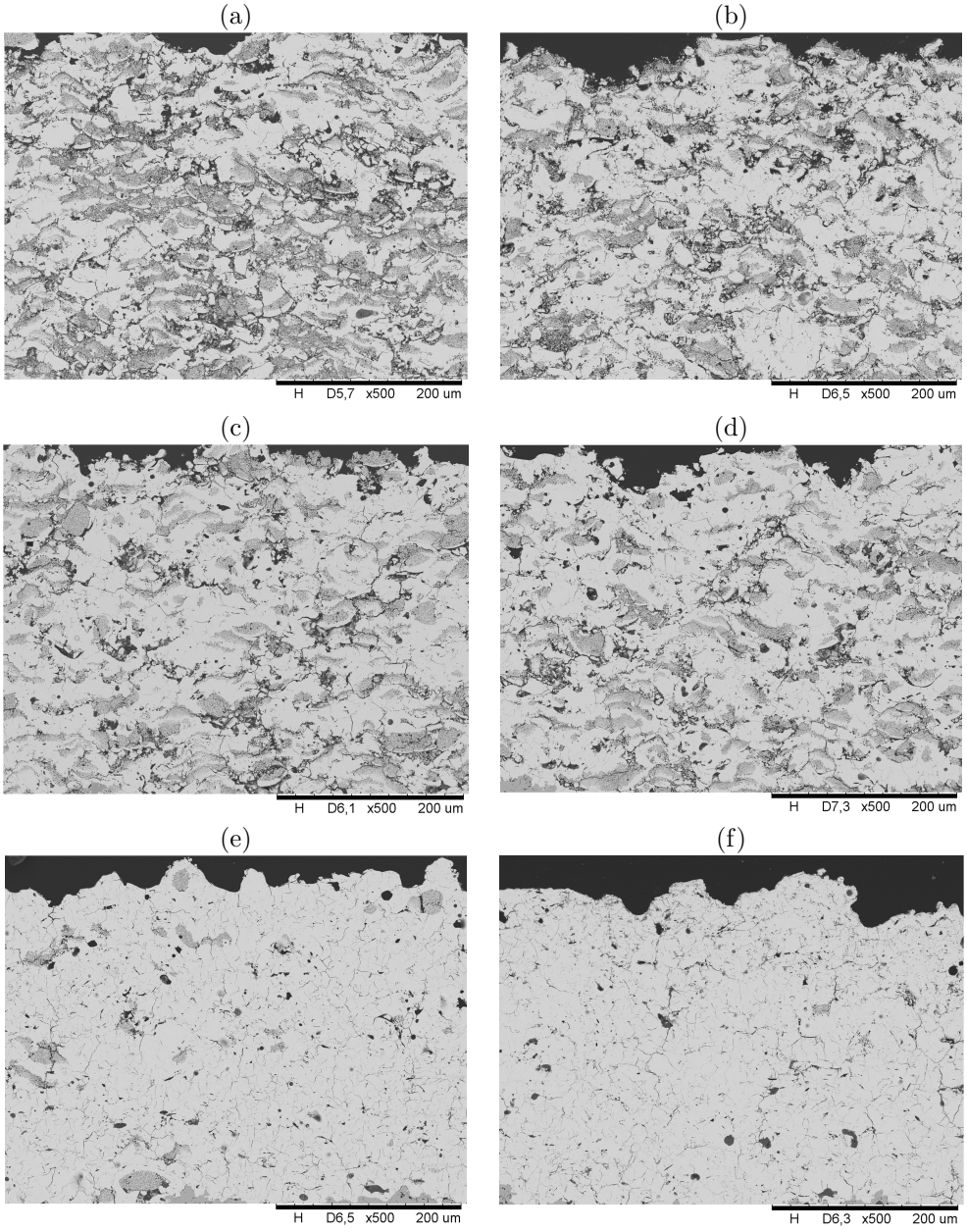

Figure 4.3: Cross-section microstructure images of the as-sprayed GZO coatings sprayed with: 300 A-75 mm (a), 325 A-95 mm (b), 325 A-65 mm (c), 325 A-75 mm (d), 450 A-95 mm (e), 525 A-95 mm (f).

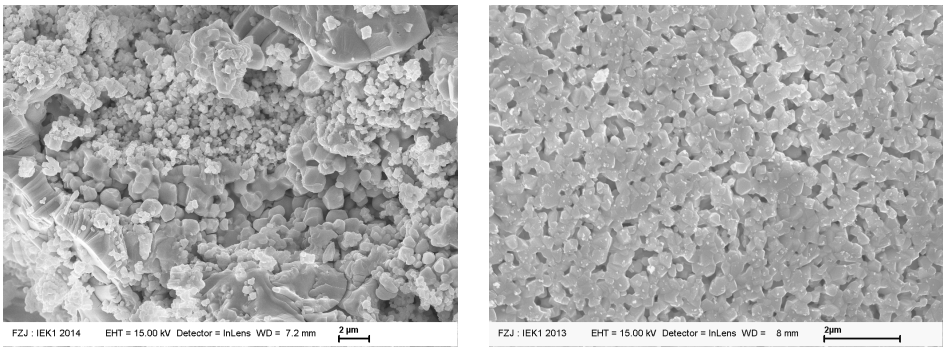

(a) (b)

Figure 4.4: Fracture surface secondary electron (SE) SEM image of the as-sprayed GZO coating (300 A-75 mm) (a) and a close up SE image of the GZO feedstock (b).

This can also explain the higher cumulative porosity observed at 65 mm than 75 mm, due to very short plasma-particle interaction time at 65 mm distance leading to deficient heating of the particles as mentioned above.

4.1.3 Phase Composition of the GZO Coatings

The XRD analysis of the spray-dried and sintered GZO feedstock yields solely pyrochlore phase, while as-sprayed GZO coatings show defect-fluorite phase as presented in Figure 4.5. According to the binary phase diagram of ZrO_2-Gd_2O_3 (see chapter 2, Figure 2.12), solidification from the liquid phase starts with the fluorite phase and it is transformed into pyrochlore with further cooling (below ∼1550 °C) in the homogeneity range of the pyrochlore phase under equilibrium conditions. However, it appears that the rapid solidification on the substrate during the spraying process kinetically constrains the necessary atomic arrangements to generate an ordered pyrochlore superlattice structure. This results in the formation of a disordered pyrochlore phase* in the as-sprayed coatings which shows no characteristic superstructure reflexes of the pyrochlore (331, 511, etc.) unlike the powder as shown in the diffractograms. Similar findings were reported earlier in the literature both for the plasma-sprayed and the electron-beam deposited pyrochlore materials (Zhao *et al.*, 2011; Mauer *et al.*, 2012; Munawar *et al.*, 2014). Moreover, it is worth mentioning here that because the as-sprayed coatings are consisted of re-solidified splats as well as the unmelted particles in particular at low spray currents, a combination of defect-fluorite and pyrochlore phases can be expected in the coatings dominated by

*It is typically referred to a "defect-fluorite phase" in the literature (Wu *et al.*, 2002a; Vaßen *et al.*, 2004; Mazilin *et al.*, 2014) and will do so here.

the former. Smaller pyrochlore fractions are difficult to quantify because it is based on the weak pyrochlore reflexes.

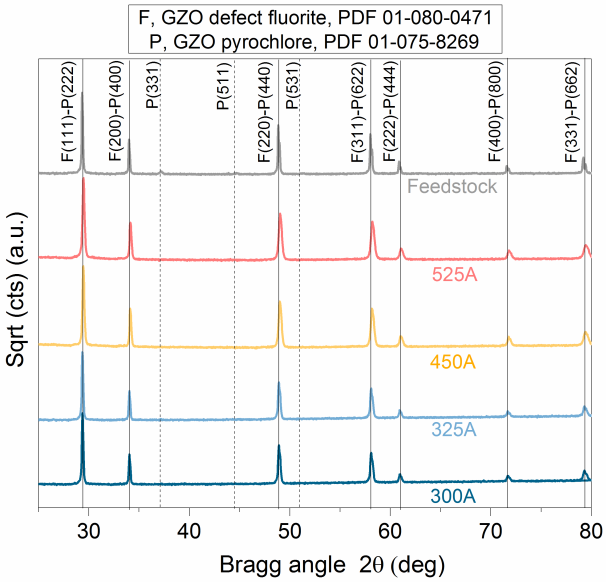

Figure 4.5: X-ray diffractograms of the GZO 357 H feedstock and as-sprayed GZO coatings sprayed at varied currents.

4.1.4 Chemical Composition of the GZO Coatings and Single Splats

Chemical Analysis and Lattice Parameter Refinement of the GZO Coatings

Figure 4.6 shows a comparison of the gadolinia content of the GZO feedstock and the as-sprayed coatings determined by chemical analysis. As noted before, the GZO 357 H feedstock has a slight excess of gadolinium (33.8 ± 0.13 mol %, Gd/Zr atomic ratio is ∼1.03) compared with the stoichiometric composition. The results reveal that the gadolinia content in the as-sprayed GZO coatings sprayed at 300 A-75 mm, 325 A-95 mm, 450 A-95 mm and 525 A-95 mm currents and stand-off distances, respectively, exhibits a decreasing trend with increasing spray currents (Figure 4.6). This decrease in the gadolinia content implies higher evaporation rates of the gadolinia at the higher spray currents. However, due to the excess gadolinia content of the powder, the compositions

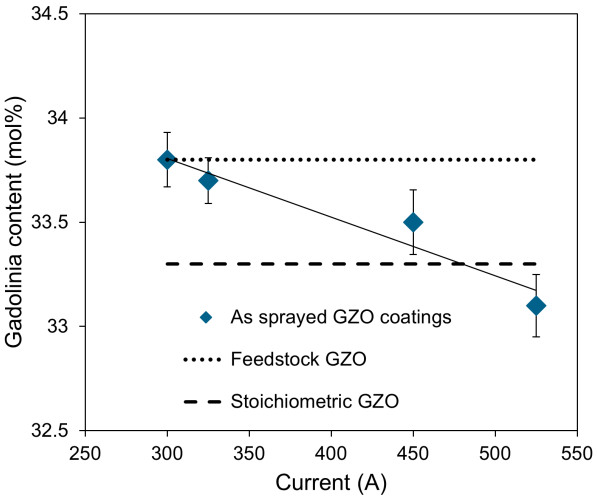

Figure 4.6: Gadolinia contents of the GZO feedstock and as-sprayed GZO coatings determined by chemical analysis vs.spray current. The stand-off distance is 95 mm with the exception of 75 mm used at 300 A.

of the coatings are still close to stoichiometric composition even at high current levels. At 525 A, the coating has a gadolinia content of 33.1 ± 0.15 mol % corresponding to an approximately 0.99 Gd/Zr atomic ratio.

The defect-fluorite and pyrochlore structures of the GZO coatings and the feedstock powder, respectively, were refined from XRD by Pawley´s method (Pawley, 1981) of refinement and the results are shown in Figure 4.7a. The graph shows the reduced lattice parameter of the pyrochlore phase (divided by factor of 2) for the comparison with the defect-fluorite phase. The slightly larger lattice parameter of the feedstock than the stoichiometric composition can be attributed to the excess gadolinia in the powder. The results also indicate that the cubic lattice parameter decreases with the increasing spray currents from 300 A to 525 A. This can be associated with the change in the stoichiometry as a result of the evaporation of gadolinia. Vacant larger gadolinium cation sites which form due to evaporation are occupied by smaller zirconium cations and oxygen vacancies accompanied by these gadolinium cations are filled. These rearrangements in the cubic lattice likely resulted in a reduction of the lattice parameter.

Applicability of the Vegard´s law (Vegard, 1921) to the lattice parameters of cubic Gd_2O_3-ZrO_2 solid solution was shown in the literature (Yashima *et al.*, 1992; Zinkevich *et al.*, 2005).

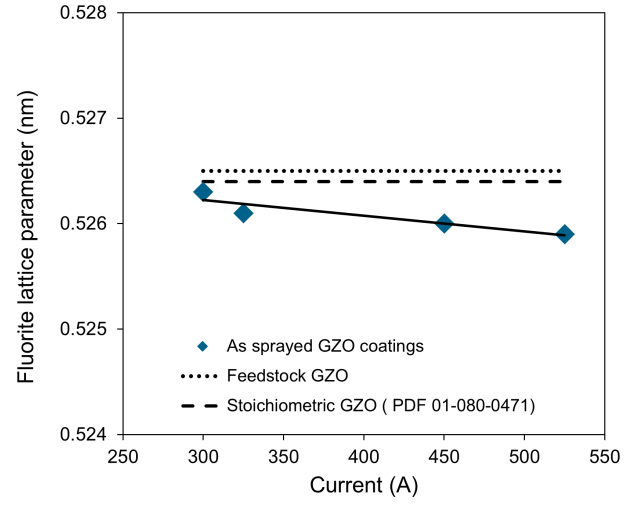

(a)

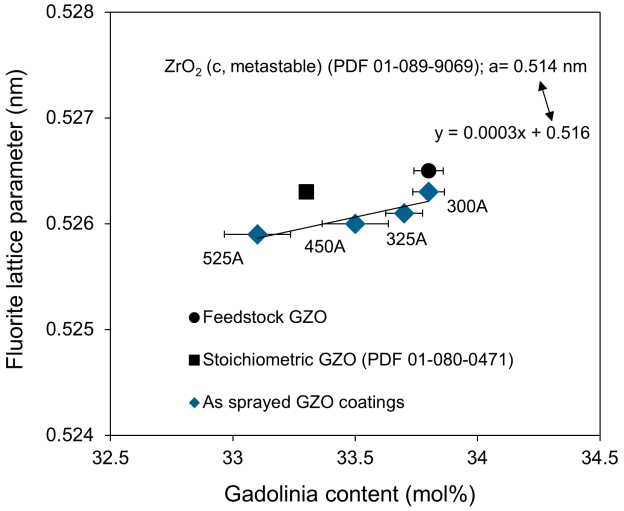

(b)

Figure 4.7: Lattice parameter of the as-sprayed GZO coatings determined by Pawley´s method vs. spray current (a) and vs. gadolinia content (b) determined by chemical analysis. The stand-off distance is 95 mm with the exception of 75 mm used at 300 A.

The lattice parameter versus gadolinia content graph of the as-sprayed GZO coatings also exhibit a linear relationship suggested by this law (Figure 4.7b). The lattice parameters as well as the gadolinia content of the coatings are reduced consistently with the increase in the current levels as a result of the evaporation of gadolinia. Nevertheless, an

uncertain lattice parameter difference was noticed for the same gadolinia content level of feedstock and the coating sprayed at 300 A. If this data is extrapolated to the zero mol % gadolinia content, the lattice parameter becomes 0.516 nm which approaches to the lattice parameter of metastable cubic zirconia (0.514 nm). Obviously, more gadolinium sites are occupied by zirconium cations with increasing evaporation and eventually the full depletion of gadolinia leads to the formation of the metastable zirconia. Thus, the implication is that the variation of the lattice parameter between pure zirconia (ZrO_2) and stoichiometric zirconate ($RE_2Zr_2O_7$) can be used to estimate the amount of rare-earth oxide (RE_2O_3) evaporation in zirconia and rare-earth oxide solid solutions, as shown already for $La_2Zr_2O_7$ in the literature (Mauer *et al.*, 2012).

Cross-Section Imaging of the GZO Single Splats via FIB-SEM

Cross-sections of the GZO single splats sprayed with one low (325 A, M-13-165-TP) and one high spray current (525 A, M-13-166-TP) were analyzed to investigate the homogeneity of chemical composition through thickness of the splats. Because a compositional gradient can be expected, if the gadolinia evaporates from the particle surfaces during the flight likewise lanthana as shown for $La_2Zr_2O_7$ in the literature earlier (see chapter 2, Figure 2.19).

A GZO single splat sprayed at 325 A exhibiting a fragmented morphology with a non-flattened, partially unmelted core and a flattened, fully melted rim which bears evidence of low particle temperature is shown in Figure 4.8 a. The rim of the splat is clearly microcracked due to quenching effects. FIB-cutting of the flattened rim displays a thin (≈1 µm), smooth layer with numerous transverse microcracks (Figure 4.8 a1). The ion channeling contrast of the micrographs in Figure 4.8 a1- a2 also clarifies that the splat exhibits through-thickness columnar grains of about 200 nm in width, which is quite typical for thermal spray ceramic splats (Sampath and Herman, 1996; Bolelli *et al.*, 2010). Furthermore, the absence of any through-thickness contrast gradient suggests that the chemical composition of the GZO is homogeneous within the detectability limits of this method across the splat.

A GZO single splat sprayed at 525 A, which is completely flattened and extensively microcracked indicating a higher particle temperature is shown in Figure 4.8 b. The splat thickness is lower than that of sprayed at the 325 A, suggesting that more extensive flattening of the GZO impacting onto the substrate with higher velocity and lower viscosity was possible (Figure 4.8 b1-b2). From compositional point of view, similar to what was monitored at 325 A, the splat exhibits a chemically homogenous through-thickness columnar microstructure.

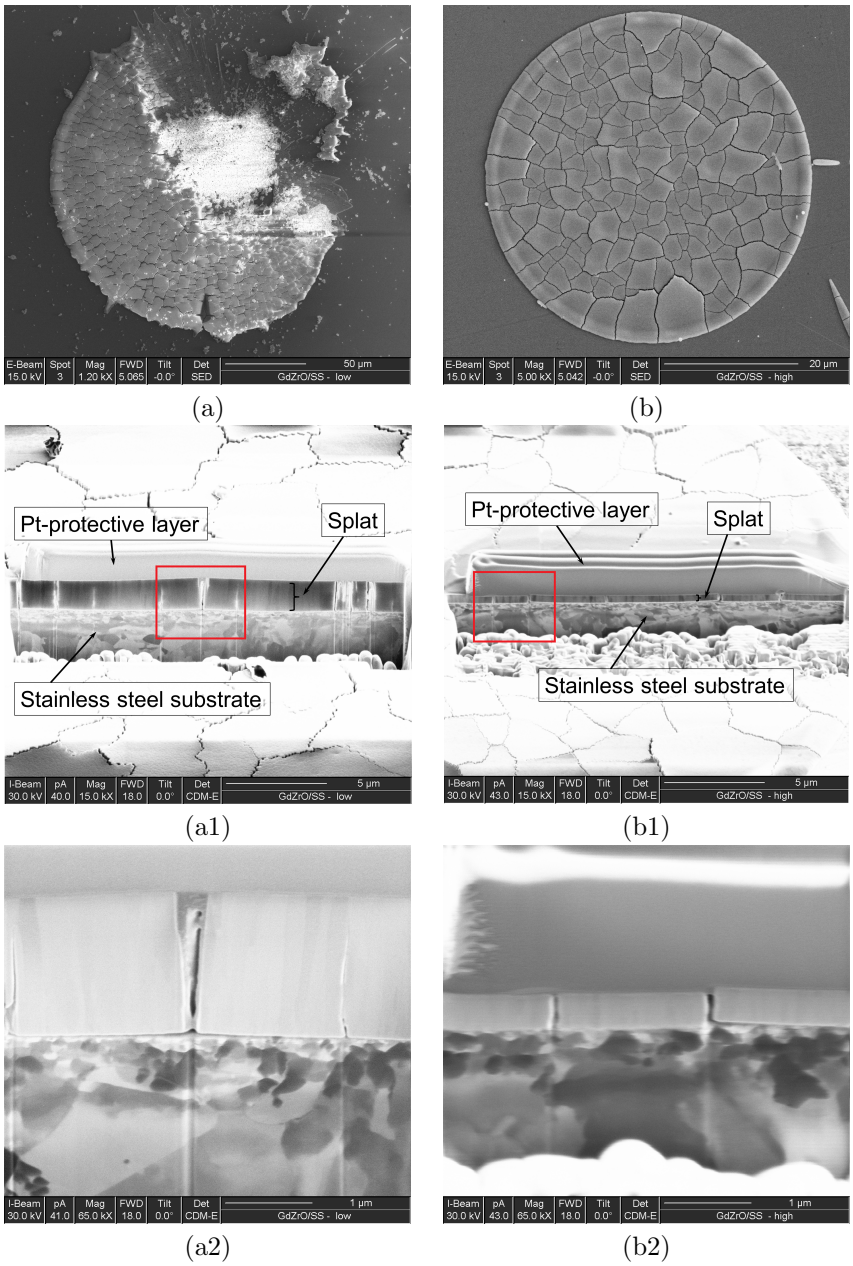

Figure 4.8: Secondary electron SEM images of the single splats sprayed with 325 A (a) and 525 A (b). Ion-beam micrographs of the FIB cross-sections of the splats sprayed with 325 A (a1-a2) and 525 A (b1-b2). a2 and b2 images are taken from the regions indicated with red-boxes in a1 and b1, respectively. By courtesy of Dr. Luca Lusvarghi, Università degli Studi di Modena e Reggio Emilia, Italy.

Depth Profile Analysis of the GZO Splats via TOF-SIMS

With the same through-thickness chemical concentration analysis of interest, elemental distributions of the splats (325 A and 525 A) was investigated by SIMS depth profiling, which offers a detection sensitivity in the ppm range for most elements. The splats were sputtered by a focused Cs^+ ion beam and the intensities of the emitted substances were monitored as a function of the sputtering time. Figure 4.9 a-b shows the detected intensity of $GdO^-$and ZrO^- secondary ions during the sputtering. The FeO intensity is also given on the plots to indicate splat-steel substrate interface.

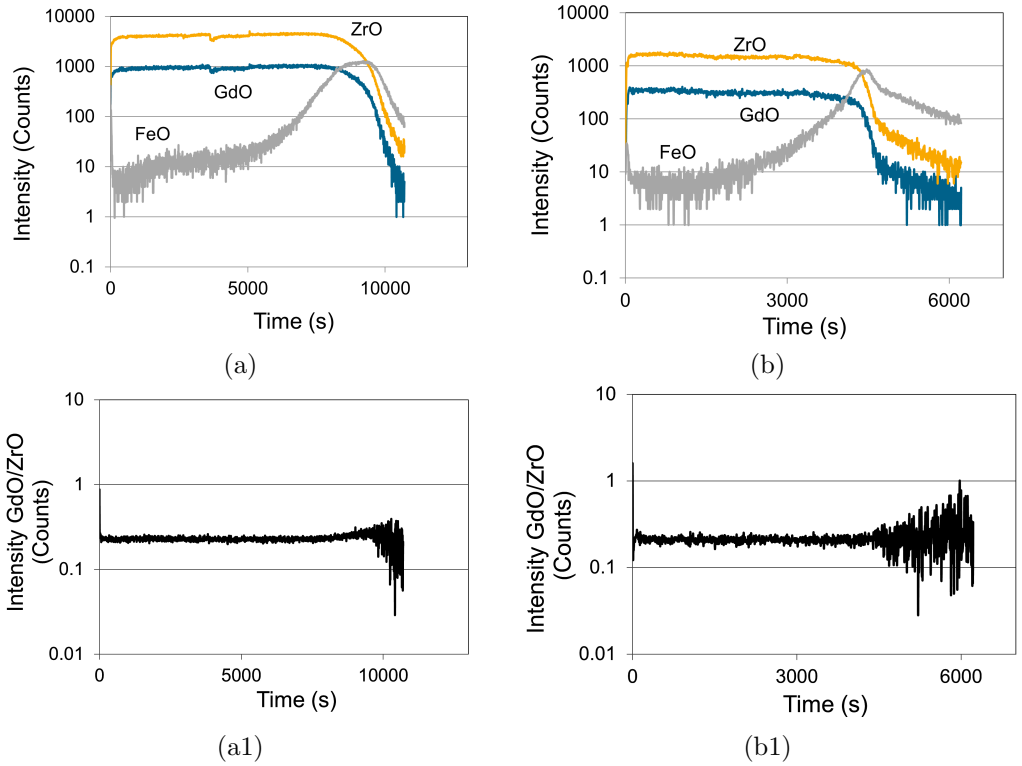

Figure 4.9: Depth profiles taken from the single splats sprayed at 325 A (a) and 525 A (b). The bottom row shows relative secondary ion intensity ratios (GdO^-/ZrO^-) (a1-b1) calculated from (a) and (b). The sputter time is proportional to the sputtered depth and it is assumed that the sputter rates are identical.

Similar to the observation on the FIB-cut cross-section surfaces, the splat thickness is lower at 525 A than that of 325 A, suggesting a more extensive flattening at the higher current. The relative secondary ion intensity ratios (GdO^-/ZrO^-) were calculated for the

each splat to describe the composition at a certain sputtered depth and are given as function of time in Figure 4.9 a1-b1. The results display flat relative intensity profiles for both splats sprayed at 325 A and 525 A, implying a homogenous chemical composition through their thicknesses.

4.1.5 Thermal Cycling Lifetime of YSZ/GZO Double Layer TBCs

The YSZ/GZO double layer TBCs (100 µm/400 µm thickness ratio) were manufactured for the assessment of the thermal cycling lifetime. Initially selected spray currents and stand-off distances (see in Table 4.1) were used for the GZO layer processing of six different double layer systems. All the YSZ layers were sprayed with a 470 A current and 200 mm stand-off distance in these systems introducing a cumulative 12 % porosity. A cross-section SEM image of an as-sprayed double layer system is given in Figure 4.10. Two specimens were tested from each double layer system in the burner rig test facility and a comparison of their lifetime performances with a standard YSZ (WDS 2324) and single layer GZO TBC (WDS 3046-3047) is shown in Figure 4.11. The monitored surface ($T_{\text{surf.}}$) and calculated bond-coat temperatures (T_{BC}) of each specimens at burner rig test as well as their number of cycles to failure can be also found in Table 4.2.

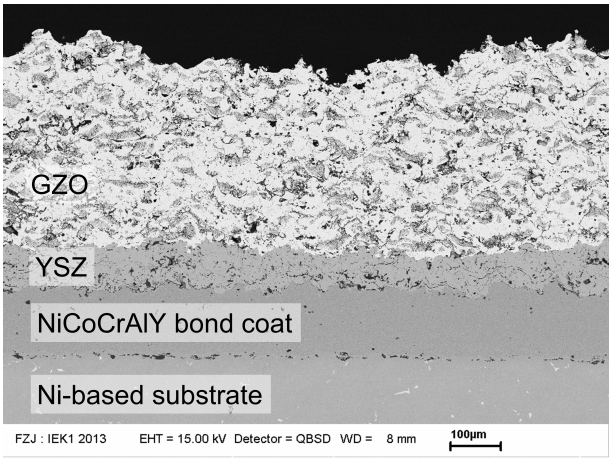

Figure 4.10: Cross-section SEM image of an as-sprayed YSZ/GZO double layer TBC system (GZO (325 A-75 mm)/YSZ).

Results reveal that the double layer YSZ/GZO TBC concept is able to provide significant lifetime improvement at 1400 °C surface temperature compared to the standard YSZ. The single layer GZO, on the other hand, cannot survive more than 20 cycles due to

low toughness and thermochemical compatibility issues as introduced previously. The lifetime improvement in the double layer systems seems to be only pronounced for the double layers with high porous GZO layers, as the double layers with the GZO porosity below 18 % showed very early failures.

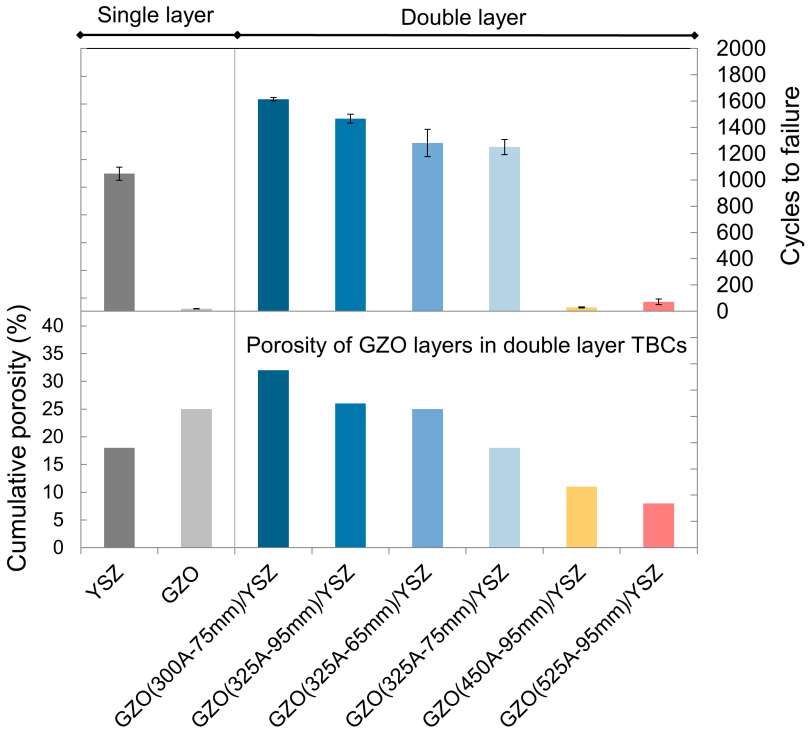

Figure 4.11: Comparison of the thermal cycling performances of single and double layer TBCs at 1400 °C surface temperature. Burner rig test results indicating the average cycle numbers of the two specimens are plotted in the upper graph. The error bars show the max. and min. number of cycles of two tested specimens revealing good reproducibility. Cumulative porosity of the GZO and YSZ layers are also shown in the bottom graph.

The failure modes of the thermally cycled double layers both with photos of the specimens and cross-section SEM micrographs are presented in Figure 4.12. The failure mode of the coatings are changed from TGO growth driven failure (Figure 4.12 a-d) to YSZ/GZO ceramic interface delamination (Figure 4.12 e-f) consistent with the transition from long to short lifetime. Second specimens of the each system also showed the same behaviors.

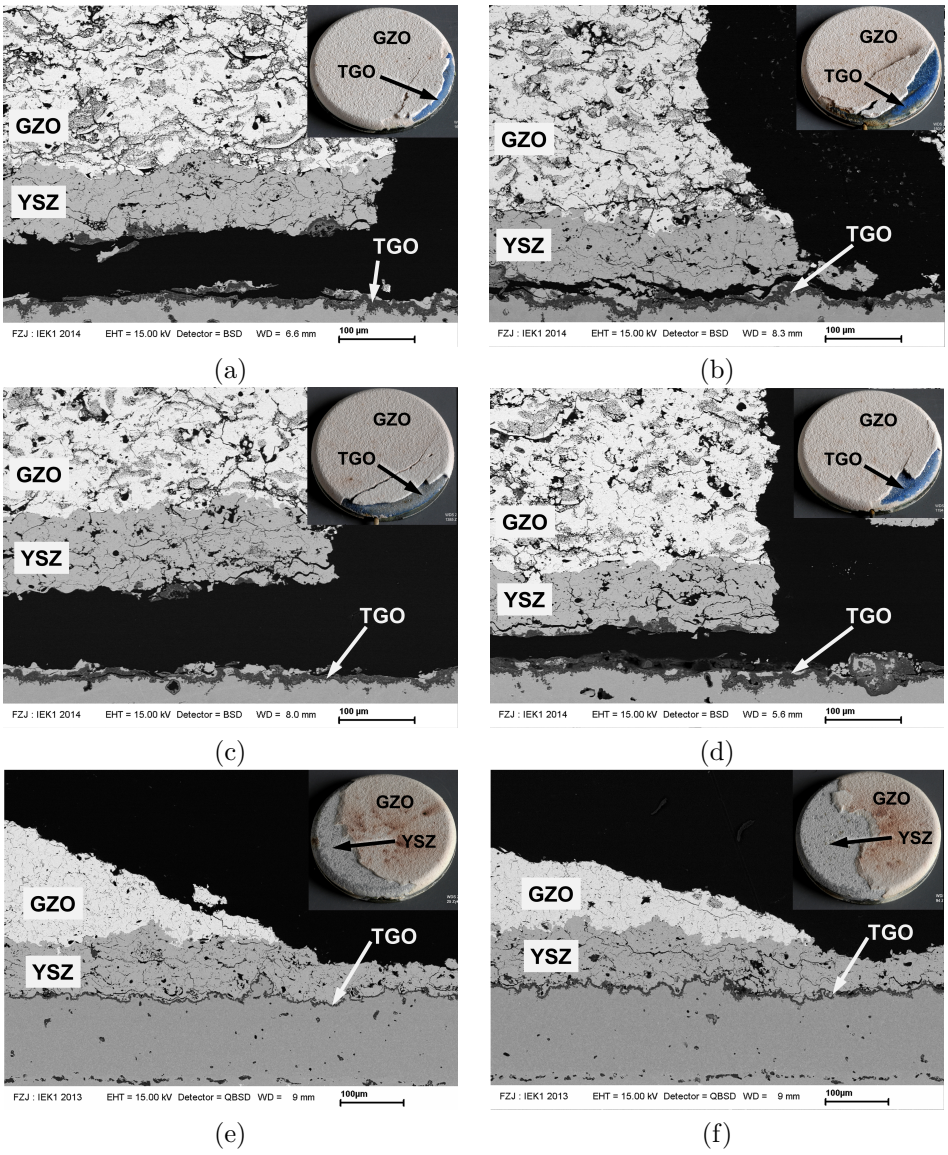

Figure 4.12: Photos and cross-section microstructures showing the failure modes of thermally cycled GZO/YSZ coatings sprayed with different GZO spray parameters; (a) 300 A-75 mm (WDS 2532), (b) 325 A-75 mm (WDS 3535), (c) 325 A-95 mm (WDS 2538), (d) 325 A-65 mm (WDS 2541), (e) 450 A-95 mm (WDS 2996), (f) 525 A-95 mm (WDS 3000), current and stand-off distances, respectively.

Table 4.2: Recorded surface ($T_{\text{surf.}}$) and bond-coat temperatures (T_{BC}) as well as lifetime cycles of two tested specimens for each set of spray parameters.

Coating systems and internal specimen codes	$T_{\text{surf.}}$ **(°C)**		T_{BC}**(°C)**		**Lifetime (number of cycles)**	
	1st	**2nd**	**1st**	**2nd**	**1st**	**2nd**
GZO (300 A-75 mm)/YSZ (WDS 2532&2533)	1390	1384	1053	1066	1627	1602
GZO (325 A-95 mm)/YSZ (WDS 2538&2539)	1389	1382	1067	1069	1501	1433
GZO (325 A-65 mm)/YSZ (WDS 2541&2542)	1386	1394	1079	1065	1177	1385
GZO (325 A-75 mm)/YSZ (WDS 2535&2536)	1389	1388	1064	1069	1194	1307
GZO (450 A-95 mm)/YSZ (WDS 2996&2997)	1409	1397	1075	1084	25	33
GZO (525 A-95 mm)/YSZ (WDS 2999&3000)	1373	1372	1067	1075	50	94

Although the characterizations of the GZO single splats suggested a homogenous chemical composition gradient, as the lattice parameters and the chemical analysis results of the GZO coatings sprayed at high spray currents (450 A) showed slight deviations from the stoichiometric composition, the low porosity as well as the evaporation of gadolinia can be considered as potential reasons of these early failures. While the evaporation can introduce secondary undesirable phases (e.g. metastable zirconia) to the structure, both the low pore volume fraction leads to a high elastic modulus. A higher elastic modulus implies greater elastic strain energy storage in the coating associated with the developed compressive stresses upon cooling from the elevated temperature. The stored energy is released by crack propagation and Griffith's energy release rate fracture criterion suggests that the crack propagates when the energy release rate (G) exceeds a critical value for the material (G_c) (Knott, 1973)

$$G = \frac{1-\nu^2}{E} K_I^2 \geq G_c \tag{4.1}$$

where v is the Poisson ratio, E is the elastic modulus and K_{I} is the stress intensity factor.

Thus, the higher elastic strain energy storage in the dense coatings favors the crack propagation and the early failure of the system.

4.1.6 Phase Composition of the Thermally Cycled GZO Coatings

XRD diffractograms of the two cycled specimens (300 A and 525 A) taken from the surface of GZO layers can be seen in Figure 4.13. Results indicate that the ordering degree of the as-sprayed structure is increased after exposure to 1400 °C. The pyrochlore superstructure reflexes, (111), (311), (331), (511) are clearly evident in the XRD pattern of the cycled coating system with the GZO layer sprayed with 300 A-75 mm current and stand-off distance. Some of these superlattice reflexes are either absence or lower in intensity for the other coating system (525 A-95 mm), which suggest a less ordered pyrochlore structure. This might be attributed to the different thermal history of the coating systems. The longer high temperature exposure time of the GZO coating (300 A-75 mm) can assist the atomic arrangements required for the ordered structure, while early failure of the other coating constrain it. Furthermore, tetragonal YSZ peaks originating from the YSZ layer were detected from the specimen of 525 A-95 mm system, as it failed through the YSZ/GZO ceramic interface.

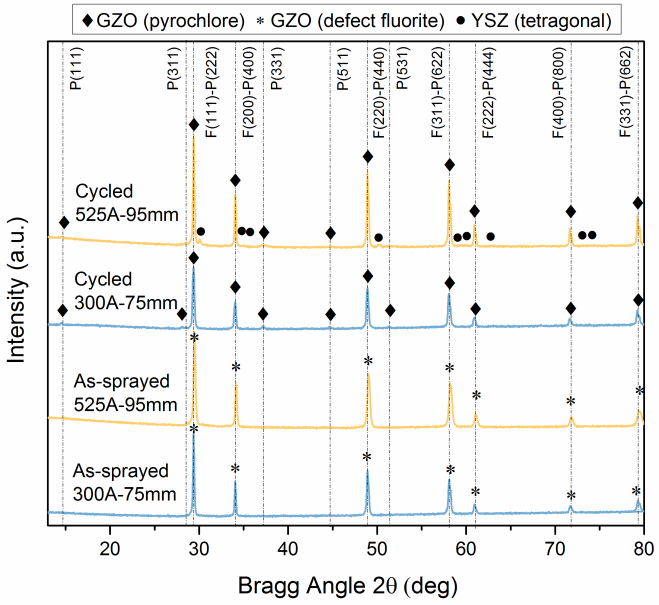

Figure 4.13: X-ray diffractograms taken from the GZO top surface of the thermally cycled specimens and the as-sprayed GZO coatings. The cycled specimens with the GZO sprayed with 300 A-75 mm and 525 A-95 mm current and stand-off distance, failed after 1627 and 50 cycles, respectively. The PDF numbers for the pyrochlore, defect fluorite and YSZ are; 01-075-8269, 01-080-0471 and 01-070-4427.

4.2 Detailed Relations of Microstructural Features and Lifetime of GZO

In order to separate the interference of gadolinia evaporation and low porosity on the early failures observed at high spray currents ($\geq$ 450 A), experimental plan was extended at this stage of the investigation. High porous GZO coatings (>18 %) were aimed to be achieved at 450 A and to be tested under the same thermal cycling conditions that employed in the previous section for a comparison. Because, if the evaporation has an influence on the lifetime, this should result in early failures regardless of high porous microstructure obtained at the high spray current.
In this second section, optimization of the stand-off distance at 450 A (using GZO 365 H powder) to achieve the high porosity by means of monitored in-flight particle temperatures will be presented. The impacts of the selected stand-off distances on the porosity, microstructure and chemical composition of the GZO coatings will be characterized. Furthermore, the modifications of the GZO microstructure by manipulating the spray parameters along with the general microstructural features of the coatings will be discussed via derivative analysis of the MIP data. Finally, the thermal cycling lifetime of YSZ/GZO double layers produced with the optimized spray parameters in this section will be evaluated.

4.2.1 Particle Temperature Measurements

Figure 4.14 shows in-flight particle temperature distributions of the GZO at a plasma current of 450 A and with the stand-off distances between 125 mm and 350 mm with 25 mm intervals. It is readily apparent that the particle temperatures drop with increasing stand-off distances as a result of longer time of flight of the particles outside the hot plasma zone. At the same time, the particle temperature distribution becomes narrower with greater stand-off distances. The wider temperature distributions are attributed in the literature to larger variation of melting among particles associated with the broader particle size distributions (Streibl *et al.*, 2006; Dwivedi *et al.*, 2015). Fine particles are heated up faster than coarser particles in the plasma plume which may contribute toward the broadening of the temperature distribution, as observed here at relatively shorter stand-off distances (from 125 mm to 225 mm). On the other hand, the particle temperature difference between the fine and coarser particles can become closer again at longer stand-off distances, as the temperature drop will be faster for the former than the later. This can explain the narrower temperature distributions beyond 225 mm.

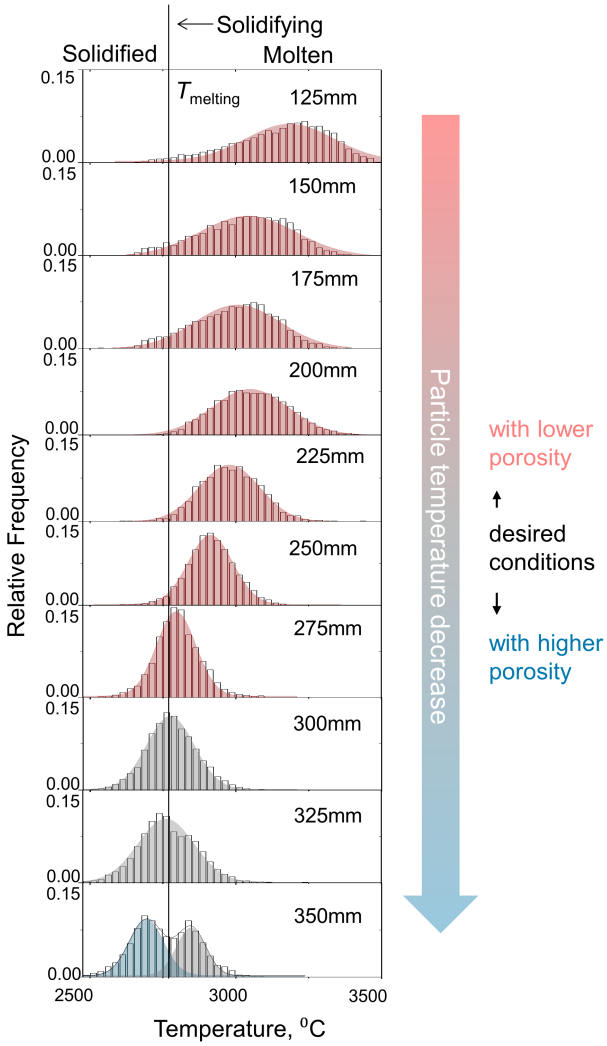

Figure 4.14: Particle temperature distributions as measured by two-colour pyrometry at 450 A with varied stand-off distances.

Similar to previous in-flight particle temperature evaluations (Figure 4.1), the distributions were fitted with Gaussian distributions. The peak temperatures (T) of the distributions were compared with the melting temperature (T_m) of the GZO and accordingly the characteristic peaks indicated in order to classify re-solidified ($T<T_m$), solidifying ($T\approx T_m$) and liquid particle ($T>T_m$) fractions. Based on these results, it can be seen that the majority of the particles are still liquid between stand-off distances of 125 mm

and 250 mm. The solidification occurs at the stand-off distances of 275 mm or greater, as the peak temperatures remain almost constant which is assumed to be associated with the release of fusion enthalpy. Finally with further particle temperature drops, a separate peak for the re-solidified particles is visible at 350 mm. With this approach, it can be estimated that the desired high porosity (>18%) might be achieved beyond a stand-off distance of 250 mm at 450 A. For that reason, it was decided to perform spraying experiments starting from a stand-off distance of 225 mm increasing up to 350 mm (Table 4.3). Furthermore, a low current-short stand-off distance (350 A-75 mm) spray parameter was added to the experimental plan for a comparison.

Table 4.3: Spray currents and stand-off distances selected to be tested for spraying of GZO.

Spray current (A)	Stand-off distance (mm)	Spray protocol
450	225	M-14-26-TP
450	250	M-14-27-TP
450	275	M-14-38-TP
450	300	M-14-42-TP
450	350	M-14-43-TP
350	75	M-14-62-TP

4.2.2 Porosity and Microstructure Analysis

The pore size distributions of the free-standing GZO coatings sprayed with varied spray parameters (Table 4.3) as determined by MIP are shown in Figure 4.15. For comparison, the porosity distribution of the GZO coating from previous results section (450 A-95 mm) was also added to the graph. The results show that the cumulative porosity of the coatings sprayed at 450 A changed from 11 to 20 % by volume. The porosity of the coatings sprayed between 250 mm and 300 mm are not significantly different from each other (12-15 %), but at 350 mm the porosity reaches 20 %. This can be due to higher amount of re-solidified particles in the microstructure as particle temperature measurements suggested. Moreover, the GZO coating sprayed at 350 A indicates a similar 20 % porosity content. However it is immediately visible that, although the two distribution curves approaches to 20 % cumulative pore volume, pore radius contributing to this porosity level is quite different in each case. The contribution of the pores with larger radius (>1 µm) to the cumulative porosity is almost 50 % by volume at 450 A, whereas it is in the range of 10 % at 350 A.

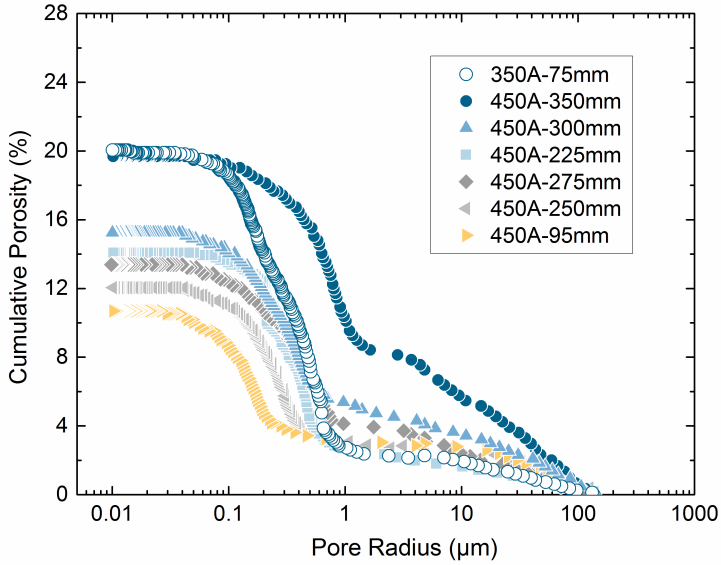

Figure 4.15: Cumulative pore size distributions of the GZO coatings sprayed at varied current and stand-off distances.

Typical porosity features in TBCs can be identified as; (i) interlamellar cracks formed due to imperfect adhesion of splats as a result of rapid solidification, (ii) intrasplat cracks, which are mostly perpendicular to the substrate and are formed by relaxation of quenching stresses, (iii) very fine pores formed around partially melted or unmelted particles, (iv) globular pores originating from gas entrapment and incomplete intersplat contact (Figure 4.16).

All of these features with different pore radius lead to typical bi-modal pore distributions (<1 µm, >1 µm) of the TBCs, which is also the case in the Figure 4.15. Commonly, the globular pores are classified as the larger pores of the distribution with a pore radius of > 1 µm, and the pores around unmelted particles, as well as intrasplat and interlamellar cracks, are classified as smaller pores with a pore radius of < 1 µm. According to the pore size distribution graph, the contribution of the large pores to the cumulative porosity increased with increasing stand-off distances. Based on this information, an increase in the numbers of globular pores can be expected at large stand-off distances, which can be observed in the SEM images of the coatings shown in Figure 4.17. The intrasplat cracks are observed at shorter stand-off distances (Figure 4.17 a-b), while interlamellar cracks and globular pores are noted at larger stand-off distances (Figure 4.17 c-e). Taking into consideration that the particle temperatures and velocities decrease while particle

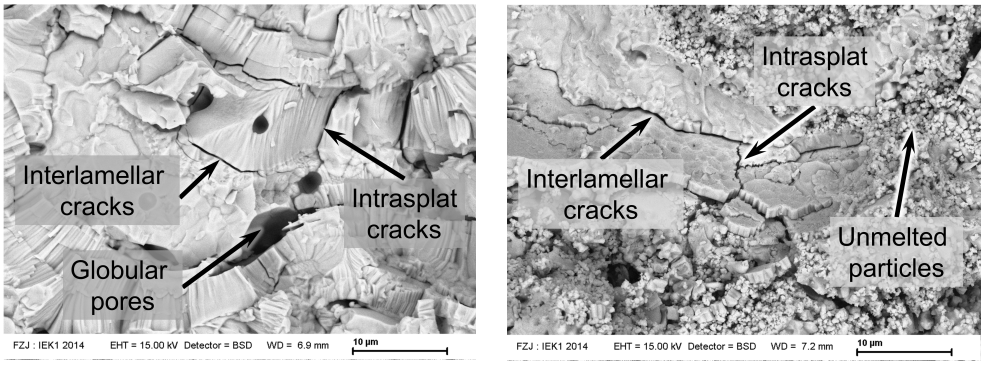

(a) (b)

Figure 4.16: Typical porosity features in plasma-sprayed TBC microstructures. Fracture surface SEM images of the coatings sprayed at 450 A-350 mm (a) and 350 A-75mm (b).

viscosity increases at greater stand-off distances, fewer quenching stress relaxation cracks, less splat spreading and hence poorer cohesion and packaging can be anticipated. The microstructure of the GZO coating sprayed at 350 A can be also seen in Figure 4.17f. Fine unmelted particles are seen in the microstructure, whereas almost no unmelted particles are visible at 450 A. Obviously, the particles reach the melting temperature of GZO at 450 A regardless of particle sizes, which is not the case at 350 A as discussed in the previous section.

It is important to specify these different features of the microstructures in order to interpret better their thermo-mechanical properties, lifetime performances etc. Thus, an approach for the identification of these features using MIP data will be discussed below.

Microstructural Feature Analysis from MIP Data

A different presentation was derived from MIP data in order to make the differences in the pore size distributions of the coatings due to changes in the microstructural features more readily visible. The derivative of the logarithmic pore size distribution function ($\Delta\phi \setminus \Delta(log_{10}(r))$ was plotted against the pore radius (r) with a logarithmically spaced abscissa as shown in Figure 4.18. By calculating the derivative of the pore size distribution function, the slope changes of the distribution which corresponds to a certain pore radius and hence a certain microstructural feature was aimed to display. The reason for taking the logarithmic derivative pore size distribution function was to find a correlation with the SEM images covering both small and large pore radii.

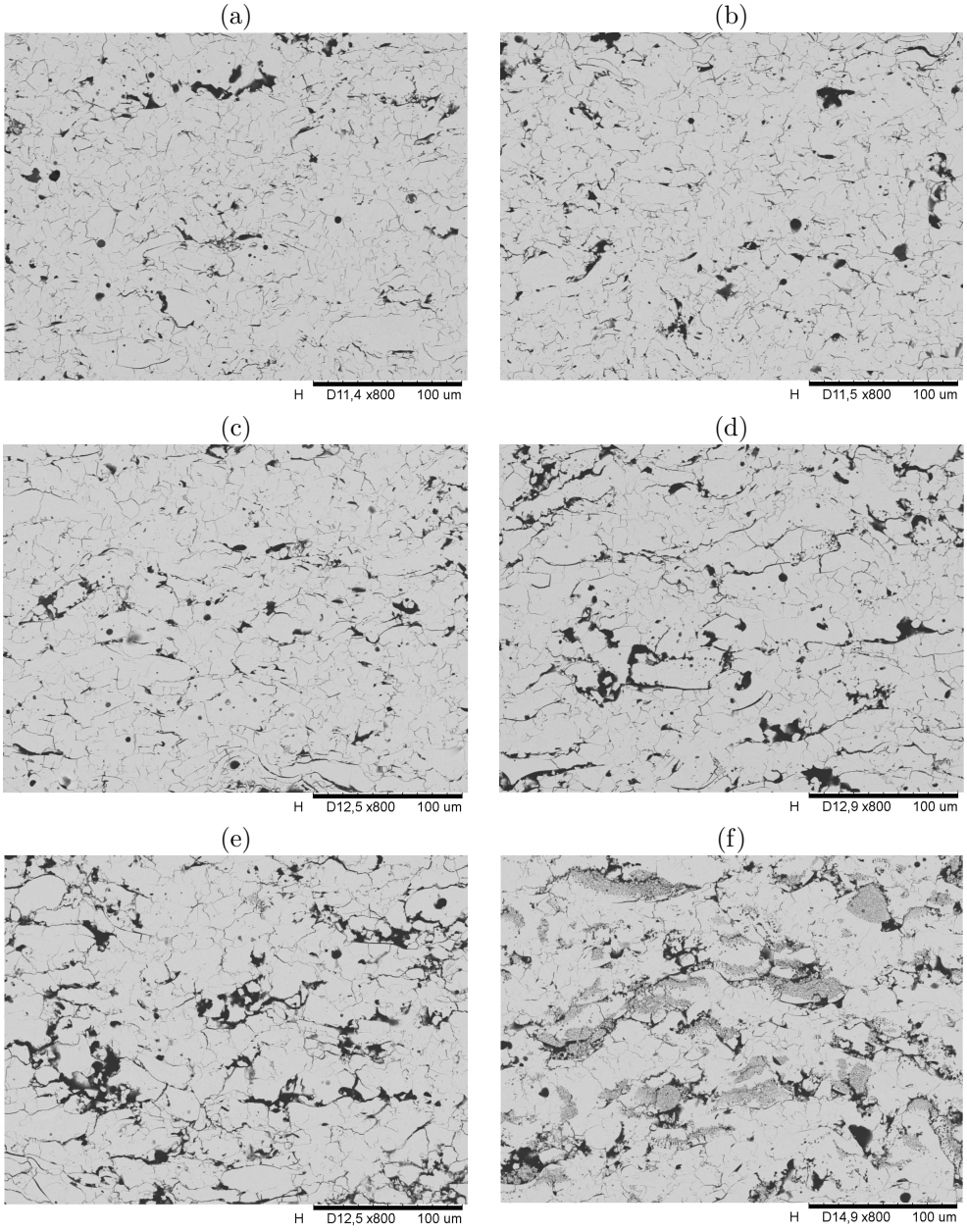

Figure 4.17: Microstructures of as-sprayed GZO coatings sprayed at 450 A with different stand-off distances; (a) 250 mm, (b) 275 mm, (c) 300 mm, (d) 325 mm, (e) 350 mm and (f) at 350 A with 75 mm stand-off distance.

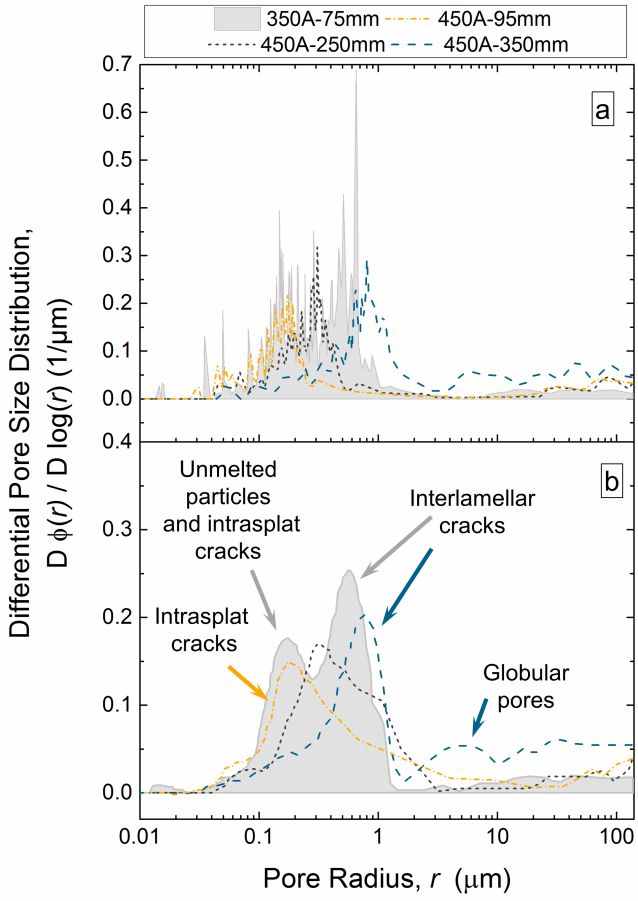

Figure 4.18: Differential pore size distributions of GZO coatings sprayed with 350 A-75 mm, 450 A-95 mm, 450 A-250 mm and 450 A-350 mm current spray distances; (a) logarithmic derivative of raw mercury intrusion porosimetry data and (b) after smoothing.

The contribution of the larger pores could not be represented with a linear derivative as it would approach zero. Furthermore, the data was smoothed in order to show peak positions more clearly, both raw and smoothed curves are given in Figure 4.18 for clarity. In the graph, the data of the GZO coatings sprayed at 450 A with 95 mm, 250 mm and 350 mm stand-off distances is shown as well as the coating sprayed at 350 A with 75 mm stand-off distance. It can be seen that the GZO coating sprayed at 350 A exhibits two peaks corresponding to a pore radius of 0.1-0.2 µm and 0.5-1 µm. Beyond 1 µm pore size, the differential pore size distribution of this coating is close to zero. On the other

hand, the coatings sprayed at 450 A at different stand-off distances typically show one maximum. Similar to the coating sprayed at 350 A, the distributions of the coatings sprayed at 450 A become close to zero beyond 1 µm pore radius, except for the layer sprayed at 350 mm stand-off distance. Observed peak positions of each coating provide information about their microstructural features. In the first place, a gradual shift of the peak position can be observed for the coatings sprayed at 450 A; from approximately 0.2 µm pore radius to 0.3 µm and then to 1 µm while extending the stand-off distance from 95 mm to 250 mm and 350 mm, respectively. This shift can be attributed to the replacement of fine intrasplat cracks detected at 95 mm with the relatively larger interlamellar cracks observed at 350 mm stand-off distance. Moreover, a comparison of the peak positions of the pore size distributions obtained at 350 A and 450 A reveals the essential differences of the corresponding microstructures. Fine unmelted particles of the GZO coating sprayed at 350 A are likely to be the reason for the first peak seen around the pore radius of 0.1 µm, which does not appear at 450 A. The two peaks located around 1 µm presumably originate from interlamellar cracks in both GZO coatings sprayed at 350 A and 450 A. Finally, the large globular pores clearly seen in the microstructure of the GZO layer sprayed at 450 A with a stand-off distance of 350 mm represent a considerable contribution of radii larger than 1 µm.

After all, this analysis enabled to get information about the porosity features of the different microstructures, which was not possible by means of a typical porosity distribution graph. Although, the interference of unmelted particles and intrasplat cracks could not be avoided, interlamellar cracks and globular pores could be separated from the crack network of the coatings with this method.

4.2.3 Crystallographic Evaluations

XRD analyses of the as-sprayed GZO coatings sprayed at 350 A and 450 A revealed that the coatings display a GZO defect-fluorite phase (Figure 4.19a). No characteristic pyrochlore reflections were detected in the diffractograms, similar to what was observed previously for the other as-sprayed GZO coatings. In order to see the effect of long stand-off distances at 450 A on the stoichiometry, lattice parameters of the coatings were derived from the X-ray diffractograms and are given also in Figure 4.19b.

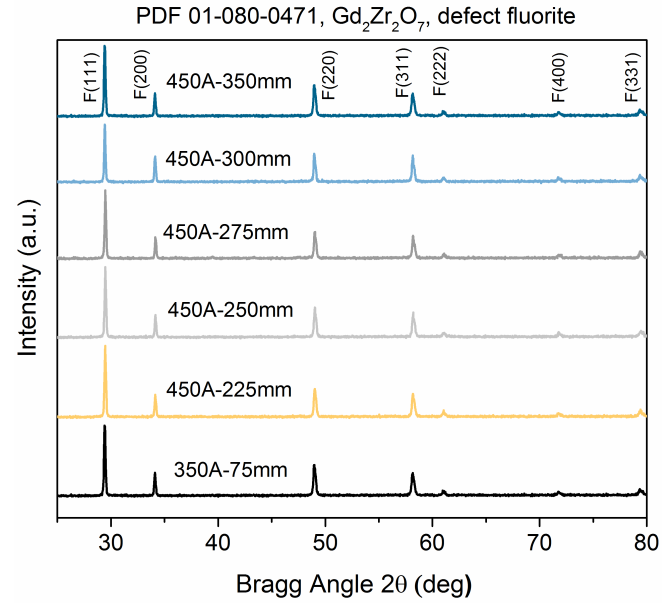

(a)

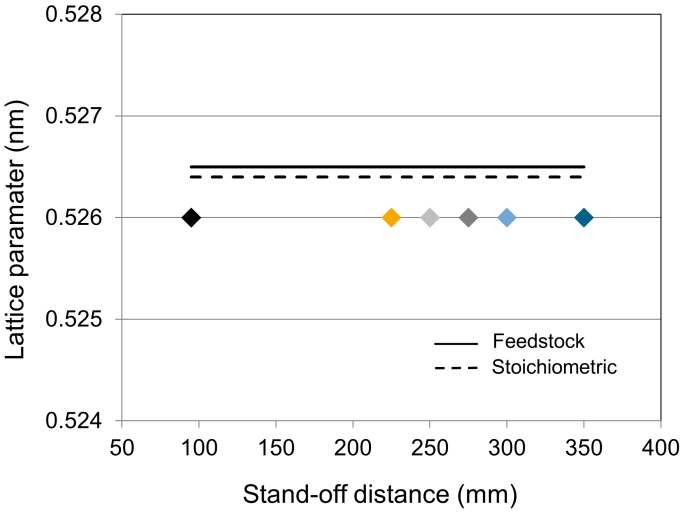

(b)

Figure 4.19: X-ray diffractograms of the as-sprayed GZO coatings sprayed at different current levels and stand-off distances (a), the lattice parameters of as-sprayed GZO coatings determined by Pawley´s method of refinement vs. stand-off distance (b). For a comparison, the lattice parameter of the coating sprayed at 450 A with 95 mm stand-off distance is also shown on the bottom graph.

In the graph, half of the value of the lattice parameter of the pyrochlore GZO feedstock is given for comparison. The slightly larger lattice parameter of the powder with respect to the lattice parameter of stoichiometric composition shows the small amount of excess gadolinia in the powder. The results also indicate no change in the lattice parameters of the coatings sprayed at 450 A with long stand-off distances. Obviously, the evaporation mainly occurs in the hot core of the plasma plume so that extended stand-off distances do not affect the total volume of vaporized gadolinia in the detectable limits.

4.2.4 Thermal Cycling Lifetime

The YSZ/GZO double layer TBCs (100 µm/400 µm thickness ratio) were manufactured for the assessment of the lifetime. The two spray parameters (350 A-75 mm and 450 A-350 mm), which produce the same cumulative 20 % porosity in different microstructures, were used to spray GZO layers while all the YSZ layers were sprayed with a 470 A current and 200 mm stand-off distance in these systems introducing a cumulative 12 % porosity. The monitored surface ($T_{\text{surf.}}$) and bond-coat temperatures (T_{BC}) as well as the number of cycles of the two tested specimens from each system in the burner rig tests can be found in Table 4.4. A comparison of their lifetime performances with the 450 A-95 mm system given in the previous section is shown in Figure 4.20.
Based on the results it can be concluded that:

i. The comparison of the two GZO layers sprayed at 450 A with short (95 mm) and long (350 mm) stand-off distances shows that the extended stand-off distance leads to an increase in porosity from 11 % to 20 %. No significant difference in the gadolinia content of the two coatings was found. Considering a lower gadolinia content of the coating sprayed at 450 A than that of 350 A based on the previous section and the good thermal cycling performance of the coating sprayed at 450 A-350 mm current and stand-off distance found in this section, the degree of gadolinia evaporation at 450 A apparently does not critically affect the lifetime. In other words, the GZO porosity governs the lifetime of double layers.

ii. Not only the porosity level of the GZO layer but also its microstructure considerably influences the lifetime of the double-layer systems. The GZO layers sprayed at 350 A-75 mm and 450 A-350 mm current and stand-off distances show the same cumulative porosity level, but different microstructures reveal dissimilar lifetime performances.

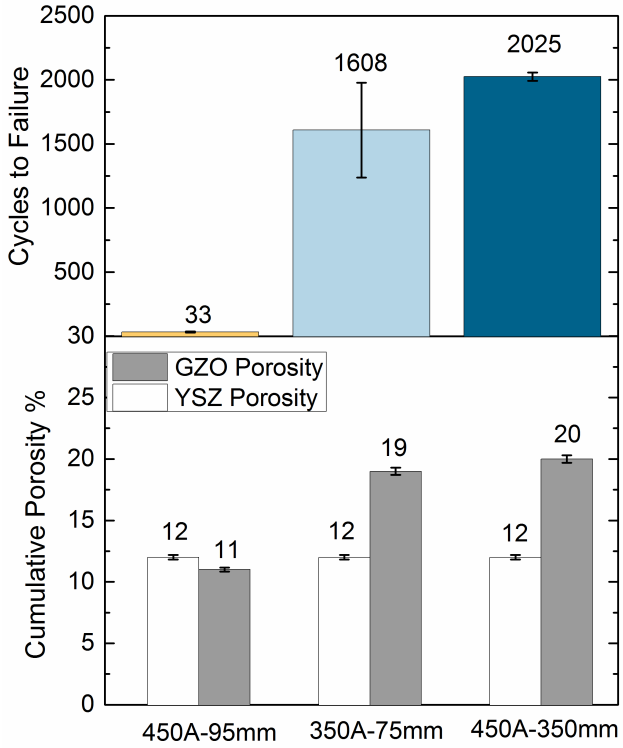

Figure 4.20: Influence of the porosity and microstructure of the GZO layer on the lifetime performance of YSZ/GZO double layers. Burner rig test results of double-layer TBCs tested at 1400 °C surface temperature are plotted in the upper graph. The error bars on the lifetime plot bars show the max. and min. number of cycles of two tested specimens. The number of cycles indicated at the top of the bars is the average cycle number. Cumulative porosities of the GZO and YSZ layers in double-layer systems are also shown in the bottom graph. Lifetime and porosity data for 450 A-95 mm spray conditions are taken from a previous section for comparison.

The failure modes of the two thermally cycled coatings can be seen in the cross-section SEM images in Figure 4.21. It can be observed that in addition to the extreme difference in the lifetime for 450 A-350 mm system compared to 450 A-95 mm, a change in the failure is recorded. The failure mode changed from YSZ-GZO interface delamination due to the crack growth in the YSZ layer to TGO growth-induced failure with increasing GZO porosity.

Table 4.4: Recorded surface ($T_{\text{surf.}}$) and bond-coat temperatures (T_{BC}) as well as lifetime cycles of two tested specimens for each set of spray parameters.

Coating systems and internal specimen codes	$T_{\text{surf.}}$ **(°C)**		T_{BC}**(°C)**		**Lifetime (number of cycles)**	
	1st	**2nd**	**1st**	**2nd**	**1st**	**2nd**
GZO (350 A-75 mm)/YSZ (WDS 3041&3042)	1397	1391	1073	1060	1238	1979
GZO (450 A-350 mm)/YSZ (WDS 3043&3044)	1394	1392	1066	1064	1988	2055

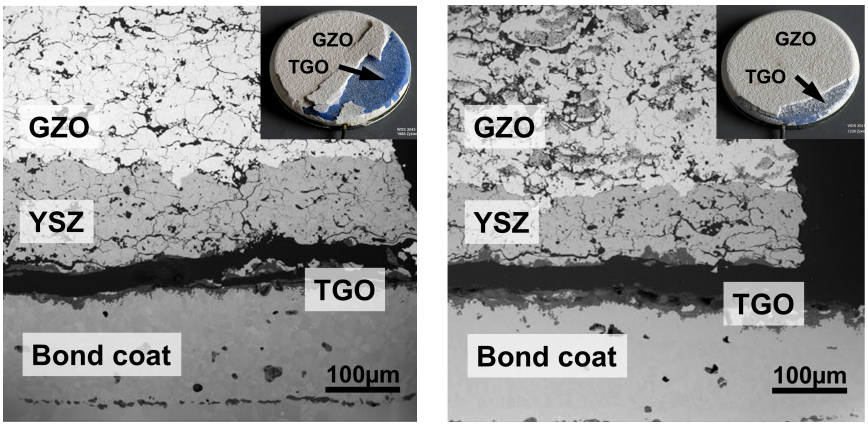

(a) (b)

Figure 4.21: Cross-section microstructures showing the failure modes of thermally cycled GZO/YSZ coatings. GZO layers in the systems were sprayed at (a) 450 A-350 mm (WDS 3043), (b) 350 A-75 mm (WDS 3041) current and stand-off distances.

The elimination of the potential effect of gadolinia evaporation on the lifetime of the coating sprayed at 450 A favours the interpretation that the early failure observed at 95 mm was induced by low porosity levels. Likely, the high Young´s modulus of the low porous as-sprayed GZO coating, which is enhanced at high temperatures due to sintering, caused the early failures. On the other hand, the different performance of the 450 A-350 mm system than the 350 A-75 mm also suggests dissimilar properties of the GZO microstructures sprayed with these parameters, despite their same total porosity level. Thus, to get a better understanding on the performance of these GZO layers, the thermomechanical properties of them will be discussed in Chapter 5.

5 | Results and Discussion Part 2: Thermophysical and Thermomechanical Properties

The purpose of this chapter is to describe thermophysical and thermomechanical properties of the GZO and YSZ coatings which affect the coating failure driving force and resistance. A low thermal conductivity and a high coefficient of thermal expansion (CTE) are essential properties required for a ceramic TBC layer as introduced before. However, although the data of the CTE and the thermal conductivity belong to GZO is available in the literature, they are mostly obtained from the sintered powder compacts. Thus, these properties of the as-sprayed GZO coatings were measured and compared with the literature in this chapter.

Furthermore, ceramic coating sintering and creep are among the most important issues for the development of advanced TBCs, as their effects are known to be profound and detrimental to coating performance (Eaton and Novak, 1987; Soltani *et al.*, 2007). Not only can sintering and creep result in microstructural changes and compaction of the coating, entailing considerable elastic modulus increases, but also can cause spallation. Thereby, the critical issues such as sintering, creep and elastic modulus of the GZO coating and their relevance to lifetime will be addressed here.

5.1 CTE and Thermal Conductivity of Plasma-Sprayed GZO Coatings

The CTE of a GZO coating sprayed with 325 A-75 mm spray current and stand-off distance yielding 18 % total porosity volume was measured from expansion rate in a thermomechanical analysis (TMA) facility. Figure 5.1 shows a comparison of the acquired data with the literature. Firstly, the results reveal that the CTE of the GZO is comparable to that of plasma sprayed 8YSZ ($10.7 \times 10^{-6}\,\mathrm{K}^{-1}$, 293-1273 K, Cao *et al.* (2004)).

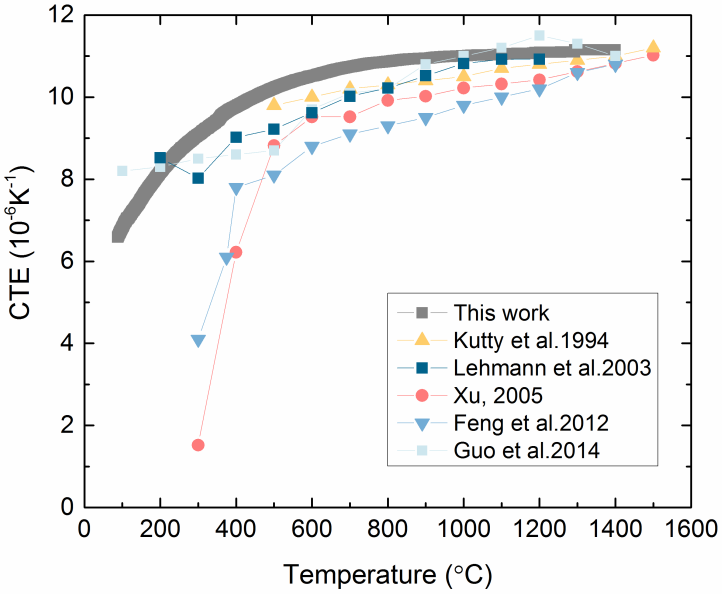

Figure 5.1: Comparison of the CTEs of the GZO compiled from the literature and this work.

Secondly, it should be clarified that the literature data given on the plot are either calculated theoretically for a GZO pyrochlore crystal structure (Feng *et al.*, 2012) or measured from sintered GZO specimens via different methods such as high-temperature X-ray diffractometry (Kutty *et al.*, 1994) or dilatometry (Lehmann *et al.*, 2003; Guo *et al.*, 2014). In this respect, apart from the differences introduced by the different measurement techniques, variations in the CTE measurement results can be anticipated due to different crystallographic order-disorder degree of the as-sprayed and sintered specimens. Because, the CTE of the materials is directly related to their crystal structure and atomic bonding. It was reported in the literature that the bonding strength in the $A_2B_2O_7$ structure is correlated to the variation of crystallographic 48f oxygen x position, which lies between 0.3125 and 0.375 and describes the A-O/B-O distances (Subramanian *et al.*, 1983; Kutty *et al.*, 1994). The Madelung binding energy of the structure decreases with the increase in the x parameter, which indicates a disordered pyrochlore structure, leading to an increase in the CTE of the material (Pannetier, 1973; Radhakrishnan *et al.*, 2011).

The initial porosity content of the as-sprayed coating and sintered specimens can be also expected to be different. However, generally, there is no certain thermal expansion-porosity relationship that can be applied to all porous materials. Moreover, CTE of the

different sintered or plasma sprayed ceramic materials were already reported as independent of porosity in the literature (Coble and Kingery, 1956; Nakamichi *et al.*, 1998). Thermally-induced relaxation of a bond or the lattice constant of a material is known as leading to an increase in the CTE of the material at elevated temperatures, which is also observed in Figure 5.1. Calculations of Feng *et al.* (2012) suggest that the temperature dependence of CTE follows closely the specific heat of Debye approximation and the CTE is increased linearly by increasing the temperature at the temperatures higher than the Debye temperature, i.e. 600 K. This shows a rather good agreement with the measurements of the CTE of the sintered GZO pellets with an ordered structure. But the increase rate of the CTE at elevated temperatures is relatively small for the as-sprayed GZO coating with a disordered pyrochlore (or defect fluorite) structure. Furthermore, a slightly higher CTE of the as-sprayed coating is recognized particularly at lower temperatures than 1000 °C. This can be due to the fact that the ordering degree of the as-sprayed coating is increased during dilatometric measurement. The lower binding energy of disordered structure can be the reason of observed higher CTE at lower temperatures, while a relatively ordered structure at elevated temperatures can explain the concurrence of the results.

The thermal diffusivity of the two GZO coatings and a YSZ coating, sprayed with 325 A-75 mm, 325 A-95 mm and 420 A-200 mm current and stand-off distances which displayed 18, 25, and 18 % total porosity volume, respectively, was measured via laser-flash technique. Figure 5.2 shows the the calculated thermal conductivity of these three coatings using the measured thermal diffusivity, the specific heat and density of the coatings. Some other literature data are also given for comparison on the plot. The comparison of the results obtained from the coatings in this work reveals a ∼25 % lower thermal conductivity of the GZO than that of the YSZ at the same (18 %) porosity level over the measurement temperature range. On the other hand, no significant reduction was recorded in the thermal conductivity of GZO coating with further porosity increase up to 25 %.

As the rest of the data taken from the literature indicating the measured thermal conductivity of the sintered compact YSZ or GZO powder, the initial porosity volume of these specimens are expected to be significantly lower than those of the coatings. Correspondingly, a lower thermal conductivity of the sprayed coatings with lamellar and cracked microstructure and higher porosity than that of the pressed powder specimens is clearly seen on the graph regardless of the material.

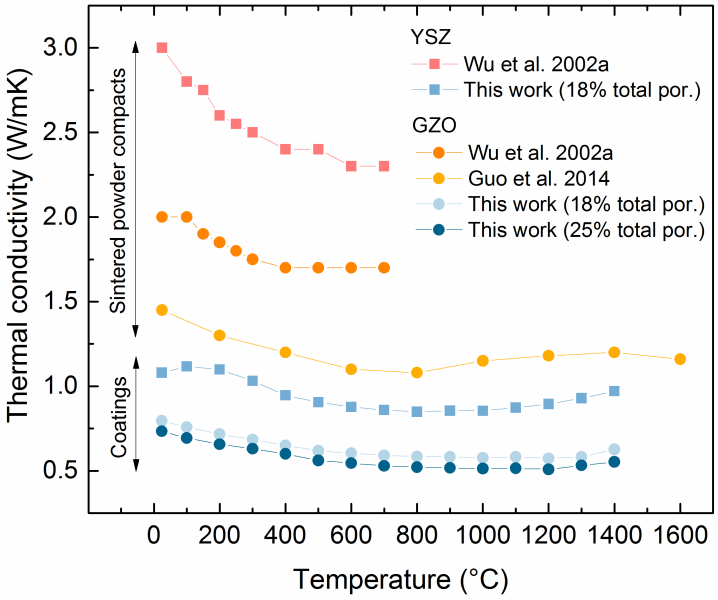

Figure 5.2: Comparison of the measured thermal conductivity of the GZO coatings and sintered powder compacts via laser flash technique compiled from the literature and this work.

It is also worth repeating here that the thermal conductivity of GZO pyrochlore and fluorite were reported as very similar up to 700 °C by Wu *et al.* (2002a). Moreover, a lower thermal conductivity of the GZO (from ∼30% to ∼50%) than that of the YSZ is also obvious in the sintered specimen group. The lower thermal conductivity of the GZO is mainly attributed to the (i) higher concentration of oxygen vacancies present in the GZO and (ii) the more effective phonon scattering by solute Gd cations as a result of the significant atomic-weight difference between Gd and Zr, as introduced before.

A typical decrease is observed in the thermal conductivity of all specimens up to ∼800 °C which can be assigned to enhanced phonon scattering with increasing temperatures. With a further temperature increase, a slight thermal conductivity increase is recorded and can be attributed to the increased contribution of the radiative component of heat conduction, also known as photon thermal conductivity (Wu *et al.*, 2002a; Somiya, 2012; Guo *et al.*, 2014). This monitored temperature dependence of measured thermal conductivity is consistent with similar observations made on porous zirconia coatings and dense sintered pyrochlore ceramics in the literature (Zhu and Miller, 2004; Jang and Matsubara, 2006; Fabrichnaya *et al.*, 2015).

5.2 Elastic Behavior and Creep Processes in Plasma-Sprayed YSZ and GZO Coatings

The elastic response and creep behavior of as-sprayed free-standing GZO and YSZ coatings were investigated in the TMA facility with the three-point bending setup. The measurements were performed applying varied low loads (5, 10, 15, 20 g) on the as-sprayed and annealed coatings (1400 °C-200 h) at room temperature (RT) and during annealing from RT to 1400 °C to monitor temperature-dependent properties. Furthermore, load-duration and time-dependent evolution of the properties of the as-sprayed and annealed coatings were investigated. The elasticity and viscosity data of the coatings will be presented as function of temperature, load duration and time below.

5.2.1 Temperature Dependent Young´s Modulus and Viscosity

The elastic modulus and viscosity of the as-sprayed YSZ (420 A-200 mm, ∼18 % total porosity) and GZO (325 A-75 mm, ∼18 % total porosity) as well as annealed (1400 °C-200 h) coatings were investigated as a function of temperature with a constant load duration of one minute. Figure 5.3 shows the cross-section microstructure comparison of the as-sprayed and annealed coatings. The as-sprayed YSZ coating exhibits a splat-like microstructure composed of overlapped lamellae separated by interlamellar cracks and embedded in a network of microcracks and voids (Figure 5.3a), while the heat treatment leads to the partial sintering of the porous microstructure (Figure 5.3a1). Sintering necks are formed at the boundary of the splats improving the interlamellar bonding along with the closure of microcracks and pores. The fine intrasplat cracks disappear, while the large pores are influenced by densification at lesser extent. Similar to the YSZ coating, as-sprayed GZO microstructure consists a network of inter-intrasplat cracks and voids but the main difference is the presence of the unmelted particles (Figure 5.3b). The densification of the GZO coating can be also observed after the heat treatment although the difference is not as clear as the YSZ coating. Obviously, the fine cracks are closed and disappear, however the unmelted particles with a certain growth and voids among them are still present in the microstructure (Figure 5.3b1). By no means they lead to a full densification despite their high specific surface area and curvature that are expected to favor sintering activity. As discussed before, the larger pores observed in the microstructure of the coatings consisted of unmelted particles are assumed to be formed pullouts during polishing. Because the unmelted particles are preserved after heat treatment, the large pores settled around them can be attributed to the same artifact.

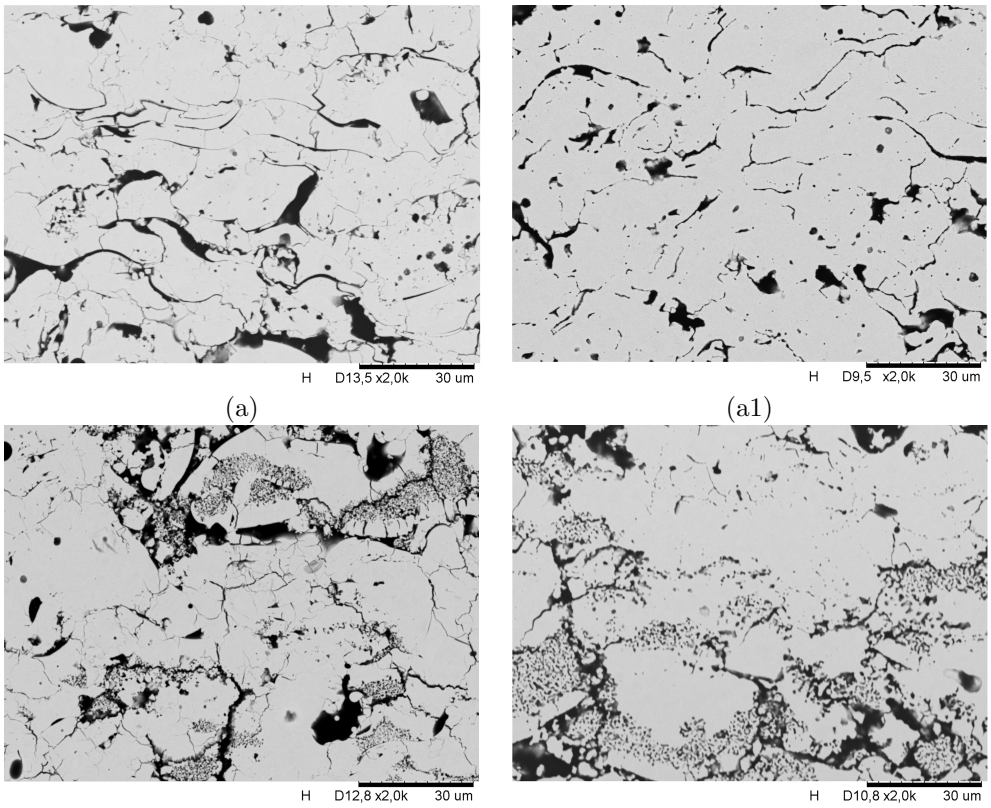

Figure 5.3: Cross-section SEM micrographs of as-sprayed (a,b) and annealed (1400 °C-200 h) (a1, b1) YSZ and GZO coatings, respectively.

Figure 5.4 shows the temperature dependent pure elastic modulus (K_1 in the Burgers Model) of the as-sprayed YSZ and GZO coatings. A difficulty in determining the elastic modulus of the plasma sprayed coatings is obtaining a pure elastic deformation due to splat sliding and/or propagation of cracks and pores. Thus, in order to rule out the effect of these on the results during the loading period, the displacement after load release was used to calculate Young´s modulus. The tests for the as-sprayed coatings were performed two times in a row from RT to 1400 °C, which are referred to be the first and second cycles on the graph.

The 1st cycle measurements of the both as-sprayed GZO and YSZ coatings yield almost a constant elastic modulus profile at ∼5 GPa and ∼16.5 GPa, respectively, up to 800 °C. The variation in the applied tensile or compressive loads, deformation volumes as well

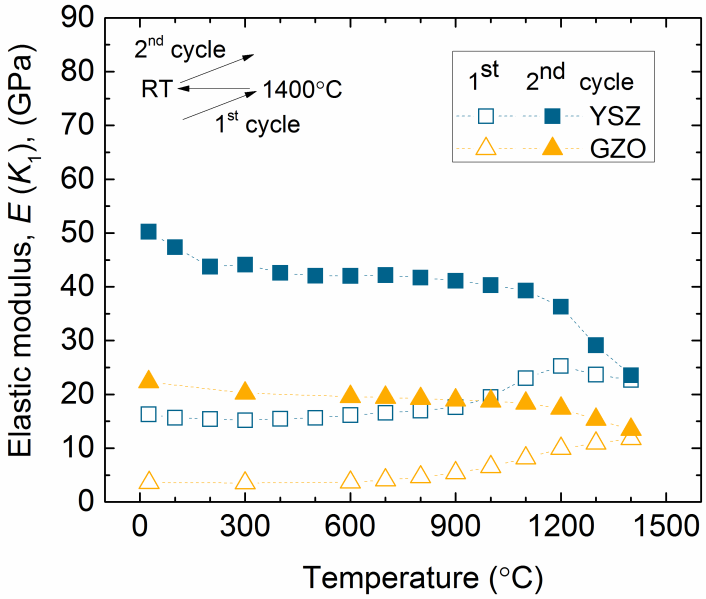

Figure 5.4: Temperature-dependent elastic moduli of the as-sprayed YSZ and GZO coatings.

as in-plane or out-of plane measurement directions of individual test techniques were reported to be significantly effective in the modulus of the plasma sprayed coatings (Kim and Kweon, 1999; Ahrens *et al.*, 2004; Choi *et al.*, 2008). Nevertheless, a comparison of the elastic modulus of the as-sprayed YSZ coatings determined by three-point bending test in the literature shows a good agreement with the results reported here. Kim and Kweon (1999) and Ahrens *et al.* (2004) measured an elastic modulus of ∼21 GPa and ∼17 GPa for the 12 % and 16 % porous plasma-sprayed YSZ coatings, respectively. The obtained elastic modulus of the as-sprayed coatings via bending tests are an order of magnitude lower than bulk modulus of the YSZ (210 GPa, Vaßen *et al.* (2000)) determined by indentation technique. Apart from the influence of the measurement technique, this difference can be attributed to the effect of splat-like porous microstructure on the elastic modulus, where the interlamellar cracks may enable a relative motion and bending of the splats.

According to the current literature search, there is no study, yet, reporting the elastic modulus of the plasma-sprayed GZO coatings, although the bulk modulus of the GZO was measured to be 200 GPa by Zhang and Zhao (2013) via indentation technique, which is very close to that of the YSZ (210 GPa). However, higher melting temperature of the

YSZ than the GZO suggests stronger binding energy in the former, which requires higher forces to separate the atoms, and thus the higher modulus of elasticity. According to the measurements performed here on the as-sprayed coatings, the elastic modulus of 18 % porous GZO coating is found to be four-fold lower than the same porous YSZ coating. There is certainly a contribution of the different microstructural features of the YSZ and GZO coatings on the observed moduli, however it is not possible to interpret it with the available research data.

An increase in the modulus of the GZO coating and an increase followed by a decrease in the modulus of the YSZ coating was recorded above temperatures of 800 °C in the 1st cycle. In the 2nd cycle, on the other hand, in addition to an about four-fold increase in the RT modulus of the coatings, a gradual reduction in the moduli with increasing temperatures is observed becoming more pronounced above 800 °C. The monitored stiffness increase of the coatings in the 1st cycle can be related to enhanced sintering at higher temperatures. Similarly, noted higher moduli of the coatings in the 2nd cycle can be associated with their recorded thermal history and sintering during the 1st cycle.

The reduction in the elastic modulus of polycrystalline ceramic materials at elevated temperatures are attributed to different phenomena. The increased thermal vibrations and relaxed atomic bindings at high temperatures lead to a decrease in the elastic modulus, however, the non-elastic effects such as grain boundary sliding and grain boundary softening were indicated to be more effective on the decrease of the modulus (Rice, 2000; Carter and Norton, 2013). Furthermore, the increased ordering of the GZO pyrochlore phase or phase separations of t' phase of the YSZ into the equilibrium phases of monoclinic and cubic phase above 1200 °C may also have an effect on the modulus of the coatings.

After a 200 h heat treatment at 1400 °C (Figure 5.5), the RT elastic modulus of the GZO coating shows almost an order of magnitude increase (from ∼5 GPa to ∼47 GPa) compared to the RT modulus of the as-sprayed coating measured in the 1st cycle. With the temperature increase, a progressive decrease in the modulus of the annealed coating is observed approaching to ∼30 GPa at 1400 °C. The temperature-dependent evolution of the modulus of annealed GZO coating is similar to one noted in the 2nd cycle of as-sprayed coating except to shift towards higher values of modulus. For the annealed YSZ coating, on the other hand, a strong temperature-dependent behavior of the elastic modulus is noted varying in between 75 and 50 GPa. The secondary phases introduced by phase separations of t' phase as mentioned above, which are reported to have different modulus of elasticity (Zhao *et al.*, 2011), might be the reason of the observed fluctuations.

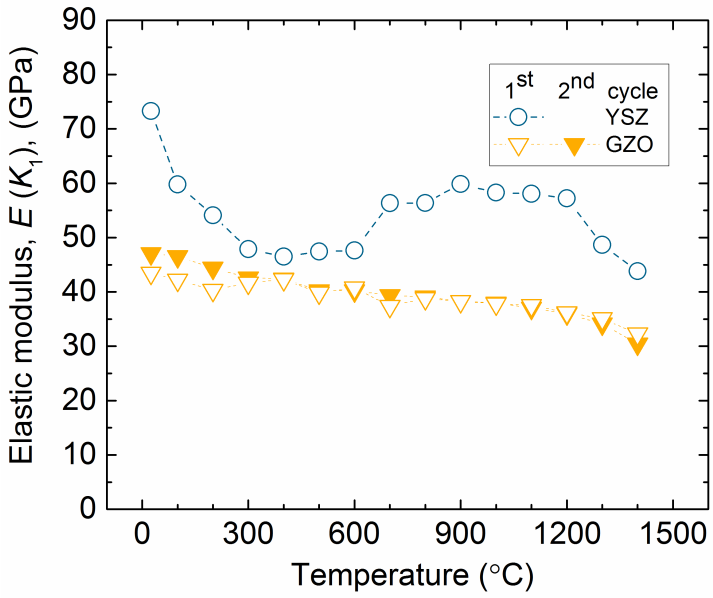

Figure 5.5: Temperature-dependent elastic moduli of the annealed (1400 ˚C-200 h) YSZ and GZO coatings.

Figure 5.6 shows the calculated viscosity of the YSZ and GZO coatings as a function of temperature. Considering the 1st cycle measurements of the both coatings, from RT to ∼800 ˚C and from 800 ˚C to 1400 ˚C, two different trends are observed. In the RT-800 ˚C range, a decrease in the viscosity up to 300 ˚C is recorded which starts to increase afterward. Above 800 ˚C, the viscosity is linearly decreasing up to 1400 ˚C.

One of the earliest work (Firestone *et al.*, 1982) in the literature indicated that the time-dependent strain increase of the plasma-sprayed coatings under a constant load (creep) is a thermally-activated process, with the splat-sliding being an important creep deformation mechanism. More recent work reported that the ceramic thermal barrier coatings can creep significantly under compressive stress states at relatively low temperatures (Zhu and Miller, 1998a; Rejda *et al.*, 1999; Ahrens *et al.*, 2004). Zhu and Miller (1998b) proposed a mechanism-based model to describe the densification and deformation occurring in thermal barrier coatings taking into account a stress induced mechanical sliding mechanism as well as a temperature and stress enhanced cation diffusion through the splat and grain boundaries.

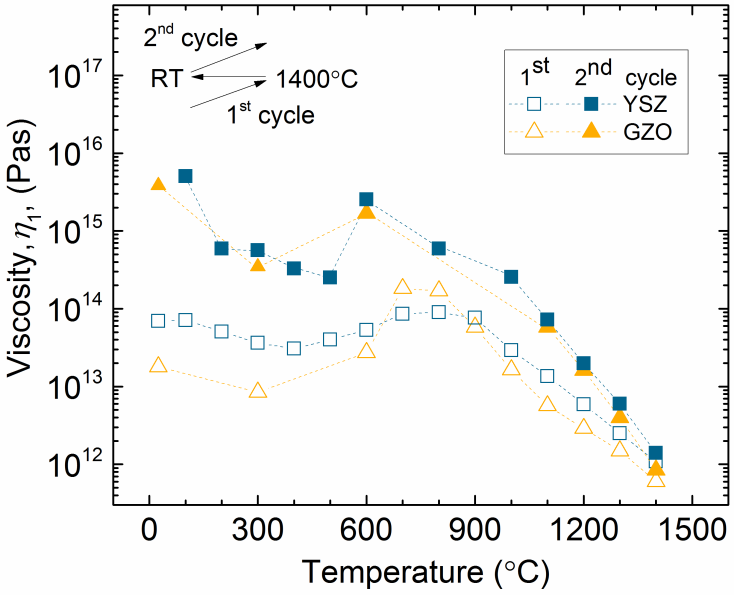

Figure 5.6: Temperature-dependent viscosity of the as-sprayed YSZ and GZO coatings.

In agreement with the literature, the noted changes in the behavior of the as-sprayed YSZ and GZO coatings in the relatively lower and higher temperature ranges (Figure 5.6) suggests different creep mechanisms. The mechanical sliding process between the splats can explain the creep observed even at RT. Based on that, the different friction forces present in the splat-splat and splat-unmelted particle interactions of the YSZ and GZO coatings, respectively, can be related to differences in the RT temperature viscosity of the coatings. It is rather complicated to explain the monitored behavior up to 900 °C and it is not fully understood. One reason leading of an increase in the viscosity of the system above 300 °C can be the formed sintering necks limiting the motion of the splats. On the other hand, linearly decreasing viscosity above 900 °C clearly indicates a thermally-activated mechanism. Presumably, the assistance of the diffusion processes to the mechanical sliding mechanism becomes more pronounced in these elevated temperature range. Nevertheless, no significant difference in the viscosity of the YSZ and GZO coatings were observed. The 2nd cycle viscosity measurement results of the coatings are also shown in the graph (Figure 5.6) showing similar behaviors along with a general shift to the higher viscosity values.

Considering that the temperature dependence of the viscosity is a thermally activated process, creep activation energies of the as-sprayed and annealed GZO coatings were

calculated by utilizing the natural logarithm of the Arrhenius equation i.e. (Green, 1998);

$$ln(\eta) = ln(\eta_0) + \left(-\frac{Q}{R}\right) \cdot \left(\frac{1}{T}\right) \tag{5.1}$$

where Q is the activation energy for viscous flow, η_0 is a constant, R is the gas constant and T is the absolute temperature. Figure 5.7 shows the Arrhenius plot and calculated activation energies of the coatings in the temperature range of 900-1400 °C.

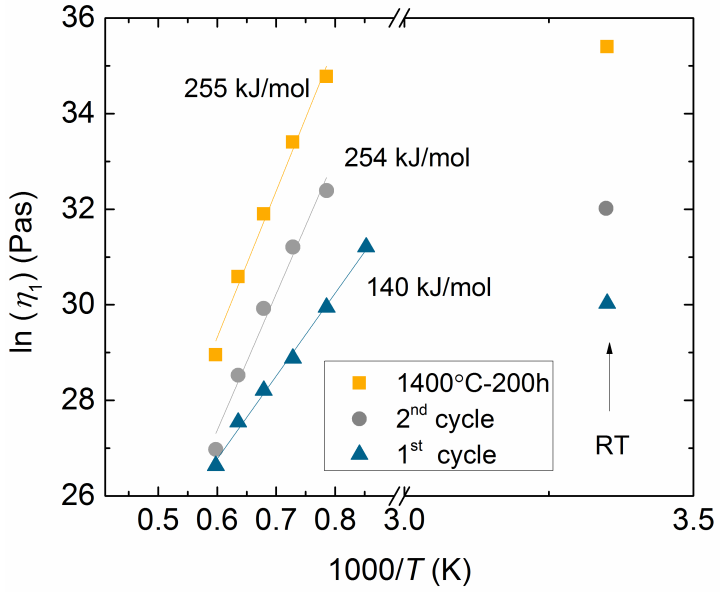

Figure 5.7: Comparison of the viscosity data of an as-sprayed and annealed (1400 °C-200 h) GZO coating as a function of inverse temperature.

The RT measurement result of each coating is also indicated on the graph which explicitly suggest a different creep mechanism at RT. Furthermore, the creep activation energy of the as-sprayed coating in the 1st cycle (140 kJ/mol) is found be lower than that of the same coating in the 2nd cycle (254 kJ/mol) as well as the annealed GZO coating (255 kJ/mol). Interestingly, this implies a faster creep of the as-sprayed coating in the 1st cycle even compared to 2nd cycle as well as to the annealed coating. This can be related to the reduced contribution of the mechanical sliding to the diffusion at elevated temperatures due to densification particularly in the annealed coating. On the other hand, it can be attributed to differences in the diffusion activation energies of the ions

in the GZO crystal structures with different degree of ordering. It is consistent with the experimental study that the ordering degree of an as-sprayed GZO coating is lower than a coating which was exposed to 1400 °C. Thus, it can be assumed that after the 1st cycle measurement or after annealing the ordering degree of the coating is increased. In the literature, different studies show an agreement on the worse ionic transport properties of the ordered pyrochlore structure with lack of defects compared to a disordered structure (Wilde and Catlow, 1998b; Wuensch *et al.*, 2000; Guillén *et al.*, 2008). Thus, a better sintering/creep resistance can be expected in the ordered pyrochlores as a result of their limited ionic transport properties.

5.2.2 Elastic Modulus and Viscosity as a Function of Load Duration

The time dependent elastic and viscous response of the as-sprayed YSZ (18 % por.) and GZO (20 % por.) coatings were investigated at RT as a function of load durations (1, 2, 3, 4, 5, 10, 15 min). Figure 5.8 shows recorded displacement of a coating as an example under cycling loading with different loads and load durations. The measured Young´s modulus and viscosity of the YSZ and GZO coatings in these experiments are given in Figure 5.9.

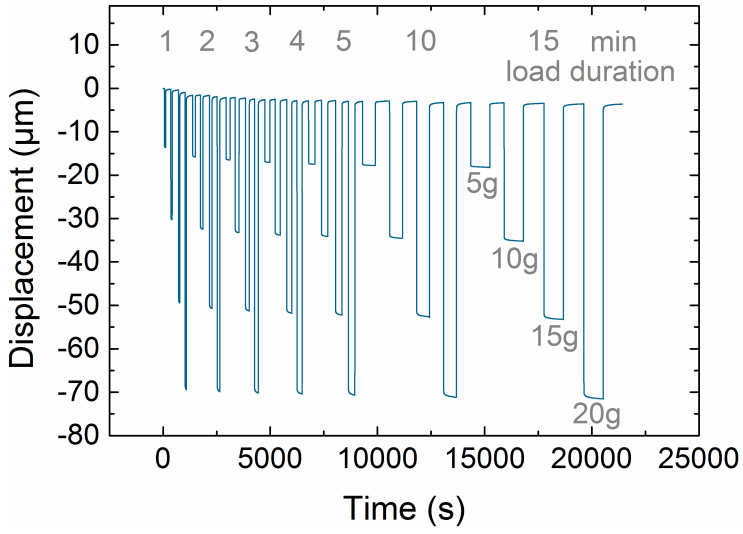

Figure 5.8: Time-dependent displacement of a coating during cyclic loading at room temperature with varied load durations and loads.

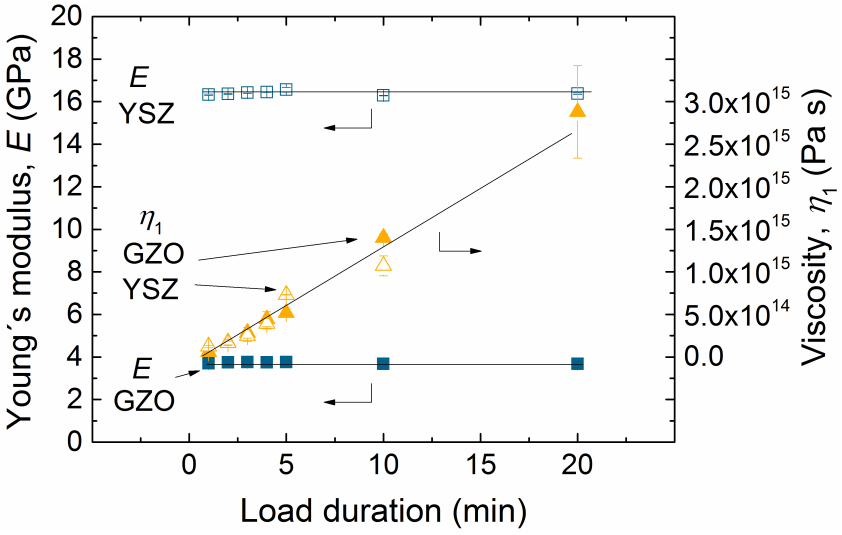

Figure 5.9: The measured Young´s modulus and viscosity of the as-sprayed YSZ and GZO coatings as a function load duration.

The Young´s modulus of the YSZ and GZO coatings are found to be independent from the load duration at room temperature and recorded as 16.5 GPa and 4 GPa, respectively. On the other hand, a linear relationship of the viscosity and the load duration is observed for both materials. As discussed previously, the time-dependent strain increase of the as-sprayed coatings under a constant load at RT is related to the stress induced splat sliding, which is governed by not the material inherent properties but the splat geometry. The sliding of the mechanically bound splats until becoming locked in place by neighboring splats, which leads to a strain hardening effect in the coating, thus, can be related to the observed increase in the viscosity of the coatings at longer load durations.

The effect of the load duration on the viscosity of the YSZ and GZO coatings was also investigated at 1400 °C under a constant load of 10 g. Figure 5.10a-b show the monitored displacement of a coating and the measured viscosity at these high temperature experiments compared to the room temperature measurements, respectively.

The results reveal that the effect of load duration becomes less predominant at the elevated temperature suggesting a modification in the creep mechanism of the mechanical splat sliding. A diffusion driven creep mechanism at elevated temperatures, as already shown by Arrhenius dependency of the data previously, becomes evident with these findings.

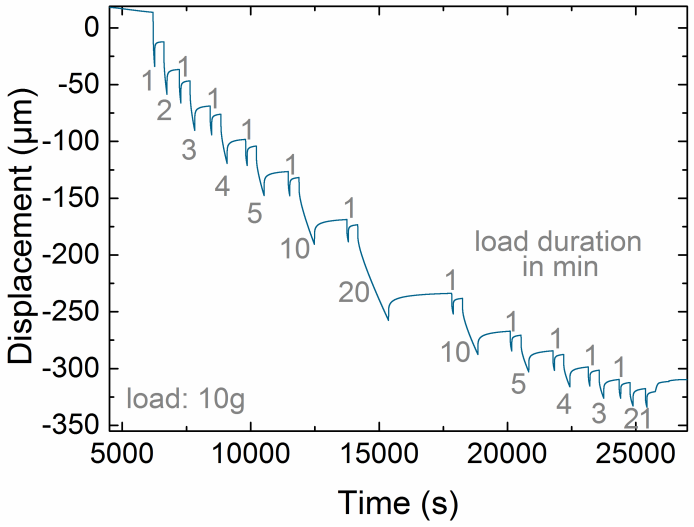

(a)

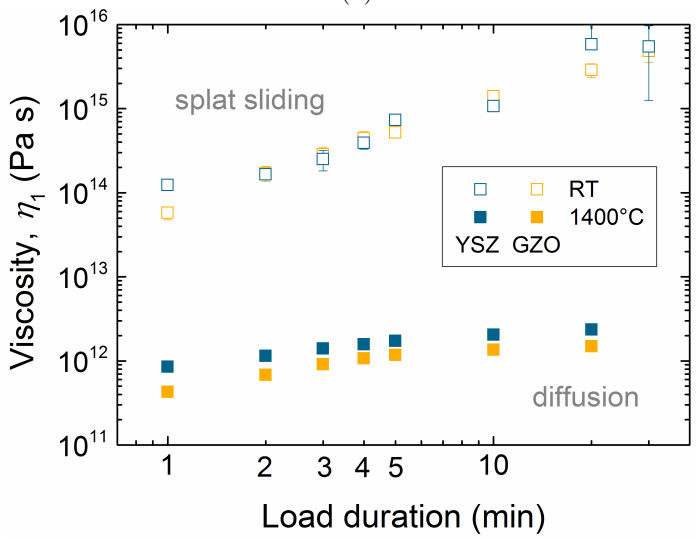

(b)

Figure 5.10: Recorded displacement of a coating during cyclic loading under 10 g load at 1400 °C with varied load durations (a), comparison of the measured viscosity of the as-sprayed YSZ and GZO coatings at room temperature (RT) and at 1400 °C as a function load duration (b).

Furthermore, considering also the differences in the microstructures of the YSZ and GZO coatings, no significant difference in the high temperature creep behavior of the

as-sprayed YSZ and the GZO coatings is observed in these experiments similar to the RT measurements. However, as discussed previously, there is a significant difference between the high temperature creep behavior of disordered (as-sprayed) and ordered (after exposed to 1400 °C) GZO coatings. Therefore, further experiments are needed to compare and understand high temperature creep behavior of YSZ and GZO coatings.

5.2.3 Time Evolution of the Young´s Modulus of GZO Coatings

As discussed in Chapter 4, the thermal cycling tests of the YSZ/GZO double layer systems with the GZO layers which have the same total porosity content but different microstructural features revealed different performances at 1400 °C surface temperature (see Figure 4.20). The assumption was that the individual strain tolerances of the different microstructural features can be leading to different thermal cycling performances. For that reason, the Young´s moduli of the GZO coatings of interest (450 A-350 mm, 350 A-75 mm, 450 A-95 mm systems with the total porosity volume of ∼20, 20 and 11 %, respectively) were investigated. The Young´s modulus evolution of the coatings monitored at 1400 °C as a function of time (t) and compared with the initial RT values (t=0).

Figure 5.11 shows the obtained maximum strain vs. maximum stress plot of these GZO coatings at RT exhibiting a linear elastic relationship with comparable stress levels. The results clearly indicate that the GZO coating sprayed at 450 A with 95 mm stand-off distance, which has the lowest porosity (11 %), displays the highest Young´s modulus (12 ± 1 GPa). On the other hand, the two other GZO microstructures, which have the same total 20 % porosity, also yield different Young's moduli. The elastic modulus of the coatings sprayed with 450 A-350 mm and 350 A-75 mm current and stand-off distances was found to be 2.3 ± 0.3 GPa vs. 4.7 ± 0.5 GPa. It is consistent in the literature that the poor interfacial contact or otherwise weakly bonded regions due to presence of microcracks and small pores cause a decrease in the Young's Modulus in plasma-sprayed coatings, and large pores lead a further reduction (Kim and Kweon, 1999; Kulkarni *et al.*, 2003). Based on the microstructural characterizations of the two coatings sprayed at 350 A and 450 A, the main microstructural difference is the presence of the unmelted particles (350 A) and the large globular pores (450 A) in these coatings. The latter presumably have a stronger effect on decreasing the splat contact area, which means higher induced local stresses and strains and hence reduced effective Young´s modulus of the microstructure.

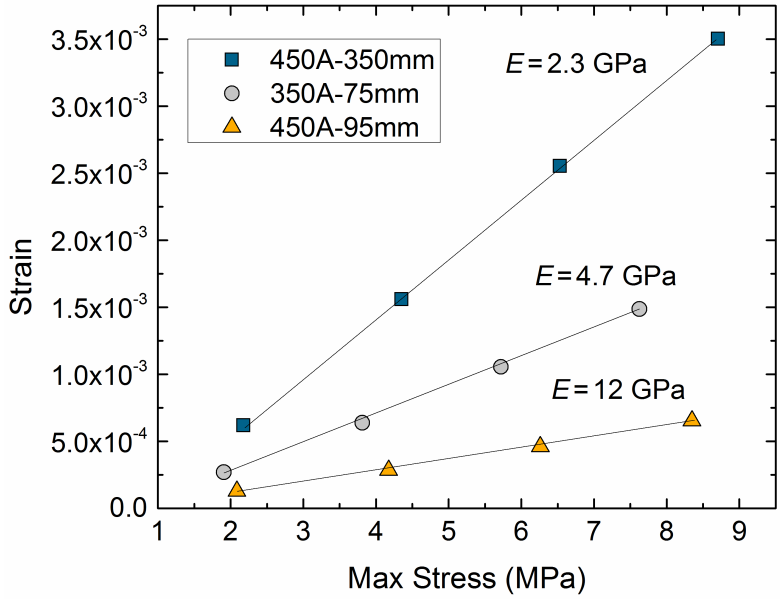

Figure 5.11: Strain-stress plot of the GZO coatings with different microstructures obtained by three-point bending tests. The resulting Young´s moduli (E) are included in the graph.

The Young´s modulus evolution of these three GZO coatings at an annealing temperature of 1400 °C is shown in Figure 5.12. The monitored data was fit with the stiffening equation in (Vaßen *et al.*, 2009b);

$$E(t) = E_0 \frac{1 + A \cdot exp\left(-\frac{Q}{RT}\right) t^n}{1 + \frac{E_0}{E_\infty} \cdot A \cdot exp\left(-\frac{Q}{RT}\right) t^n} = E_0 \frac{1 + \beta t^n}{1 + \frac{E_0}{E_\infty} \beta t^n} \tag{5.2}$$

where E_0 denotes the Young's modulus of the as-sprayed coating, E_∞ the bulk modulus (175 GPa, Vaßen *et al.* (2000)), β a temperature dependent factor, and n the time exponent which indicates the speed of the stiffening process. The results indicate a rapid initial increase in the stiffness (t=0h..2h) followed by a progressive rise (t=2h..43h). Same trends were observed in zirconia top coats and Thompson and Clyne (2001) proposed a two-stage sintering mechanism for plasma-sprayed coatings. The first stage which leads to a fast and significant increase in the stiffness was attributed to grain growth associated improvements in bonding across the splat boundaries, while the second stage was related to repair of the microcracks resulting in progressive increase in the stiffness.

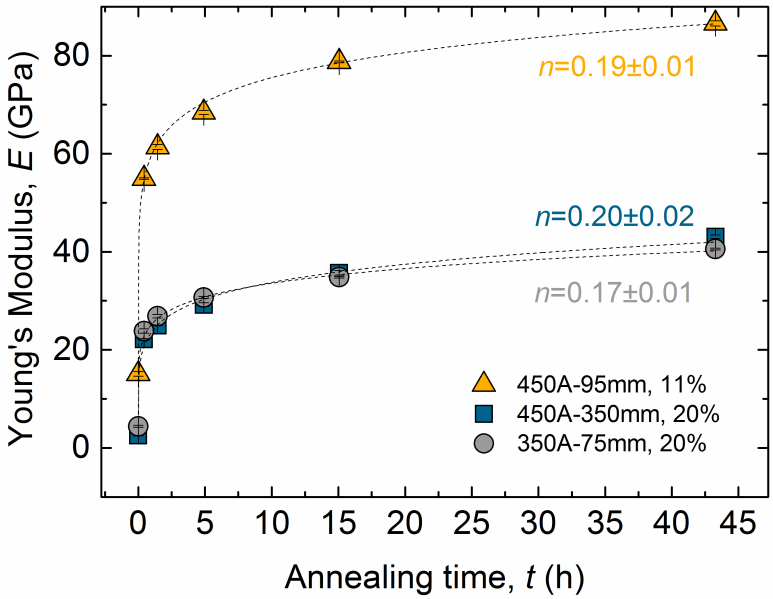

Figure 5.12: Young´s modulus evolution of the GZO coatings at 1400 °C. The time exponent (n) of the fit according to Equ. (5.2) is indicated on the graph.

The absolute values of the modulus of the high porous GZO materials remain smaller in the observed time range. The time exponents of the fits according to Equ. (5.2) reveal that the stiffening rate of the all coatings are almost the same (n=0.17, 0.19, 0.20 ± 0.01). Furthermore, the final modulus (t=43 h) of the coating sprayed at 450 A with 350 mm distance is found to be even slightly higher than that of the coating sprayed at 350 A (43.1 ± 0.5 GPa vs. 40.5 ± 0.7 GPa), which were 2.3 ± 0.3 GPa vs. 4.7 ± 0.5 GPa at t=0. In fact, more sintering activity leading to a higher final stiffness of the coating sprayed at 350 A was expected. Because, due to presence of fine unmelted particles, it has a higher specific surface energy providing the driving force for sintering to occur.

A comparison of the microstructure of the coatings in the as-sprayed and annealed states is given in Figure 5.13. Associated with the microcrack healings and sintering necks occurred across splat and particle boundaries after 200 h annealing at 1400 °C, a significant grain growth along with the small-closed pores in these grains are observed. Nevertheless, although it is hard to judge the size and amount of them, still some of the globular pores, intersplat cracks and unmelted particles separated with voids remain in the related microstructures increasing the splat contact areas even after 200 h (Figure 5.13 a1-b1).

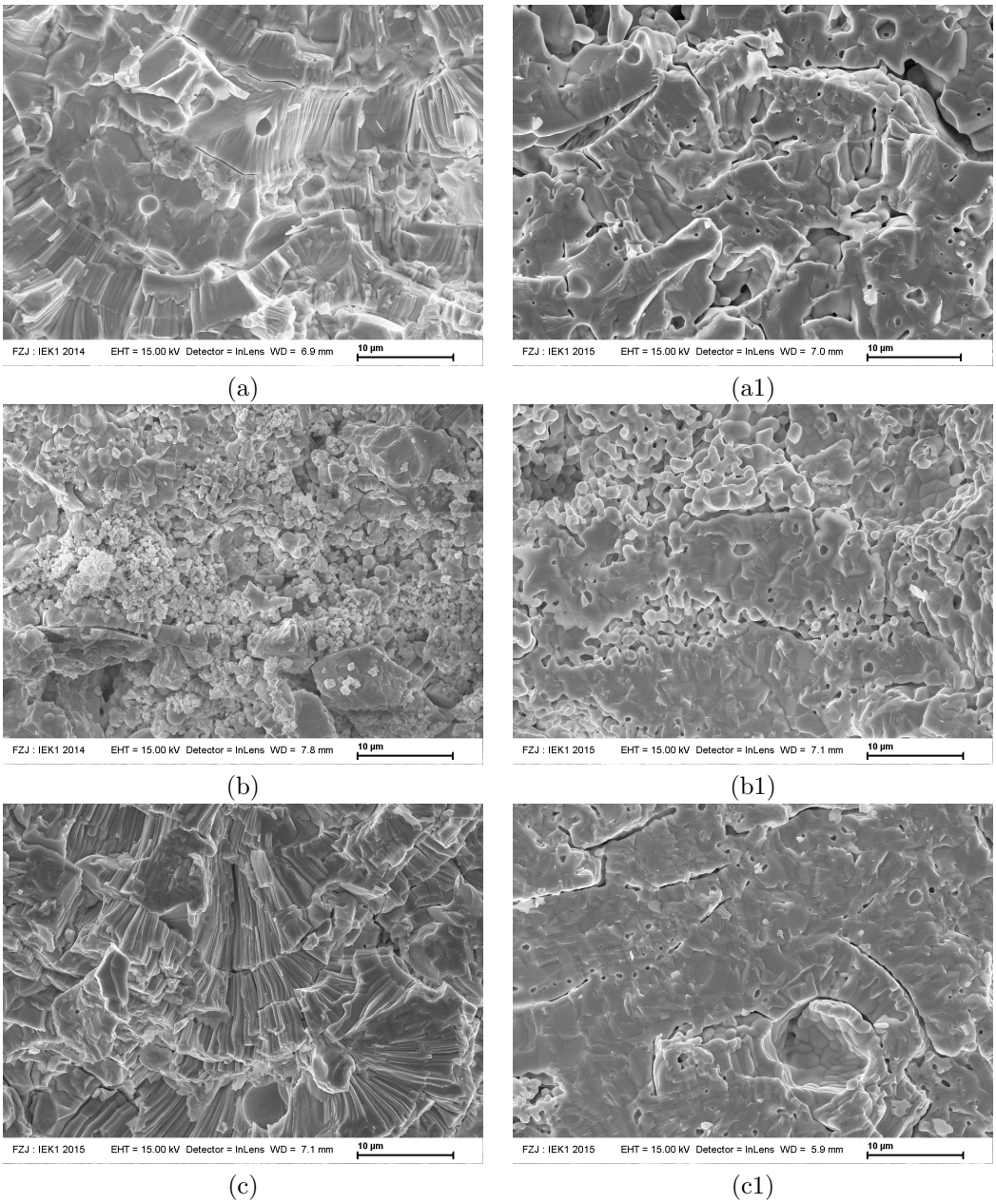

Figure 5.13: Fracture surface SEM images of the as-sprayed (a-b-c) and annealed (1400 °C-200 h) (a1-b1-c1) GZO coatings. The spray parameters are 450 A-350 mm (a), 350 A-75 mm (b), 450 A-95 mm (c).

Possibly, because the unmelted particles still maintain their porous structure after sintering, they do not lead to a strong bonding in the structure (at least in the monitored 43 hours) and hence are still able to provide some strain tolerance. Furthermore, despite the driving force for the sintering is higher for the unmelted particles, their mass transport kinetics can be different than that of the molten and re-solidified splats. As the presence of defects in crystalline solids allows diffusional mass transport to take place, the defects control the rates of processes such as sintering, grain growth and creep as discussed before. Considering that the unmelted particles are sintered and ordered pyrochlore powder particles unlike the defect-fluorite sprayed splats, the rate of diffusion in the later and hence the sintering and bonding to each other can be initially faster. This might be a factor assisting the higher stiffness of the microstructure composed of solely sprayed splats. Notwithstanding, more research is needed on the ordering and sintering kinetics for elucidating the mechanisms of stiffening in these microstructures. On the other hand, the results clearly indicate their similar value of elastic modulus, which cannot explain their different thermal cycling performances. Further observations and remarks related to individual performance of the layers will be given in following conclusion chapter.

6 | Summary and Concluding Remarks

Within the scope of this dissertation GZO was investigated as a topcoat material for TBCs. Three main topics were examined: (i) the APS processing of the GZO and its impact on the microstructural and compositional properties of the as-sprayed GZO coatings; (ii) the thermal cycling lifetime of the YSZ/GZO double-layer coatings manufactured with the systematically changed GZO spray parameters at a surface temperature of 1400 °C; (iii) the thermophysical and thermomechanical properties of the GZO and YSZ coatings such as thermal conductivity, CTE, elastic and creep behavior. Studies on the microstructural and compositional properties highlighted the importance of the process parameters on the development of the GZO coatings with desirable porosity features and homogenous composition assisting superior lifetime performances. A significant insight was gained into the time and temperature dependent elastic and creep behavior of the coatings which play a critical role on the development of advanced TBCs. The overarching conclusion of this work is that the GZO has the potential to increase the temperature capability of gas turbines, if it is applied in double-layer TBC systems and if its microstructure is tailored according to requirements and favorably supported by advanced process design and diagnostic methods. Detailed conclusions and remarks follow below.

The APS processing related study revealed that the monitored in-flight particle temperature distributions can be used as a rapid-estimation tool to reach desired properties during process optimization. A process parameter window was defined based on these distributions initially from the spray current of 300 A to 525 A using 65 mm to 95 mm stand-off distances. Highly porous GZO coatings could be produced ($<$450 A, $>$18 % porosity) with a microstructure consisting of high amount of fine unmelted particles in this window. As the gadolinia evaporation was a major concern, the chemical composition of the produced GZO coatings as well as GZO single splats was investigated utilizing different characterization techniques. The results suggested that there is no notable gadolinia loss in the detectable limits. Nevertheless it should be mentioned that the lattice parameters and chemical analysis results of the GZO coatings sprayed at high spray currents ($\geq$450 A) showed slight deviations from the stoichiometric composition. Furthermore, the thermal cycling results of the YSZ/GZO double-layer coatings manufactured with the GZO spray currents of $\geq$450 A ($<$18 % porosity) yielded very early failures ($<$ 15 cycles), while higher porous GZO coatings showed significantly superior

performances. The low porosity as well as evaporation of gadolinia were considered as potential reasons of these early failures at this stage of the work. Therefore, to completely eliminate the possibility of the contribution of gadolinia evaporation to the early failures, a new process parameter window at a high spray current was studied.
Highly porous GZO coatings (>18 %) were aimed to be achieved at 450 A and to be tested under the same thermal cycling conditions. Because, if the evaporation has an influence on lifetime, this should have resulted in early failures regardless of high porous microstructure obtained at the high spray current. The particle temperature measurements suggested to acquire a high amount of re-solidified particles at 450 A with the stand-off distances above 300 mm. Using this information a highly porous GZO coating (20 %) was achieved at 350 mm with a microstructure containing no unmelted particles, so different from the produced highly porous coatings in the first process window. The differences in the microstructural features of these GZO coatings were investigated by a derivative analysis of the pore size distribution data obtained via MIP technique. The comparison of the porosity features of the two coatings (350 A-75mm vs. 450 A-350 mm) both with 20 % porosity revealed that the main microstructural difference is the presence of the unmelted particles (350 A) and the large globular pores (450 A) in these coatings. Moreover, although a porosity increase from 11 % to 20 % was observed by comparing the coating sprayed in the 1st process window at 450 A-95 mm with the coating obtained at 450 A-350 mm, no chemical composition difference was found. This implies that the gadolinia evaporation occurs mainly in the hot plasma zone so that extended stand-off distances do not affect the total volume of vaporized gadolinia in the detectable limits. Finally, the thermal cycling tests of the double-layer system manufactured with the 20 % porous GZO sprayed at 450 A yielded an even better performance than the system with 20 % porous GZO sprayed in the first process parameter window. Figure 6.1 shows the compiled thermal cycling results of YSZ/GZO double layer TBCs obtained in this study. Based on the results it can be concluded that;

- the degree of gadolinia evaporation even at a high spray current such as 450 A does not critically affect the lifetime, considering the best performance obtained with the GZO layer sprayed with 450 A-350 mm current and stand-off distance,

- the porosity level of the GZO (and YSZ) layer governs the lifetime of double layers,

- not only the porosity level of the GZO layer but also its microstructure considerably influences the lifetime of double-layer systems. Because, although the GZO layers sprayed at 350 A-75 mm and 450 A-350 mm current and stand-off distances display

the same cumulative porosity level of 20 %, their different microstructures reveal dissimilar lifetime performances.

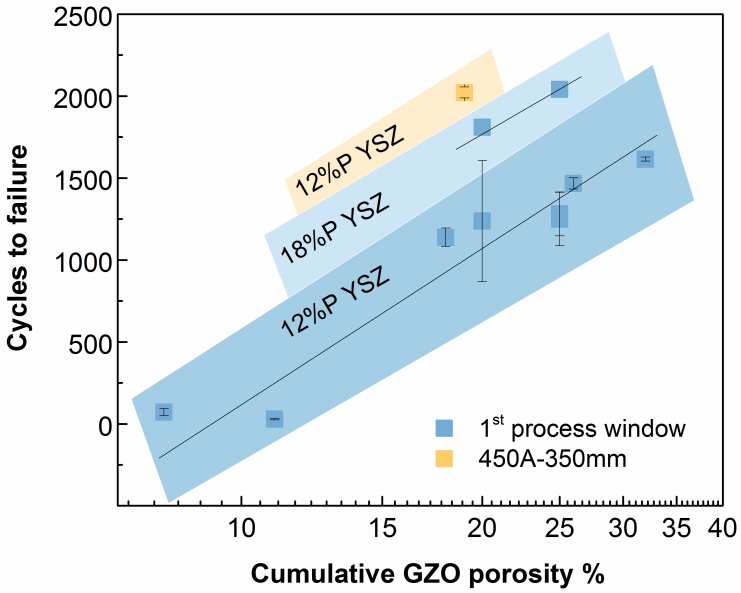

Figure 6.1: Thermal cycling results (T_{surface}:1400 °C) of YSZ/GZO double layer TBCs as a function of the porosity of GZO and YSZ layers. Note that the GZO coating sprayed at 450 A current with 350 mm stand-distance display a different microstructure than the GZO coatings sprayed in the first process parameter window. The cycling results with 18 % YSZ porosity were taken from the conducted DFG project (Project No 1108) for comparison.

To learn more about the thermomechanical behavior of these same porous GZO layers with different microstructures, which could help to elucidate their particular lifetime performances, the Young´s moduli of the GZO coatings of interest were investigated. The Young´s modulus evolution of the coatings was monitored at 1400 °C as a function of time (t) and compared with the initial room temperature (RT) values (t=0). The RT elastic modulus of the coatings sprayed with 450 A-350 mm and 350 A-75 mm current and stand-off distances was found to be 2.3 ± 0.3 GPa vs. 4.7 ± 0.5 GPa. The lower elastic modulus of the former could be attributed to the large globular pores which decrease the splat contact area in this coating. However, after 43 h heat treatment at 1400 °C, the Young´s modulus of the same coatings was measured to be 43.1 ± 0.5 GPa and 40.5 ± 0.7 GPa, respectively. The micrographs of the annealed coatings (1400 °C-200 h)

revealed a significant grain growth for both coatings, although some globular pores and the unmelted particles were still present in the related microstructures. It was assumed that, because the unmelted particles still maintain their porous structure after sintering, they do not lead to a strong bonding in the structure (at least in the monitored 43 hours) and hence are still able to provide some strain tolerance. On the other hand, considering the higher disordering degree and defect concentration in the sprayed splats compared to the unmelted particles, the diffusional mass transport and hence sintering can be faster in the former assisting the higher stiffness of the coating sprayed at 450 A. After all, the stiffening mechanism of these microstructures remains to be clarified by future work. On the other hand, the results clearly indicate their similar value of elastic modulus, which cannot explain their different thermal cycling performances. In this regard, another explanation can be proposed based on an observation on the crack propagation behavior of the GZO coatings. Figure 6.2 shows a cross-section image of a thermally cycled YSZ/GZO double-layer system, as an example. It can be clearly seen from the image that the cracks propagate along unmelted particles. According to the crack growth mechanism the cracks always propagate along the direction with minimum critical strain energy release rate (Sih, 1991). So that, obviously these fine particles distributed in the microstructure introduce a crack propagation path that supplies the minimum resistance. Therefore, it is believed that the presence of unmelted particles might be lowering the critical energy release rate of the microstructure.

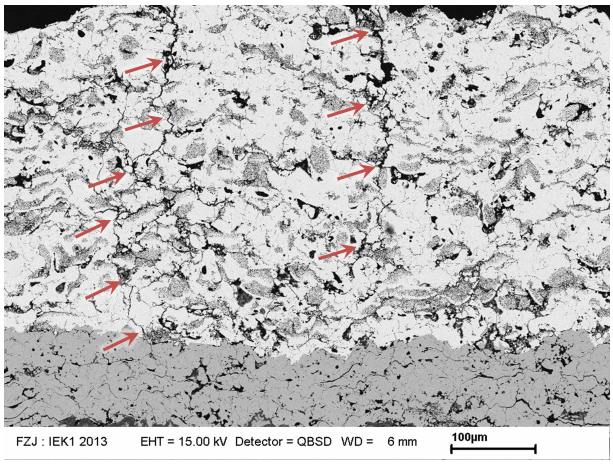

Figure 6.2: Crack growth along the boundaries between unmelted particles in a thermally cycled GZO layer.

This might explain the inferior performance of the GZO coating with the unmelted particles (350 A-75 mm) compared to the GZO coating without these particles (450 A-350 mm), despite their same 20 % total porosity and similar strain tolerances. Thus, the implication associated with the performance of the YSZ/GZO double layer system is that not only the total porosity but also the porosity features (size, aspect ratio, distribution etc.) are needed to be controlled by processing. Furthermore, the results and observations once again manifested the requirement of the strategies to improve the intrinsic toughness of the GZO, which seems going to be an issue of a long-standing debate in the literature.

In this thesis work, a DFG/FVV project (Deutsche Forschungsgemeinschaft/ Forschungsvereinigung Verbrennungskraftmaschinen e.V., Project No:1108) was conducted based on the lifetime modeling of plasma sprayed YSZ/GZO double-layer TBCs. Similar to the findings here on the thermally cycled GZO coatings, delamination cracks through unmelted particle paths were observed during isothermal oxidation tests of the GZO coatings at 1100 °C. Furthermore, better performances of the GZO coatings with less amount of unmelted particles, in this particular case sprayed with an F4 plasma torch and with different spray parameters, were monitored in these tests. Additionally, it was found in this project that the thermal cycling performance of the YSZ/GZO double layer coatings are significantly influenced by the roughness of bond coat interface as well as the thickness of the YSZ layer. Particularly early failures were observed when the high bond coat roughness ($R_a \geq$ 16 µm) is combined with the low YSZ thickness (<100 µm) despite high porous GZO layers (25 %).

Comparison of the investigated thermophysical and thermomechanical properties of the YSZ and GZO coatings manifests that the later is superior to the former in terms of thermal insulation and strain tolerance. The thermal conductivity of the GZO was found to be ∼25 % lower than that of the YSZ (0.6 W/mK vs. 0.8 W/mK, 1273 K, 18 % porosity), while the RT elastic modulus of the as-sprayed GZO and YSZ coatings both with 18 % porosity was measured to be 5 GPa and 16.5 GPa. Furthermore, based on the results, similar mismatch strains can be expected to be developed with the metallic substrate and bond coat in the both YSZ and GZO ceramic coatings. Because, examination of the CTE of the plasma-sprayed GZO layer revealed that the CTE of the GZO (10.9×10^{-6} K^{-1}, 1273 K) is comparable to that of the plasma-sprayed 8YSZ coating (10.7×10^{-6} K^{-1}, 1273 K, Cao *et al.* (2004)).

Temperature dependency of the elastic modulus of the as-sprayed GZO and YSZ coatings were investigated from RT to 1400 °C. The results indicated no significant changes in the moduli of the coatings from RT up to 800 °C. An increase in the moduli was observed

with the further temperature increase, which was related to enhanced sintering at elevated temperatures. On the other hand, significantly different temperature-dependent behaviors of annealed YSZ and GZO coatings were recorded. After 200 h heat treatment at 1400 °C, the RT elastic modulus of the GZO coating showed almost an order of magnitude increase (from ∼5 GPa to ∼47 GPa) compared to the RT modulus of the as-sprayed coating. With the temperature increase, a progressive decrease in the modulus of the annealed GZO coating was observed approaching to 30 GPa at 1400 °C. The observed decrease of the modulus was attributed to increased thermal vibrations as well as to non-elastic effects such as grain boundary sliding and softening. For the annealed YSZ coating (200 h-1400 °C), however, a strong temperature-dependent behavior of the elastic modulus was monitored showing large scatter with values between 75 and 50 GPa, which can be due to the secondary phases introduced by phase separations of t' phase above 1200 °C.

Temperature dependency of the viscosity of the coatings was also extracted from the same experiments. In agreement with the literature, observed behaviors of the plasma-sprayed coatings suggested different creep mechanisms at RT and at relatively high temperature ranges (800-1400 °C). The creep observed at RT was attributed to mechanical sliding process between the splats, while a diffusion driven creep mechanism in the high temperature range was shown by the Arrhenius dependency of the data. Notwithstanding, no significant differences were found between either in RT or high temperature viscosity of the YSZ and GZO coatings.

The effect of load duration on the elastic and creep behavior of the coatings at RT and at 1400 °C was also investigated. The elastic modulus of the YSZ and GZO coatings was found to be independent from the load duration, while a linear relationship between the viscosity and the load duration was observed for both material at RT. The time-dependent strain increase at longer load durations was associated with a strain hardening effect in the coatings as a result of mechanically locked splats. The measurements at 1400 °C revealed that the effect of load duration on the viscosity becomes less predominant at the elevated temperature suggesting a modification in the creep mechanism of the mechanical splat sliding. A diffusion driven creep mechanism at elevated temperatures, as shown previously by Arrhenius dependency of the data, became evident with these findings.

Bibliography

Ahrens, M., Vaßen, R., Stöver, D. and Lampenscherf, S. (2004), 'Sintering and Creep Processes in Plasma-Sprayed Thermal Barrier Coatings', *J. Therm. Spray Technol.* **13**(3), 432–442.

Arnault, V., Mévrel, R., Alpérìne, S. and Jaslier, Y. (1999), 'Thermal Barrier Coatings for Aircraft Turbine Airfoils : Thermal Challenge and Materials', *Revue de Metallurgie. Cahiers D'Informations Techniques* **96**(5), 585–597.

Aygun, A., Vasiliev, A. L., Padture, N. P. and Ma, X. (2007), 'Novel Thermal Barrier Coatings that are Resistant to High-Temperature Attack by Glassy Deposits', *Acta Mater.* **55**(20), 6734–6745.

Bansal, N. P. and Zhu, D. (2007), 'Effects of Doping on Thermal Conductivity of Pyrochlore Oxides For Advanced Thermal Barrier Coatings', *Mater. Sci. Eng. A* **459**(1), 192–195.

Barrett, J. and Malati, M. (1997), *Fundamentals of Inorganic Chemistry: An Introductory Text for Degree Studies*, Elsevier Science.

Bast, U. and Schumann, E. (2009), *26th Annual Conference on Composites, Advanced Ceramics, Materials, and Structures-B: Ceramic Engineering and Science Proceedings*, Wiley, chapter Development of Novel Oxide Materials for TBCs, pp. 525–532.

Bathie, W. (1996), *Fundamentals of Gas Turbines-Second Edition*, Wiley.

Benninghoven, A. (1994), 'Chemical Analysis of Inorganic and Organic Surfaces and Thin Films By Static Time-of-Flight Secondary Ion Mass Spectrometry (TOF-SIMS)', *Angewandte Chemie International Edition in English* **33**(10), 1023–1043.

Birks, N., Meier, G. H. and Pettit, F. S. (2006), *Introduction to the High Temperature Oxidation of Metals*, second edn, Cambridge University Press. Cambridge Books Online.

Bolelli, G., Sabiruddin, K., Lusvarghi, L., Gualtieri, E., Valeri, S. and Bandyopadhyay, P. (2010), 'FIB Assisted Study of Plasma Sprayed Splat-Substrate Interfaces: NiAl-Stainless Steel and Alumina-NiAl Combinations', *Surf.Coat. Tech.* **205**(2), 363–371.

Bouse, G. K. and Mihalisin, J. R. (1989), *Metallurgy of Investment Cast Superalloy Components*, Academic Press, pp. 99–148.

Bragg, W. and Bragg, W. (1913), 'The Reflection of X-rays by Crystals', *Proc. R. Soc. Lond* .

Burggraaf, A., van Dijk, T. and Verkerk, M. (1981), 'Structure and Conductivity of Pyrochlore and Fluorite Type Solid Solutions', *Solid State Ionics* **5**, 519–522. Proceedings of the International Conference on Fast Ionic Transport in Solids.

Campbell, F. (2008), *Elements of Metallurgy and Engineering Alloys*, ASM International.

Cao, X., Vaßen, R., Jungen, W., Schwartz, S., Tietz, F. and Stöver, D. (2001), 'Thermal Stability of Lanthanum Zirconate Plasma-Sprayed Coating', *J. Am. Ceram. Soc.* **84**(9), 2086–2090.

Cao, X., Vaßen, R. and Stöver, D. (2004), 'Ceramic Materials for Thermal Barrier Coatings', *J. Eur. Ceram. Soc.* **24**(1), 1–10.

Cao, X., Vaßen, R., Tietz, F. and Stöver, D. (2006), 'New Double-Ceramic-Layer Thermal Barrier Coatings Based on Zirconia-Rare Earth Composite Oxides', *J. Eur. Ceram. Soc.* **26**(3), 247–251.

Carter, C. and Norton, G. (2013), *Ceramic Materials: Science and Engineering*, Springer New York.

Chen, X., Wang, R., Yao, N., Evans, A., Hutchinson, J. and Bruce, R. (2003), 'Foreign Object Damage in a Thermal Barrier System: Mechanisms and Simulations', *Mater. Sci. Eng.: A* **352**(1-2), 221–231.

Chevalier, J., Gremillard, L., Virkar, A. V. and Clarke, D. R. (2009), 'The Tetragonal-Monoclinic Transformation in Zirconia: Lessons Learned and Future Trends', *J. Am. Ceram. Soc.* **92**(9), 1901–1920.

Choi, S. R., Zhu, D. and Miller, R. A. (2008), *Deformation and Strength Behavior of Plasma-Sprayed ZrO_2-8wt. Y_2O_3 Thermal Barrier Coatings in Biaxial Flexure and Trans-Thickness Tension*, John Wiley & Sons, Inc., pp. 653–661.

Clarke, D. R., Oechsner, M. and Padture, N. P. (2012), 'Thermal-Barrier Coatings for More Efficient Gas-Turbine Engines', *Mrs Bulletin* **37**(10), 891–898.

Clave, A. (2006), Atomic Scale Simulations for Waste Form Applications, PhD thesis, Imperial College of London.

Coble, R. L. and Kingery, W. D. (1956), 'Effect of Porosity on Physical Properties of Sintered Alumina', *J. Am. Ceram. Soc.* **39**(11), 377–385.

Curry, N., VanEvery, K., Snyder, T. and Markocsan, N. (2014), 'Thermal Conductivity Analysis and Lifetime Testing of Suspension Plasma-Sprayed Thermal Barrier Coatings', *Coatings* **4**(3), 630–650.

Czech, N., Schmitz, F. and Stamm, W. (1994), 'Improvement of MCrAlY Coatings by Addition of Rhenium', *Surf. Coat. Tech.* **68-69**(0), 17 – 21.

Davis, J. and Committee, A. (2000), *Nickel, Cobalt, and Their Alloys*, ASM International.

de Boer, G. B. J., de Weerd, C., Thoenes, D. and Goossens, H. W. J. (1987), 'Laser Diffraction Spectrometry: Fraunhofer Diffraction Versus Mie Scattering', *Particle & Particle Systems Characterization* **4**(1-4), 14–9.

Diaz-Guillen, J., M.R., D.-G., Padmasree, K., Fuentes, A., Santamaria, J. and Leon, C. (2008), 'High Ionic Conductivity in The Pyrochlore-Type $Gd_{2-y}La_yZr_2O_7$ Solid Solution (0<y<1)', *Solid State Ionics* **179**(38), 2160–2164.

Dosch, R. G., Headly, T. J. and Hlava, P. (1984), 'Crystalline Titanate Ceramic Nuclear Waste Forms:Processing and Microstructure"', *J. Am. Ceram. Soc.* **67**(5), 354–361.

Drexler, J. M., Chen, C.-H., Gledhill, A. D., Shinoda, K., Sampath, S. and Padture, N. P. (2012a), 'Plasma Sprayed Gadolinium Zirconate Thermal Barrier Coatings that are Resistant to Damage by Molten Ca-Mg-Al-Silicate Glass', *Surf. Coat. Technol.* **206**(19-20), 3911–3916.

Drexler, J. M., Ortiz, A. L. and Padture, N. P. (2012b), 'Composition Effects of Thermal Barrier Coating Ceramics on Their Interaction With Molten Ca-Mg-Al-Silicate (CMAS) Glass', *Acta Mater.* **60**(15), 5437–5447.

Dudek, M., Rog, G., Bogusz, W., Kozlowska-Rog, A., Bucko, M. and Zych, L. (2006), 'Calcium Zirconate as a Solid Electrolyte for Electrochemical Devices Applied in Metallurgy', *Materials Science Poland* **24**(1), 253–260.

Dunin-Borkowski, R., Newcomb, S., Boothroyd, C., Czyrska-Filemonowicz, A., Clemens, D. and Quadakkers, W. (1996), A Grain Boundary Study of the Aluminium Oxide

Formed on MA 956 of Different Yttria Contents, *in* S. Newcomb and J. A. Little, eds, 'Microscopy of Oxidation', 3rd International conference on Microscopy of Oxidation, The Institute of Materials, Cambridge, pp. 166–176.

Dwivedi, G., Tan, Y., Viswanathan, V. and Sampath, S. (2015), 'Process-Property Relationship for Air Plasma-Sprayed Gadolinium Zirconate Coatings', *J. Therm. Spray Technol.* **24**(3), 454–466.

Dwivedi, G., Viswanathan, V., Sampath, S., Shyam, A. and Lara-Curzio, E. (2014), 'Fracture Toughness of Plasma-Sprayed Thermal Barrier Ceramics: Influence of Processing, Microstructure, and Thermal Aging', *J. Am. Ceram. Soc.* **97**(9), 2736–2744.

Eaton, H. and Novak, R. (1987), 'Sintering Studies Of Plasma-Sprayed Zirconia', *Surf. Coat. Tech.* **32**(1-4), 227–236.

EIA (2014), International Energy Outlook, Technical report, U.S. Energy Information Administration. (www.eia.gov/forecasts/ieo/pdf/0484(2014).pdf), September 30, 2014.

Eldridge, J. I., Spuckler, C. M. and Markham, J. R. (2009), 'Determination of Scattering and Absorption Coefficients for Plasma-Sprayed Yttria-Stabilized Zirconia Thermal Barrier Coatings at Elevated Temperatures', *J. Am. Ceram. Soc.* **92**(10), 2276–2285.

Evans, A., Clarke, D. and Levi, C. (2008), 'The Influence of Oxides on the Performance of Advanced Gas Turbines', *J. Eur. Ceram. Soc.* **28**(7), 1405–1419.

Evans, A., Mumm, D., Hutchinson, J., Meier, G. and Pettit, F. (2001), 'Mechanisms controlling the durability of thermal barrier coatings', *Progress in Materials Science* **46**(5), 505–553.

Fabrichnaya, O. and Aldinger, F. (2004), 'Assessment of Thermodynamic Parameters in The System ZrO_2-Y_2O_3-Al_2O_3', *Zeitschrift für Metallkunde* **95**(1), 27–39.

Fabrichnaya, O., Wulf, R., Kriegel, M., Savinykh, G., Dopita, M.and Seidel, J., Heitz, H., Nashed, O., Gross, U. and H.J., S. (2015), 'Thermophysical Properties of Pyrochlore and Fluorite Phases in the $Ln_2Zr_2O_7$-Y_2O_3 systems (Ln= La, Nd, Sm): 2. Comparison of Conventionally Sintered and SPS samples in the systems $Nd_2Zr_2O_7$-Y_2O_3 and $Sm_2Zr_2O_7$-Y_2O_3', *J. Alloy Compd.* **625**, 200–207.

Fauchais, P., Heberlein, J. and Boulos, M. (2014), *Thermal Spray Fundamentals: From Powder to Part*, Springer.

Feng, J., Xiao, B., Zhou, R. and Pan, W. (2012), 'Thermal Expansions of $Ln_2 2Zr_2O_7$ (Ln=La, Nd, Sm, and Gd) Pyrochlore', *J. Appl. Phys.* **111**(10), 103535–4.

Fincke, J., Haggard, D. and Swank, W. (2001), 'Particle Temperature Measurement in The Thermal Spray Process', *J. Therm. Spray Technol.* **10**(2), 255–266.

Firestone, R. F., Logan, W. R., Adams, J. W. and Bill, R. C. (1982), *Creep of Plasma-Sprayed-ZrO_2 Thermal-Barrier Coatings*, John Wiley & Sons, Inc., pp. 758–771.

Freling, M., Maloney, M., Litton, D., Schlichting, K., Smeggil, J. and Snow, D. (2008), 'Thermal Barrier Coating Compositions, Processes for Applying Same and Articles Coated With Same', *US Patent 7,455,913* . US Patent 7,455,913.

Friedrich, C., Gadow, R. and Schirmer, T. (2001), 'Lanthanum Hexaaluminate a New Material for Atmospheric Plasma Spraying of Advanced Thermal Barrier Coatings', *J. Therm. Spray Technol.* **10**(4), 592–598.

Gadow, R. and Lischka, M. (2002), 'Lanthanum Hexaaluminate-Novel Thermal Barrier Coatings For Gas Turbine Applications-Materials And Process Development', *Surf. Coat. Tech.* **151-152**, 392–399.

Gadow, R. and Schäfer, G. (2006), 'Thermal Insulating Material and Method Of Producing Same', Patent.

Gao, W. (2008), *Developments in High Temperature Corrosion and Protection of Materials*, Woodhead Publishing Series in Metals and Surface Engineering, Elsevier Science.

Gil, A., Shemet, V., Vassen, R., Subanovic, M., Toscano, J., Naumenko, D., Singheiser, L. and Quadakkers, W. (2006), 'Effect of Surface Condition on the Oxidation Behaviour of MCrAlY Coatings', *Surf. Coat. Tech.* **201**(7), 3824–3828.

Goodenough, J. B. (2000), 'Ceramic Technology: Oxide-ion Conductors by Design', *Nature* **404**(6780), 821–823.

Goodenough, J. and Castellano, R. (1982), 'Defect Pyrochlores as Catalyst Supports', *J. Solid State Chem.* **44**(1), 108–112.

Goward, G. (1998), 'Progress in Coatings for Gas Turbine Airfoils', *Surface and Coatings Technology* **108-109**(0), 73 – 79.

Green, D. (1998), *An Introduction to the Mechanical Properties of Ceramics*, Cambridge Solid State Science Series, Cambridge University Press.

Gualco, G., Corcoruto, S., Campora, A., Taylor, R., Schwingel, D. and Oswald, S. (1997), Highly Porous Thick Thermal Barrier Coatings Produced by Air Plasma Spraying of a Plastic-Ceramic Mixed Powder, *in* 'Thermal Spray: a United Forum for Scientific and Technological Advances', pp. 305–313.

Gudmundsson, B. and Jacobson, B. (1989), 'Yttrium Oxides in Vacuum-Plasma-Sprayed CoNiCrAlY Coatings', *Thin Solid Films* **173**(1), 99–107.

Guignard, A., Mauer, G., Vaßen, R. and Stöver, D. (2012), 'Deposition and Characteristics of Submicrometer-Structured Thermal Barrier Coatings by Suspension Plasma Spraying', *J. Therm. Spray Technol.* **21**(3-4), 416–424.

Guillén, M. D., Guillén, J. D., Padmasree, K., Almanza, J. and Fuentes, A. (2008), 'Synthesis and Electrical Properties of The Pyrochlore-Type $Gd_{2-y}La_yZr_2O_7$ Solid Solution', *Boletín de la Sociedad Española de Cerámica y Vidrio* **47**(3), 159–164.

Guo, H., Zhang, H., Ma, G. and Gong, S. (2009), 'Thermo-Physical and Thermal Cycling Properties of Plasma-Sprayed $BaLa_2Ti_3O_{10}$ Coating as Potential Thermal Barrier Materials', *Surf. Coat. Tech.* **204**(5), 691–696.

Guo, L., Guo, H., Peng, H. and Gong, S. (2014), 'Thermophysical Properties of Yb_2O_3 Doped $Gd_2Zr_2O_7$ and Thermal Cycling Durability of $(Gd_{0.9}Yb_{0.1})_2Zr_2O_7$/YSZ Thermal Barrier Coatings', *J. Eur. Ceram. Soc.* **34**(5), 1255–1263.

Habibi, M., Wang, L. and Guo, S. (2012), 'Evolution of Hot Corrosion Resistance of YSZ, $Gd_2Zr_2O_7$, and $Gd_2Zr_2O_7$ + YSZ Composite Thermal Barrier Coatings in Na_2SO_4 + V_2O_5 at 1050°C', *J. Eur. Ceram. Soc.* **32**(8), 1635–1642.

Hasselman, D. P. H., Johnson, L. F., Bentsen, L., Rahmatullah, S., Hong, L. L. and Swain, M. (1987), 'Thermal Diffusivity and Conductivity of Dense Polycrystalline ZrO_2 Ceramics: a Survey', *Am. Ceram. Soc. Bull.* **66**, 799–806.

Hayashi, S. and Gleeson, B. (2009), 'Early-Stage Oxidation Behavior of Pt-Modified γ' Ni_3-Al Based Alloys with and without Hf Addition', *Oxidation of Metals* **71**(1-2), 5–19.

Haynes, J., Pint, B., More, K., Zhang, Y. and Wright, I. (2002), 'Influence of Sulfur, Platinum, and Hafnium on the Oxidation Behavior of CVD NiAl Bond Coatings', *Oxidation of Metals* **58**(5-6), 513–544.

Ishizaki, K., Komarneni, S. and Nanko, M. (1998), *Porous Materials: Process Technology and Applications*, Materials Technology Series, Springer US.

Jacobson, N. (1989), *Thermodynamic Properties of Some Metal Oxide-Zirconia Systems*, NASA-Lewis Research Center, Cleveland, OH.

Jang, B.-K. and Matsubara, H. (2006), 'Influence of Porosity on Thermophysical Properties of Nano-Porous Zirconia Coatings Grown by Electron Beam-Physical Vapor Deposition', *Scripta Materialia* **54**(9), 1655–1659.

Jarligo, M. O., Mack, D. E., Mauer, G., Vaßen, R. and Stöver, D. (2010), 'Atmospheric Plasma Spraying of High Melting Temperature Complex Perovskites for TBC Application', *J. Therm. Spray Technol.* **19**(1-2), 303–310.

Jones, R. (1997), 'Some Aspects of the Hot Corrosion of Thermal Barrier Coatings', *J. Therm. Spray Technol.* **6**(1), 77–84.

Jones, R. L., Reidy, R. F. and Mess, D. (1996), 'Scandia, Yttria-stabilized Zirconia for Thermal Barrier Coatings', *Surf. Coat. Tech.* **82**(1-2), 70–76.

Kaden, U., Leyens, C., Peters, M. and Kaysser, W. A. (1999), Thermal Stability of an EB-PVD Thermal Barrier Coating System on a Single Crystal Nickel-Based Superalloy, *in* J. M. Hampikian and N. B. Dhotre, eds, 'Elevated Temperature Coatings: Science and Technology', Vol. 3, The Minerals, Metals, Materials Society, p. 27.

Karger, M., Vaßen, R. and Stöver, D. (2011), 'Atmospheric Plasma Sprayed Thermal Barrier Coatings With High Segmentation Crack Densities: Spraying Process, Microstructure And Thermal Cycling Behavior', *Surf. Coat. Tech.* **206**(1), 16–23.

Kim, H. J. and Kweon, Y. G. (1999), 'Elastic Modulus of Plasma-Sprayed Coatings Determined by Indentation and Bend Tests', *Thin Solid Films* **342**(1-2), 201–206.

Kingery, W. D., Bowen, H. K. and Uhlmann, D. R. (1976), *Introduction to Ceramics*, Wiley Interscience, New York.

Klein, S. and Nellis, G. (2011), *Thermodynamics*, Cambridge University Press.

Klemens, P. (1996), *Thermal Conductivity 23*, CRC Press, chapter Thermal Conductivity of Zirconia, pp. 209–220.

Knott, J. (1973), *Fundamentals of Fracture Mechanics*, Butterworths.

Kong, L., Karatchevtseva, I., Gregg, D. J., Blackford, M. G., Holmes, R. and Triani, G. (2013), '$Gd_2Zr_2O_7$ And $Nd_2Zr_2O_7$ Pyrochlore Prepared By Aqueous Chemical Synthesis ', *J. Eur. Ceram. Soc.* **33**(15-16), 3273–3285.

Korf, S. J., Koopmans, H. J., Lippens, B. C., Burggraaf, A. J. and Gellings, P. J. (1987), 'Electrical and Catalytic Properties of Some Oxides with the Fluorite or Pyrochlore Structure. Co Oxidation on Some Compounds Derived From $Gd_2Zr_2O_7$', *Journal of the Chemical Society, Faraday Transactions 1: Physical Chemistry in Condensed Phases* **83**(5), 1485–1491.

Krämer, S., Yang, J. and Levi, C. G. (2008), 'Infiltration-Inhibiting Reaction of Gadolinium Zirconate Thermal Barrier Coatings with CMAS Melts', *J. Am. Ceram. Soc.* **91**(2), 576–583.

Krämer, S., Yang, J., Levi, C. G. and Johnson, C. A. (2006), 'Thermochemical Interaction of Thermal Barrier Coatings with Molten CaO-MgO-Al_2O_3-SiO_2 (CMAS) Deposits', *J. Am. Ceram. Soc.* **89**(10), 3167–3175.

Kulkarni, A., Wang, Z., Nakamura, T., Sampath, S., Goland, A., Herman, H., Allen, J., Ilavsky, J., Long, G., Frahm, J. and Steinbrech, R. W. (2003), 'Comprehensive Microstructural Characterization and Predictive Property Modeling of Plasma-Sprayed Zirconia Coatings', *Acta Mater.* **51**(9), 2457–2475.

Kutty, K. G., Rajagopalan, S., Mathews, C. and Varadaraju, U. (1994), 'Thermal Expansion Behaviour Of Some Rare Earth Oxide Pyrochlores', *Materials Research Bulletin* **29**(7), 759–766.

Lakiza, S. M. and Lopato, L. M. (1997), 'Stable and Metastable Phase Relations in the System Alumina-Zirconia-Yttria', *J. Am. Ceram. Soc.* **80**(4), 893–902.

Langston, L. S. (2011), 'Powering Ahead', *Mechanical Engineering* **133**(5), 30–33.

Langston, L. S. (2012), 'Breaking the Barriers: As Gas Turbines are Ever More Widely Used, They are Achieving New Heights of Performance', *Mechanical Engineering-CIME* p. 32.

Langston, L. S. (2014), *Reference Module in Earth Systems and Environmental Sciences*, Elsevier, chapter Turbines, Gas.

Le Bail, A., Duroy, H. and Fourquet, J. (1988), 'Ab-initio Structure Determination of $LiSbWO_6$ by X-Ray Powder Diffraction', *Materials Research Bulletin* **23**(3), 447–452.

Leckie, R. (2006), Fundamental Issues Regarding the Implementation of Gadolinium Zirconate in Thermal Barrier Coatings, PhD thesis, University of California Santa Barbara.

Leckie, R., Krämer, S., Rühle, M. and Levi, C. (2005), 'Thermochemical Compatibility Between Alumina and ZrO_2-$GdO_{3/2}$ Thermal Barrier Coatings', *Acta Mater.* **53**(11), 3281–3292.

Lee, K. N. (2005), 'Protective Coatings for Gas Turbines', *The Gas Turbine Handbook* **4**(2).

Lee, W. Y., Stinton, D. P., Berndt, C. C., Erdogan, F., Lee, Y.-D. and Mutasim, Z. (1996), 'Concept of Functionally Graded Materials for Advanced Thermal Barrier Coating Applications', *J. Am. Ceram. Soc.* **79**(12), 3003–3012.

Lehmann, H., Pitzer, D., Pracht, G., Vassen, R. and Stöver, D. (2003), 'Thermal Conductivity and Thermal Expansion Coefficients of the Lanthanum Rare-Earth-Element Zirconate System', *J. Am. Ceram. Soc.* **86**(8), 1338–1344.

Levi, C. G. (2004), 'Emerging Materials and Processes for Thermal Barrier Systems', *Current Opinion in Solid State and Materials Science* **8**(1), 77–91.

Li, W., Zhao, H., Zhong, X., Wang, L. and Tao, S. (2014), 'Air Plasma-Sprayed Yttria and Yttria-Stabilized Zirconia Thermal Barrier Coatings Subjected to Calcium-Magnesium-Alumino-Silicate (CMAS)', *J. Therm. Spray Technol.* **23**(6), 975–983.

Litton, D., Schlichting, K., Freling, M., Smeggil, J., Snow, D. and Maloney, M. (2010), 'Durable Reactive Thermal Barrier Coatings', *US Patent 7,662,489* .

Liu, Z.-G., Ouyang, J.-H., Zhou, Y. and Li, S. (2010), 'High-Temperature Hot Corrosion Behavior of Gadolinium Zirconate By Vanadium Pentoxide and Sodium Sulfate in Air', *J. Eur. Ceram. Soc.* **30**(12), 2707–2713.

Liu, Z.-G., Zhang, W.-H., Ouyang, J.-H. and Zhou, Y. (2014), 'Novel Double-Ceramic-Layer $(La_{0.8}Eu_{0.2})_2Zr_2O_7$/YSZ Thermal Barrier Coatings Deposited by Plasma Spraying', *Ceramics International* **40**(7, Part B), 11277–11282.

Ma, W., Jarligo, M., Mack, D., Pitzer, D., Malzbender, J., Vaßen, R. and Stöver, D. (2008b), 'New Generation Perovskite Thermal Barrier Coating Materials', *J. Therm. Spray Technol.* **17**(5-6), 831–837.

Ma, W., Mack, D., Malzbender, J., Vaßen, R. and Stöver, D. (2008a), 'Yb_2O_3 and Gd_2O_3 Doped Strontium Zirconate for Thermal Barrier Coatings', *J. Eur. Ceram. Soc.* **28**(16), 3071–3081.

Maloney, M. (2000), 'A Ceramic Surface Coatings Has a Cubic Pyrochlore Structure', *US Patent 6,117,560* .

Maloney, M. (2001), 'Thermal Barrier Coating Systems and Materials', *US Patent 6,177,200* .

Marple, B. R., Voyer Joël, T. M., Nagy, D. R. and Va/ssen (2004), 'Hot Corrosion of Lanthanum Zirconate and Partially Stabilized Zirconia Thermal Barrier Coatings', *J. Eng. Gas Turbines Power* **128**(1), 144–152.

Marrow, T., Roberts, S. and Pearce-Higgins, A. (1994), 'The Brittle/Ductile Transition In Cubic Stabilised Zirconia', *J. Eur. Ceram. Soc.* **14**(5), 447–453.

Matejicek, J., Sampath, S., Brand, P. and Prask, H. (1999), 'Quenching, Thermal and Residual Stress in Plasma Sprayed Deposits: NiCrAlY And YSZ Coatings', *Acta Mater.* **47**(2), 607–617.

Mauer, G., Hospach, A., Zotov, N. and Vaßen, R. (2013), 'Process Conditions and Microstructures of Ceramic Coatings by Gas Phase Deposition Based on Plasma Spraying', *J. Therm. Spray Technol.* **22**(2-3), 83–89.

Mauer, G., Sebold, D., Vaßen, R. and Stöver, D. (2012), 'Improving Atmospheric Plasma Spraying of Zirconate Thermal Barrier Coatings Based on Particle Diagnostics', *J. Therm. Spray Technol.* **21**(3-4), 363–371.

Mauer, G., Vaßen, R. and Stöver, D. (2008), 'Detection of Melting Temperatures and Sources of Errors Using Two-Color Pyrometry During In-flight Measurements of Atmospheric Plasma-Sprayed Particles', *Int. J. Thermophys.* **29**(2), 764–786.

Mazilin, I., Baldaev, L. and Drobot, D. (2014), Lanthanum and Gadolinium Zirconate Thermal Barrier Coatings Structure and Properties Evolution, *in* 'Thermal Spray 2014: Proceedings of the International Thermal Spray Conference (May 21-23, 2014, Barcelona, Spain)'.

Meier, G. H. and Pettit, F. S. (1992), 'The Oxidation Behavior of Intermetallic Compounds', *Mater. Sci. Eng.: A* **153**(1-2), 548–560.

Mercer, C., Faulhaber, S., Evans, A. and Darolia, R. (2005), 'A Delamination Mechanism for Thermal Barrier Coatings Subject to Calcium-Magnesium-Alumino-Silicate (CMAS) Infiltration', *Acta Mater.* **53**(4), 1029–1039.

Mercer, C., Williams, J., Clarke, D. and Evans, A. (2007), 'On a Ferroelastic Mechanism Governing the Toughness of Metastable Tetragonal-Prime Yttria-Stabilized Zirconia', *Proceedings of the Royal Society of London A: Mathematical, Physical and Engineering Sciences* **463**(2081), 1393–1408.

Michel, D., Mazerolles, L. and Perez y Jorba, M. (1984), *Advances in Ceramics: Science and Technology of Zirconia II*, Vol. 12, American Ceramic Society, Ohio„ chapter Polydomain Crystals of Single-Phase Tetragonal ZrO_2: Structure, Microstructure and Fracture Toughness, pp. 131–138.

Mikijelj, B., Varela, J. A. and Whittemore, O. J. (1991), 'Equivalence of Surface Areas Determined by Nitrogen Adsorption and By Mercury Porosimetry', *Am. Ceram. Soc. Bull.* **70**(5), 829–31.

Miller, R. A. (1987), 'Current Status of Thermal Barrier Coatings- An Overview', *Surf. Coat. Tech.* **30**(1), 1–11.

Miller, R. A. (1997), 'Thermal Barrier Coatings for Aircraft Engines: History and Directions', *J. Therm. Spray Technol.* **6**(1), 35–42.

Miller, R. A., Smialek, J. L. and Garlick, R. (1981), 'Phase Stability in Yttria Stabilized ZrO_2', *Adv. Ceramics* **3**, 241–253.

Minervini, L., Grimes, R. W. and Sickafus, K. E. (2000), 'Disorder in Pyrochlore Oxides', *J. Am. Ceram. Soc.* **83**(8), 1873–1878.

Moskal, G., Swadzba, L., Hetmanczyk, M., Witala, B., Mendala, B., Mendala, J. and Sosnowy, P. (2012), 'Characterisation of the Microstructure and Thermal Properties of $Nd_2Zr_2O_7$ and $Nd_2Zr_2O_7$/YSZ Thermal Barrier Coatings', *J. Eur. Ceram. Soc.* **32**(9), 2035–2042.

Mücke (2007), Sinterung von Zirconiumdioxid-Elektrolyten im Mehrlagen-Verbund der Oxidkeramischen Brennstoffzelle (SOFC), PhD thesis, Ruhr Universität Bochum. in German.

Munawar, A. U., Schulz, U., Cerri, G. and Lau, H. (2014), 'Microstructure and Cyclic Lifetime of Gd and Dy-containing EB-PVD TBCs Deposited as Single and Double-Layer on Various Bond Coats', *Surf. Coat. Technol.* **245**, 92–101.

Nakamichi, M., Takabatake, T. and Kawamura, H. (1998), 'Material Design Of Ceramic Coating By Plasma Spray Method', *Fusion Engineering and Design* **41**(1-4), 143–147.

Nicholls, J. (2000), 'Designing Oxidation-Resistant Coatings', *JOM* **52**(1), 28–35.

Nicholls, J., Deakin, M. and Rickerby, D. (1999), 'A Comparison Between the Erosion Behaviour of Thermal Spray and Electron Beam Physical Vapour Deposition Thermal Barrier Coatings', *Wear* **233-235**(0), 352–361.

Niessen, K. v., Gindrat, M. and Refke, A. (2010), 'Vapor Phase Deposition Using Plasma Spray-PVD', *J. Therm. Spray Technol.* **19**(1-2), 502–509.

Nijdam, T. and Sloof, W. (2007), 'Effect of Reactive Element Oxide Inclusions on the Growth Kinetics of Protective Oxide Scales', *Acta Mater.* **55**(17), 5980–5987.

Ogawa, K., Ito, K., Shoji, T., Seo, D., Tezuka, H. and Kato, H. (2006), 'Effects of Ce and Si Additions to CoNiCrAlY Bond Coat Materials on Oxidation Behavior and Crack Propagation of Thermal Barrier Coatings', *J. Therm. Spray Technol.* **15**(4), 640–651.

Olesik, J. W. (1991), 'Elemental Analysis Using ICP-OES and ICP/MS', *Analytical Chemistry* **63**(1), 12A–21A.

Padture, N. P., Gell, M. and Jordan, E. H. (2002), 'Thermal Barrier Coatings for Gas-Turbine Engine Applications', *Science* **296**(5566), 280–284.

Pan, W., Gong, J., Ge, C.-C. and Li, J.-F. (2007a), 'Novel Low Thermal Conductivity Ceramic Materials for Thermal Barrier Coatings', *Key Engineering Materials* **280-283**, 1497–1500.

Pannetier, J. (1973), 'Energie electrostatique des reseaux pyrochlore', *J. Phys. Chem. Solids* **34**(4), 583–589. In French.

Parker, W. J., Jenkins, R. J., Butler, C. P. and Abbott, G. L. (1961), 'Flash Method of Determining Thermal Diffusivity, Heat Capacity, and Thermal Conductivity', *J. Appl. Phys.* **32**(9), 1679–1684.

Pawley, G. S. (1981), 'Unit-cell Refinement From Powder Diffraction Scans', *J. Appl. Crystallogr.* **14**(6), 357–361.

Pawlowski, L. (2008), *The Science and Engineering of Thermal Spray Coatings*, Wiley.

Pawlowski, L. (2009), 'Suspension and Solution Thermal Spray Coatings', *Surf. Coat. Tech.* **203**(19), 2807–2829.

Pawlowski, L., Lombard, D. and Fauchais, P. (1985), 'Structure-Thermal Properties-Relationship in Plasma Sprayed Zirconia Coatings', *J. Vac. Sci. Technol., A* **3**(6), 2494–2500.

Pint, B. A. (2003), 'Optimization of Reactive-Element Additions to Improve Oxidation Performance of Alumina-Forming Alloys', *J. Am. Ceram. Soc.* **86**(4), 686–95.

Poerschke, D. L. and Levi, C. G. (2015), 'Effects of Cation Substitution and Temperature on the Interaction Between Thermal Barrier Oxides and Molten {CMAS} ', *J. Eur. Ceram. Soc.* **35**(2), 681–691.

Pollock, T. M. and Tin, S. (2006), 'Nickel-Based Superalloys for Advanced Turbine Engines: Chemistry, Microstructure and Properties', *J. Propul. Power* **22**(2), 361–374.

Porat, O., Heremans, C. and Tuller, H. L. (1997), 'Phase Stability and Electrical Conductivity in $Gd_2Ti_2O_7$-$Gd_2Mo_2O_7$ Solid Solutions', *J. Am. Ceram. Soc.* **80**(9), 2278–2284.

Qin, Y. X., Wang, J. D., Pan, W., Wan, C. L. and Qu, Z. X. (2007), 'Low thermal conductivity ceramics for thermal barrier coatings', *Key Engineering Materials* **336-338**, 1764–1766.

Qun-bo, F., Feng, Z., Fu-chi, W. and Wang, L. (2009), 'Molecular dynamics calculation of thermal expansion coefficient of a series of rare-earth zirconates', *Computational Materials Science* **46**(3), 716–719. Proceedings of the 18th International Workshop on Computational Mechanics of Materials IWCMM-18.

Rabiei, A. and Evans, A. (2000), 'Failure Mechanisms Associated with the Thermally Grown Oxide in Plasma-Sprayed Thermal Barrier Coatings', *Acta Mater.* **48**(15), 3963–3976.

Radhakrishnan, A. N., Rao, P. P., Linsa, K. S. M., Deepa, M. and Koshy, P. (2011), 'Influence of Disorder-to-Order Transition on Lattice Thermal Expansion and Oxide Ion Conductivity In $(Ca_xGd_{1-x})_2(Zr_{1-x}M_x)_2O_7$ Pyrochlore Solid Solutions', *Dalton Trans.* **40**, 3839–3848.

Ramachandran, C., Balasubramanian, V. and Ananthapadmanabhan, P. (2013), 'Erosion of Atmospheric Plasma Sprayed Rare Earth Oxide Coatings Under Air Suspended Corundum Particles', *Ceramics International* **39**(1), 649–672.

Rejda, E. F., Socie, D. F. and Itoh, T. (1999), 'Deformation Behavior of Plasma-Sprayed Thick Thermal Barrier Coatings', *Surf. Coat. Tech.* **113**(3), 218–226.

Rezanka, S., Mauer, G. and Vaßen, R. (2014), 'Improved Thermal Cycling Durability of Thermal Barrier Coatings Manufactured by PS-PVD', *J. Therm. Spray Technol.* **23**(1-2), 182–189.

Rice, R. (2000), *Mechanical Properties of Ceramics and Composites: Grain And Particle Effects*, CRC Press.

Rietveld, H. M. (1967), 'Line Profiles of Neutron Powder-Diffraction Peaks For Structure Refinement', *Acta Cryst.* **22**(151-152).

Sampath, S. and Herman, H. (1996), 'Rapid Solidification and Microstructure Development During Plasma Spray Deposition', *J. Therm. Spray Technol.* **5**(4), 445–456.

Saruhan, B., Francois, P., Fritscher, K. and Schulz, U. (2004), 'EB-PVD Processing of Pyrochlore-Structured $La_2Zr_2O_7$-Based TBCs', *Surf. Coat. Technol.* **182**(2-3), 175–183.

Schäfer, G. and Gadow, R. (1999), 'Lanthanum Aluminate Thermal Barrier Coating'.

Schelling, P. K. and Phillpot, S. R. (2001), 'Mechanism of Thermal Transport in Zirconia and Yttria-Stabilized Zirconia by Molecular-Dynamics Simulation', *J. Am. Ceram. Soc.* **84**(12), 2997–3007.

Schelling, P. K., Phillpot, S. R. and Grimes, R. W. (2004), 'Optimum Pyrochlore Compositions for Low Thermal Conductivity', *Philosophical Magazine Letters* **84**(2), 127–137.

Schulz, U. and Braue, W. (2013), 'Degradation of $La_2Zr_2O_7$ and Other Novel EB-PVD Thermal Barrier Coatings by CMAS (CaO-MgO-Al_2O_3-SiO_2) and Volcanic Ash Deposits', *Surf. Coat. Tech.* **235**, 165–173.

Schulz, U., Leyens, C., Fritscher, K., Peters, M., Saruhan-Brings, B., Lavigne, O., Dorvaux, J.-M., Poulain, M., Mevrel, R. and Caliez, M. (2003), 'Some Recent Trends In Research And Technology Of Advanced Thermal Barrier Coatings', *Aerospace Science and Technology* **7**(1), 73–80.

Schulz, U., Saruhan, B., Fritscher, K. and Leyens, C. (2004), 'Review on Advanced EB-PVD Ceramic Topcoats for TBC Applications', *Int. J. Appl. Ceram. Tec.* **1**(4), 302–315.

Scott, H. (1975), 'Phase Relationships in the Zirconia-Yttria System', *J.Mater.Sci.* **10**(9), 1527–1535.

Shillington, E. A. G. and Clarke, D. R. (1999), 'Spalling Failure of a Thermal Barrier Coating Associated with Aluminum Depletion in the Bond-coat', *Acta Mater.* **47**, 1297–1305.

Shlyakhtina, A., Shcherbakova, L., Knotko, A. and Steblevskii, A. (2004), 'Study of the Fluorite-Pyrochlore-Fluorite Phase Transitions in $Ln_2Ti_2O_7$ (Ln=Lu, Yb, Tm)', *J. Solid State Electr.* **8**(9), 661–667.

Sickafus, K. E., Minervini, L., Grimes, R. W., Valdez, J. A., Ishimaru, M., Li, F., McClellan, K. J. and Hartmann, T. (2000), 'Radiation Tolerance of Complex Oxides', *Science* **289**(5480), 748–751.

Sih, G. (1991), *Mechanics of Fracture Initiation and Propagation: Surface and Volume Energy Density Applied as Failure Criterion*, Kluwer Academic.

Sims, C., Stoloff, N. and Hagel, W. (1987), *Superalloys II*, Wiley.

Smialek, J., Jayne, D., Schaeffer, J. and Murphy, W. (1994), 'Effects of Hydrogen Annealing, Sulfur Segregation and Diffusion on the Cyclic Oxidation Resistance of Superalloys: A Review', *Thin Solid Films* **253**(1-2), 285–292.

Soltani, R., Coyle, T. W. and Mostaghimi, J. (2007), 'Creep Behavior of Plasma-Sprayed Zirconia Thermal Barrier Coatings', *J. Am. Ceram. Soc.* **90**(9), 2873–2878.

Somiya, S., ed. (2012), *Advanced Technical Ceramics*, Elsevier Science.

Song, P. (2012), Influence of Material and Testing Parameters on the Lifetime of TBC Systems with MCrAlY and NiPtAl Bondcoats, PhD thesis, Forschungszentrum Jülich, IEK-2.

Soyez, G., Eastman, J. A., Thompson, L. J., Bai, G.-R., Baldo, P. M., McCormick, A. W., DiMelfi, R. J., Elmustafa, A. A., Tambwe, M. F. and Stone, D. S. (2000), 'Grain-Size-Dependent Thermal Conductivity Of Nanocrystalline Yttria-Stabilized Zirconia Films Grown By Metal-Organic Chemical Vapor Deposition', *Applied Physics Letters* **77**(8), 1155–1157.

Stecura, S. (1977), 'Two-layer layer thermal barrier coating for high temperature components', *Am. Ceram. Soc. Bull* **56**(12), 1082–1085.

Stecura, S. (1978), Effects of Compositional Changes on the Performance of a Thermal Barrier Coating System, Technical report, NASA TM-78976, National Aeronautics and Space Administration.

Stiger, M., Yanar, N., Topping, M., Pettit, F. and Meier, G. (1999), 'Thermal Barrier Coatings For the 21st Century', *Zeitschrift fuer Metallkunde/Materials Research and Advanced Techniques* **90**(12), 1069–1078.

Stott, F., de Wet, D. and Taylor, R. (1994), 'Degradation of Thermal-Barrier Coatings at Very High Temperatures', *MRS Bulletin* **19**, 46–49.

Streibl, T., Vaidya, A., Friis, M., Srinivasan, V. and Sampath, S. (2006), 'A Critical Assessment of Particle Temperature Distributions During Plasma Spraying: Experimental Results for YSZ', *Plasma Chem. Plasma Process.* **26**(1), 73–102.

Subramanian, M., G., A. and G.V., S. R. (1983), 'Oxide Pyrohlores-A Review', *Prog. Solid St. Chem.* **15**, 55–143.

Subramanian, R. (2002), 'Thermal Barrier Coating Having High Phase Stability', *US Patent 6,387,539* .

Subramanian, R. (2005), 'Highly Defective Oxides as Sinter Resistant Thermal Barrier Coating', *US Patent 6,930,066* . US Patent 6,930,066.

Subramanian, R. and Allen, D. (2005), 'Sinter Resistant Abradable Thermal Barrier Coating', *US Patent 6,946,208* .

Suresh, G., Seenivasan, G., Krishnaiah, M. and Murti, P. (1998), 'Investigation of the Thermal Conductivity of Selected Compounds of Lanthanum, Samarium and Europium', *J. Alloys Compd.* **269**(1-2), L9–L12.

Suresh, G., Seenivasan, G., Krishnaiah, M. and Murti, P. S. (1997), 'Investigation of the Thermal Conductivity of Selected Compounds of Gadolinium and Lanthanum', *J. Nucl. Mater.* **249**(2-3), 259–261.

Tarvin, R. and Davies, P. (2004), 'A-Site and B-Site Order in $(Na_{1/2}La_{1/2}(Mg_{1/3}Nb_{2/3})O_3$ Perovskite', *J. Am. Ceram. Soc.* **87**(5), 859–863.

Taylor, T. A. and Bettridge, D. F. (1996), 'Development of Alloyed and Dispersion-Strengthened MCrAlY Coatings', *Surf. Coat. Tech.* **86-87**(0), 9 – 14.

Taylor, T., Appleby, D., Weatherill, A. and Griffiths, J. (1990), 'Plasma-Sprayed Yttria-Stabilized Zirconia Coatings: Structure-Property Relationships', *Surf. Coat. Tech.* **43-44**(0), 470–480.

Thompson, J. and Clyne, T. (2001), 'The Effect of Heat Treatment on The Stiffness of Zirconia Top Coats in Plasma-Sprayed {TBCs}', *Acta Mater.* **49**(9), 1565–1575.

Tong, T. (1994), *Thermal Conductivity 22*, Taylor and Francis.

Toraya, H. (1989), 'Whole-Powder-Pattern Decomposition Method', *The Rigaku Journal* **6**(2), 28–34.

Toscano, J., Gil, A., Huttel, T., Wessel, E., Naumenko, D., Singheiser, L. and Quadakkers, W. (2007), 'Temperature Dependence of Phase Relationships in Different Types of MCrAlY-Coatings', *Surf. Coat. Tech.* **202**(4-7), 603–607.

Traeger, F., Vaßen, R., Rauwald, K. and Stöver, D. (2003), 'Thermal Cycling Setup for Testing Thermal Barrier Coatings', *Adv. Eng. Mater.* **5**(6), 429–432.

VanEvery, K., Krane, M. J., Trice, R. W., Wang, H., Porter, W., Besser, M., Sordelet, D., Ilavsky, J. and Almer, J. (2011), 'Column Formation in Suspension Plasma-Sprayed Coatings and Resultant Thermal Properties', *J. Therm. Spray Technol.* **20**(4), 817–828.

Vaßen, R., Cao, X., Tietz, F., Basu, D. and Stöver, D. (2000), 'Zirconates as New Materials for Thermal Barrier Coatings', *J. Am. Ceram. Soc.* **83**(8), 2023–2028.

Vaßen, R., Giesen, S. and Stöver, D. (2009b), 'Lifetime of Plasma-Sprayed Thermal Barrier Coatings: Comparison of Numerical and Experimental Results', *J. Therm. Spray Technol.* **18**(5-6), 835–845.

Vaßen, R., Jarligo, M. O., Steinke, T., Mack, D. E. and Stöver, D. (2010), 'Overview on Advanced Thermal Barrier Coatings', *Surf. Coat. Tech.* **205**(4), 938–942.

Vaßen, R., Träger, F. and Stöver, D. (2004), 'New Thermal Barrier Coatings Based on Pyrochlore/YSZ Double-Layer Systems', *Int. J. Appl. Ceram. Tec.* **1**(4), 351–361.

Vegard, L. (1921), 'Die Konstitution der Mischkristalle und die Raumfüllung der Atome', *Zeitschrift fur Physik* **5**, 17–26.

Virkar, A. V. and Matsumoto, R. L. K. (1986), 'Ferroelastic Domain Switching as a Toughening Mechanism in Tetragonal Zirconia', *J. Am. Ceram. Soc.* **69**(10), C–224–C–226.

Wan, C., Qu, Z., Du, A. and Pan, W. (2009), 'Influence of B Site Substituent Ti on the Structure and Thermophysical Properties of $A_2B_2O_7$-Type Pyrochlore $Gd_2Zr_2O_7$', *Acta Mater.* **57**(16), 4782–4789.

Wang, C. (2006), Experimental and Computational Phase Studies of the ZrO_2-Based Systems for Thermal Barrier Coatings, PhD thesis, Universität Stuttgart.

Warren, B. (1969), *X-ray Diffraction*, Dover Publications.

Washburn, E. W. (1921), 'The dynamics of capillary flow', *Phys. Rev.* **17**, 273–283.

Wilde, P. and Catlow, C. (1998), 'Defects and Diffusion in Pyrochlore Structured Oxides', *Solid State Ionics* **112**(3-4), 173–183.

Wilde, P. and Catlow, C. (1998b), 'Molecular Dynamics Study of the Effect of Doping and Disorder on Diffusion in Gadolinium Zirconate', *Solid State Ionics* **112**(3-4), 185–195.

Williams, P. (1985), 'Secondary ion mass spectroscopy', *Ann.Rev.Mater.Sci.* **15**, 517–548.

Wu, J., Padture, N. P., Klemens, P. G., Gell, M., García, E., Miranzo, P. and Osendi, M. I. (2002b), 'Thermal Conductivity of Ceramics in the ZrO_2-$GdO_{1.5}$ System', *J. Mater. Res.* **17**(12), 3193–3200.

Wu, J., Wei, X., Padture, N. P., Klemens, P. G., Gell, M., García, E., Miranzo, P. and Osendi, M. I. (2002a), 'Low-Thermal-Conductivity Rare-Earth Zirconates for Potential Thermal-Barrier-Coating Applications', *J. Am. Ceram. Soc.* **85**(12), 3031–3035.

Wuensch, B. J., Eberman, K. W., Heremans, C., Ku, E. M., Onnerud, P., Yeo, E. M., Haile, S. M., Stalick, J. K. and Jorgensen, J. D. (2000), 'Connection Between Oxygen-ion Conductivity of Pyrochlore Fuel-Cell Materials and Structural Change with Composition and Temperature', *Solid State Ionics* **129**(1-4), 111–133.

Xu, Q. (2005), *Research on Rare-Earth Zirconate Ceramics for Thermal Barrier Coatings*, Tsinghua University.

Xu, Z., He, L., Mu, R., Zhong, X., Zhang, Y., Zhang, J. and Cao, X. (2009), 'Double-Ceramic-Layer Thermal Barrier Coatings Of $La_2Zr_2O_7$/YSZ Deposited by Electron Beam-Physical Vapor Deposition', *J Alloy Compd.* **473**(1-2), 509–515.

Xu, Z., Zhong, X., Zhang, J., Zhang, Y., Cao, X. and He, L. (2008), 'Effects Of Deposition Conditions on Composition and Thermal Cycling Life of Lanthanum Zirconate Coatings', *Surf. Coat. Technol.* **202**(19), 4714–4720.

Yashima, M., Ishizawa, N. and Yoshimura, M. (1992), 'Application of an Ion-Packing Model Based on Defect Clusters to Zirconia Solid Solutions: II, Applicability of Vegard's Law', *J. Am. Ceram. Soc.* **75**(6), 1550–1557.

Yokokawa, H., Sakai, N., Horita, T., Yamaji, K., Xiong, Y., Otake, T., Yugami, H., Kawada, T. and Mizusaki, J. (2001), 'Phase Diagram Calculations Of ZrO_2-Based Ceramics With an Emphasis On The Reduction/Oxidation Equilibria Of Cerium Ions In The ZrO_2-$YO_{1.5}$-CeO_2-$CeO_{1.5}$ System', *J. Phase. Equilib.* **22**(3), 331–338.

Zhang, S. and Zhao, D. (2013), *Aerospace materials handbook*, CRC Press, Boca Raton, Fla.

Zhao, H., Begley, M. R., Heuer, A., Sharghi-Moshtaghin, R. and Wadley, H. N. G. (2011), 'Reaction, Transformation and Delamination of Samarium Zirconate Thermal Barrier Coatings', *Surf. Coat. Technol.* **205**(19), 4355–4365.

Zhao, H., Levi, C. G. and Wadley, H. N. G. (2009), 'Vapor deposited samarium zirconate thermal barrier coatings', *Surf. Coat. Technol.* **203**, 3157–3167.

Zhu, D. and Miller, R. (2000), 'Thermal Conductivity and Elastic Modulus Evolution of Thermal Barrier Coatings Under High Heat Flux Conditions', *J. Therm. Spray Technol.* **9**(2), 175–180.

Zhu, D. and Miller, R. A. (1998a), 'Sintering and Creep Behavior of Plasma-Sprayed Zirconia and Hafnia-Based Thermal Barrier Coatings', *Surf. Coat. Tech.* **108-109**(0), 114–120.

Zhu, D. and Miller, R. A. (1998b), 'Determination of Creep Behavior of Thermal Barrier Coatings Under Laser Imposed High Thermal and Stress Gradient Conditions', *J. Mater. Res.* **14**(1), 146–161.

Zhu, D. and Miller, R. A. (2004), 'Development of Advanced Low Conductivity Thermal Barrier Coatings', *Int. J. Appl. Ceram. Tec.* **1**(1), 86–94.

Zhu, D., Nesbitt, J. A., Barrett, C. A., McCue, T. R. and Miller, R. A. (2004), 'Furnace Cyclic Oxidation Behavior of Multicomponent Low Conductivity Thermal Barrier Coatings', *J. Therm. Spray Technol.* **13**(1), 84–92.

Zinkevich, M., Wang, C., Morales, F., Rühle, M. and Aldinger, F. (2005), 'Phase Equilibria in the ZrO_2-$GdO_{1.5}$ System at 1400-1700°C', *J. Alloys Compd.* **398**(1-2), 261–268.

7 | Acknowledgements

Pursuing this PhD abroad has been a truly life-changing, an enjoyable experience for me. It would not have been possible to do it without the support, guidance, encouragement, trust and kind help that I received from many people. Though it will not be enough to express my gratitude in words to all those people, I would still like to give many, many thanks to them. Meinen deutschen Kollegen und Freunden möchte ich auch auf Deutsch Dank sagen.

First and foremost I want to thank my supervisor Prof. Dr. Robert Vaßen for providing me the opportunity to complete my PhD thesis at Forschungszentrum Jülich. I am grateful for his motivation, enthusiasm as well as his broad knowledge and experience in my thesis topic of thermal barrier coatings, which made working with him a privilege for me. I gratefully acknowledge also the financial support of DFG/FVV and the contributions of our project partners to my thesis in this regard.

I cordially thank to the members of my PhD committee, Prof. Dr. Marion Bartsch and Prof. Dr. Viktor Scherer, for evaluating my thesis and for their insightful comments, which enabled me to make the necessary improvements. My gratitude also goes to Prof. Dr. Olivier Guillon for following the progress of my work and for his contributions.

I warmly thank to my official scientific advisor Dr. Daniel Mack for his supervision and guidance. Special thanks also to my "unofficial" advisors, Dr. Georg Mauer and Dr. Robert Mücke, who participated in my investigations and shared their valuable time with me for discussions and giving feedback. I would like to thank to Dr. Ophelia Jarligo, as well, for being a good teacher, colleague and a friend at the same time even from the other side of the Atlantic Ocean. I am very grateful to all of my advisors that they have contributed immensely both to my personal and professional life in Germany.

I gratefully acknowledge the help and support that I received from many colleagues during conducting the experimental research in the Institute for Energy and Climate Research, Materials Synthesis and Processing (IEK-1). I would like to thank to Karl-Heinz Rauwald, Ralf Laufs and Frank Vondahlen for their support in thermal spray operations. Thank you to Dr. Doris Sebold for the numerous microscopical analyses, to Dr. Yoo Jung Sohn for the support in X-ray diffraction analyses, to Sigrid Schwartz-Lückge and Andrea Hilgers for several mercury porosimetry and particle size measurements, to Mark Kappertz for his assistance in metallographic preparations, to Volker Bader for the help

on annealing, to all workshop team but particularly to Gerd Mattonet, Fred Oellers, Tobias Offermanns and Erhan Sucuoğlu not only for mechanical manufacturing works but also for maintenance of my bike, and to many other colleagues for their daily support during my work at Jülich. Thank you to administrative officers and secretaries in IEK-1, as well. I also greatly appreciate the support received through the collaborative work undertaken with the Università di Modena e Reggio Emilia – thank you to Dr. Luca Lusvarghi and Dr. Giovanni Bolelli for microscopical investigations on single splats.
I am thankful to my colleagues at the container offices for their friendship and support, and for creating a cordial and cheerful working environment: Cornelius M. Berger, Philipp J. Terberger, Thomas Keuter, Malte Willberg, Yanli Zhang, Peter Orzessek, Dr. Manuel Krott and Dr. Chih-Long Tsai. Special thanks also to Dr. Diana Marcano and Dr. Reeti Singh. It was a great pleasure and fun to meet and work with you guys.
Last, but above all, I would like to thank my beloved family, for their constant unconditional support, love and encouragement throughout my time in Germany. It is to memory of my father, Enver, and to my mother, Hülya, that I wish to dedicate this thesis. I would also like to extend a special thank you to David, for his presence in my life.

Band / Volume 282
Modelling and Experimental Validation of the Viscosity of Liquid Phases in Oxide Systems Relevant to Fuel Slags
G. Wu (2015), XVI, 170 pp
ISBN: 978-3-95806-081-4

Band / Volume 283
Entwicklung von geträgerten protonenleitenden Dünnschichtmembranen für die Wasserstoffabtrennung
W. Deibert (2015), XI, 117 pp
ISBN: 978-3-95806-082-1

Band / Volume 284
Thermochemische Beständigkeit von keramischen Membranen und Katalysatoren für die H_2-Abtrennung in CO-Shift-Reaktoren
E. M. H. Forster (2015), X, 137 pp
ISBN: 978-3-95806-084-5

Band / Volume 285
Spektrale aktinische Flussdichten und Photolysefrequenzen - Untersuchungen in der atmosphärischen Grenzschicht und der freien Troposphäre
I. M. Lohse (2015), VI, 111, VII-XXIII pp
ISBN: 978-3-95806-086-9

Band / Volume 286
Neue Charakterisierungsmethoden für die Gasdiffusionslage in PEM-Brennstoffzellen vor dem Hintergrund produktionsprozessbedingter Materialschwankungen
S. M. Bach (2015), VIII, 149 pp
ISBN: 978-3-95806-088-3

Band / Volume 287
Using the anisotropy of electrical properties for the characterization of sedimentological structures and preferential flow processes
S. Al-Hazaimay (2015), xxii, 94 pp
ISBN: 978-3-95806-090-6

Band / Volume 288
Aktivitätsuntersuchungen und Methoden zur Regeneration von Katalysatoren für die autotherme Reformierung von Dieselkraftstoffen
K. Löhken (2015), II, 147 pp
ISBN: 978-3-95806-093-7

Band / Volume 289
Large-Scale Three Dimensional Modelling of a Direct Methanol Fuel Cell Stack
J. W. McIntyre (2015), 138 pp
ISBN: 978-3-95806-094-4

Band / Volume 290
Abscheidung von Wärmedämmschichtsystemen mit dem Plasma Spray-Physical Vapor Deposition- (PS-PVD-) Prozess – Untersuchung des Prozesses und der hergestellten Schichten
S. Rezanka (2015), XII, 234 pp
ISBN: 978-3-95806-095-1

Band / Volume 291
Characterization & Modification of Copper and Iron Oxide Nanoparticles for Application as Absorber Material in Silicon based Thin Film Solar Cells
M. R. Nuys (2015), XII, 123 pp
ISBN: 978-3-95806-096-8

Band / Volume 292
Interpretation of L-band brightness temperatures of differently tilled bare soil plots
M. Dimitrov (2015), XIV, 116 pp
ISBN: 978-3-95806-098-2

Band / Volume 293
Atrazine in the environment 20 years after its ban: long-term monitoring of a shallow aquifer (in western Germany) and soil residue analysis
D. S. Vonberg (2015), 149 pp
ISBN: 978-3-95806-099-9

Band / Volume 294
Yttria-Stabilized Zirconia / Gadolinium Zirconate Double-Layer Plasma-Sprayed Thermal Barrier Coating Systems (TBCs) E. Bakan (2015), vi, 132 pp
ISBN: 978-3-95806-100-2

Energie & Umwelt /
Energy & Environment
Band / Volume 294
ISBN 978-3-95806-100-2

JÜLICH
FORSCHUNGSZENTRUM